

Low-Temperature Scanning Tunneling Microscopy Studies on Model Catalysts

DISSERTATION

zur Erlangung des akademischen Grades
doctor rerum naturalium
(Dr. rer. nat.)
im Fach Chemie

eingereicht an der
Mathematisch-Naturwissenschaftlichen Fakultät I
Humboldt-Universität zu Berlin

von
Frau Dipl.-Chem. Maria Kulawik
geboren am 23.10.1976 in Berlin

Präsident der Humboldt-Universität zu Berlin:

Prof. Dr. Christoph Marksches

Dekan der Mathematisch-Naturwissenschaftlichen Fakultät I:

Prof. Thomas Buckhout, PhD

Gutachter:

1. Prof. Dr. Hans-Joachim Freund
2. Prof. Dr. Klaus Rademann
3. Prof. Dr. Richard Berndt

Tag der mündlichen Prüfung: 21. März 2006

Die vorliegende Dissertation wurde von April 2002 bis Januar 2006 in der Abteilung Chemische Physik am Fritz-Haber-Institut der Max-Planck-Gesellschaft unter Anleitung von Herrn Prof. Dr. H.-J. Freund angefertigt.

Abstract

Heterogeneous catalysis plays an important role in industrial synthesis as well as in environmental chemistry. Many heterogeneous catalysts consist of transition metals as active species, which are highly dispersed on an inert oxide support, such as alumina or silica. These catalysts have often very complex structures, which hamper a detailed understanding of decisive structural parameters and underlying reaction mechanisms. Thus, the investigation of well-defined model systems is very important to gain a fundamental understanding of the principles of heterogeneous catalysis.

Within the scope of this work, a well-ordered, thin alumina film on NiAl(110) has been investigated by scanning tunneling microscopy (STM) and spectroscopy (STS) at 5 K. This film was established as model for bulk alumina supports in previous studies, though its exact structure remained unknown. The first part of this work aimed therefore to gain a deeper insight into the atomic structure of the film. Indeed, atomically resolved images of the alumina film could be obtained, whereby the symmetry of the displayed features varied dependent on the tunneling conditions. The assignment of these images to distinct atomic layers of the film was possible only after determination of its structure by DFT calculations [1]. According to these, three out of four oxide layers were visualized by STM: The surface oxygen layer, the surface aluminum layer and the interface aluminum layer. The symmetry of the interface oxygen layer can be derived directly from that. Based on this knowledge, a detailed analysis of antiphase domain boundaries (APDB) became possible, which are regularly occurring line defects in the oxide film. Defects play generally a central role in catalytic processes, especially due to the interplay between their geometric structure and electronic properties. Atomically resolved STM images of APDB and comparing DFT studies revealed that APDB are oxygen-deficient. This leads to the induction of three unoccupied defect levels within the oxide band gap, as determined by STS and confirmed theoretically. Often, oxygen vacancies induce occupied defect levels. The contrary effect that was observed here, is ascribed to an electron transfer into the NiAl substrate, acting as an electron reservoir.

The second part of this thesis addressed the adsorption behavior of the alumina film toward single gold atoms, which were evaporated onto the sample at about 10 K. Prior to thermalization, gold atoms can move on the surface, thus dimers and small clusters are observed beside monomers. At low coverage, these clusters are often one-dimensional (1D) chains, which have limited length, preferential orientation and a gold-gold separation, which is about twice the distance observed in bulk gold. STM images show that gold adsorbs on top of aluminum, whereby only every second aluminum site is occupied in chains. The preferential orientation of dimers and chains with

respect to the NiAl substrate clearly indicates a participation of the metal support in the gold binding. Special gold adsorption sites were identified as places, where the gold adatom, an aluminum atom of the oxide film and atoms of the NiAl support have a special arrangement with respect to each other (e.g. on top). The gold-oxide interaction was further characterized by STS and conductance imaging. Monomers exhibit an occupied and an unoccupied state. According to computational results on related systems, they might be related to the Au 6s level, which splits due to the interaction with the alumina film. For dimers, two unoccupied resonances are observed with symmetric and antisymmetric shape, respectively, clearly indicating an interaction between the gold atoms. As direct orbital overlap can be excluded because of their large separation, a substrate-mediated interaction is suggested. Both occupied and unoccupied states are detected for longer gold chains, and their symmetry confirms the hypothesis of large gold-gold separations. The chain formation is explained with the linear arrangement of favorable adsorption sites, whereby the large separations might result from repulsive (e.g. Coulomb or polaronic) interactions of gold-induced defect states in the oxide. These results demonstrate that adsorption properties of thin oxide films can deviate significantly from bulk oxides. However, the metal adatom plays an important role beside the oxide film itself. For silver atoms on alumina / NiAl(110), for instance, no evidence for a participation of the metal support was observed. The influence of the metal support on the oxide-adatom interaction has therefore to be analyzed carefully for each adsorbate-substrate system to evaluate the model character of an oxide film for the corresponding bulk oxide.

The third part of this work presents size-dependent STM studies on metal clusters (silver, palladium) deposited onto the thin alumina film on NiAl(110). Conductance spectra reveal usually a gap around the sample Fermi level and a series of equidistant peaks for both types of metal clusters, whereby the energy separation between the peaks increases with decreasing cluster size. Spectra series taken along the cluster show furthermore, that the peak positions shift to higher absolute energy with increasing distance from the cluster center. This finding was confirmed by conductance images, where the peaks appear as concentric circles of enhanced conductance with a diameter depending on the sample bias. The described observations are best explained by a Coulomb blockade effect. Another possibility, namely the interpretation of the peaks as quantized electronic levels, is also discussed, but cannot account for all experimental findings. Thus, the spectroscopic data reflect most likely no intrinsic properties of the metal clusters but are due to the specific behavior of a double barrier tunneling junction.

Keywords:

STM, model catalyst, alumina, gold

Zusammenfassung

Die heterogene Katalyse spielt in der industriellen chemischen Synthese sowie in umwelttechnischen Prozessen eine herausragende Rolle. Viele Katalysatoren bestehen aus einem oxidischen Trägermaterial und einer darauf dispergierten aktiven Spezies, in der Regel Übergangsmetalle. Solche Systeme zeichnen sich durch eine hohe strukturelle Komplexität aus, welche ein detailliertes Verständnis von entscheidenden strukturellen Parametern sowie zugrunde liegenden Reaktionsmechanismen meist verhindert. Daher ist die Untersuchung von geeigneten Modellsystemen unerlässlich.

Im Rahmen dieser Arbeit wurde ein dünner, wohldefinierter Aluminiumoxid-Film auf NiAl(110) mittels Rastertunnelmikroskopie (STM) und -spektroskopie (STS) bei 5 K untersucht. Dieser Film konnte bereits in zahlreichen Studien als Modell für Aluminiumoxid-Trägermaterialien etabliert werden, obwohl seine atomare Struktur nicht bekannt war. Ein Ziel dieser Arbeit war es daher, diese genauer zu charakterisieren. In der Tat konnten atomar aufgelöste STM-Bilder des Films aufgenommen werden, wobei verschiedene Symmetrien in Abhängigkeit von den Tunnelbedingungen beobachtet wurden. Das Verständnis der STM-Daten und die Aufklärung der Film-Struktur gelang jedoch erst durch spätere DFT-Rechnungen [1]. Demnach lassen sich die gemessenen STM-Bilder drei der vier Aluminiumoxid-Lagen zuordnen: der obersten Sauerstoff-Lage, der obersten Aluminium-Lage und der *interface* Aluminium-Lage. Die Symmetrie der *interface* Sauerstoff-Atome lässt sich daraus ableiten. Dieses Wissen ermöglichte ein genaues Verständnis von Antiphasendomängengrenzen (APDB), d.h. von regelmäßig auftretenden Liniendefekten des Oxidfilms. Allgemein spielen Defekte oft eine entscheidende Rolle in katalytischen Prozessen, bedingt durch das Zusammenspiel ihrer geometrischen und elektronischen Eigenschaften. Untersuchungen mittels STM und STS sowie vergleichende Rechnungen ergaben, dass es sich bei APDB um sauerstoff-defizitäre Strukturen handelt, wodurch drei unbesetzte Defektzustände induziert werden. Diese werden mit einem Transfer überschüssiger Elektronen in das NiAl-Substrat erklärt.

In dem zweiten Teil der Arbeit wurde das Adsorptionsverhalten des Aluminiumoxid-Films gegenüber einzelnen Gold-Atomen untersucht, wobei Gold bei 10 K mit geringer Bedeckung aufgedampft wurde. STM-Untersuchungen der so präparierten Proben bei 5 K ergaben, dass nicht nur Gold-Monomere, sondern auch Dimere und kleine Cluster auf der Oberfläche vorhanden sind. Letztere sind oft eindimensionale Ketten mit limitierter Länge, charakteristischer Orientierung und einem Gold-Gold-Abstand, der ungefähr doppelt so groß ist wie in Bulk-Gold. Aus STM-Bildern, die Substrat und Ketten mit atomarer Auflösung zeigen, wurde Aluminium als Adsorptionsplatz von Gold ermittelt, wobei in Ketten jedes zweite Aluminium-Atom besetzt ist. Ferner konnte aus

der Orientierung von Dimeren und Ketten auf eine Beteiligung des NiAl-Substrats an der Gold-Oxid-Bindung geschlossen werden. Demnach ist es vorteilhaft, wenn das Gold-Adatom, ein Aluminium-Atom des Oxidfilms und die Atome des darunter befindlichen NiAl eine bestimmte geometrische Konstellation zueinander haben (z.B. übereinander). Die Gold-Oxid-Wechselwirkung wurde weiterhin durch STS und Leitfähigkeitsbilder charakterisiert. Demnach induziert die Adsorption eines Gold-Atoms einen besetzten und einen unbesetzten Zustand, die gemäß theoretischen Arbeiten an vergleichbaren Systemen auf die Wechselwirkung des Au 6s-Niveaus mit dem Oxidfilm zurückgeführt werden können. Gold-Dimere weisen zwei unbesetzte Zustände mit charakteristischer Symmetrie (symmetrisch bzw. antisymmetrisch) auf, was eine Wechselwirkung zwischen beiden Atomen zeigt. Diese wird vermutlich durch das Substrat vermittelt, denn aufgrund des großen Abstands kann ein direkter Orbital-Überlapp ausgeschlossen werden. Besetzte und unbesetzte Zustände wurden auch in Ketten detektiert, deren Ausbildung durch die lineare Anordnung günstiger Adsorptionsplätze erklärt wird. Die ungewöhnlich großen Gold-Gold-Abstände weisen dabei auf eine abstoßende Wechselwirkung zwischen den Gold-induzierten Defektzuständen im Oxid hin (Coulomb oder polaronisch). Die Ergebnisse zeigen klar, dass dünne Filme ein anderes Adsorptionsverhalten aufweisen können als die entsprechenden Bulk-Oxide, wobei das adsorbierte Metall eine entscheidend Rolle spielt. So gibt es z.B. für Silber-Atome keine Indizien für eine Beteiligung des NiAl-Substrats. Ein möglicher Einfluss des Metall-Substrats muss folglich für jedes Adsorbat-Substrat-System einzeln überprüft werden, bevor Ergebnisse von dünnen Filmen auf die Bulk-Phase übertragen werden können.

Im dritten Teil dieser Arbeit wurden die Eigenschaften von Metall-Clustern (Silber, Palladium) auf dem Aluminiumoxid-Film in Abhängigkeit von ihrer Größe untersucht. Leitfähigkeits-Spektren zeigen für beide Metalle äquidistante Peaks, deren Energieabstand mit geringerer werdender Cluster-Größe zunimmt. In einigen Fällen wurde auch eine Region mit unterdrückter Leitfähigkeit um das Fermi-Niveau beobachtet. Spektrenserien über die Cluster zeigen ferner, dass die Peakpositionen mit zunehmendem Abstand vom Cluster-Zentrum zu höheren absoluten Energien verschoben sind. Dies wird durch Leitfähigkeitsbilder bestätigt, in denen die Peaks als konzentrische Ringe erhöhter Leitfähigkeit erscheinen, deren Radius von der Tunnelspannung abhängt. Diese Beobachtungen können am besten mit einer Coulomb-Blockade erklärt werden. Eine Interpretation der Peaks als diskrete elektronische Zustände ist weniger wahrscheinlich, da nur ein Teil der Phänomene erklärt werden kann. Somit reflektieren die Spektren eher Eigenschaften des Tunnelkontakts als intrinsische Cluster-Eigenschaften.

Schlagwörter:

STM, Modellkatalysator, Aluminiumoxid, Gold

Contents

Abstract	iii
Zusammenfassung	v
Contents	vii
List of Figures	x
List of Tables	xiii
1 Introduction	1
2 Methods and Experimental Setup	5
2.1 Scanning Tunneling Microscopy	5
2.1.1 Introduction	5
2.1.2 Principle	6
2.1.3 Theoretical Approaches	7
2.1.4 STM on Thin Oxide Films	8
2.1.5 Imaging of Supported Metal Clusters	10
2.2 Scanning Tunneling Spectroscopy	11
2.2.1 Principle and Theory	11
2.2.2 Spectral Resolution	12
2.2.3 Probing LDOS with STS	13
2.2.4 Coulomb Blockade and Coulomb Staircase	17
2.3 Conductance Imaging	20
2.4 Experimental Setup	20
2.4.1 The UHV System	20
2.4.2 The Microscope Head	22
2.4.3 Vibrational Isolation	22
2.4.4 Cooling	23
2.4.5 Electronics	23
2.5 Tip and Sample Preparation	24
2.5.1 Tip Preparation	24
2.5.2 Sample Mounting	24

2.5.3	Preparation of The Thin Alumina Film on NiAl(110)	24
2.5.4	Deposition of Metal Atoms and Clusters	25
3	The Thin Alumina Film on NiAl(110)	27
3.1	Growth and Orientation	28
3.1.1	Defects	28
3.2	Structure	29
3.3	Antiphase Domain Boundaries	33
3.3.1	Geometric Structure	33
3.3.2	Electronic Structure	37
3.4	Summary	44
4	Single Gold Atoms on the Alumina Film	45
4.1	Introduction	45
4.2	Preliminary Studies on Silver	46
4.3	Gold Species and Their Geometric Properties	47
4.3.1	Deposition of Gold Atoms	47
4.3.2	Gold Species on the Surface	48
4.3.3	Adsorption Site	50
4.3.4	Preferential Orientation of Gold Chains	52
4.4	Electronic Properties	54
4.4.1	Experimental Results	54
4.4.2	Discussion	64
4.5	Summary	71
5	Metal Clusters on the Thin Alumina Film	74
5.1	Introduction	74
5.2	Experimental Results	75
5.2.1	Silver Clusters	75
5.2.2	Palladium Clusters	81
5.3	Interpretation	83
5.3.1	Coulomb Blockade	83
5.3.2	Quantization Along the Cluster Height	90
5.3.3	Comparison	95
5.4	Summary	95
6	Conclusions and Outlook	97
	Bibliography	100

A List of Abbreviations	116
B Publications and Conference Contributions	118
Danksagung	120

List of Figures

1.1	Schematics of a model catalyst based on a thin oxide film.	3
2.1	Schematic setup of a scanning tunneling microscope.	6
2.2	Potential energy scheme of a tunneling junction, consisting of a metallic tip, a vacuum barrier and a thin oxide film on a metal.	9
2.3	Imaging faults on clusters.	11
2.4	Potential energy scheme of a tunneling junction, consisting of of tip, vacuum, adsorbate, oxide film and metal substrate.	16
2.5	Potential energy scheme and electric circuit for a tunneling junction, consisting of tip, vacuum, metal cluster, oxide film and metal substrate.	17
2.6	Calculated dI/dV spectra, characteristic for double barrier tunneling junctions.	18
2.7	Experimental setup.	21
2.8	LEED pattern of the alumina film on NiAl(110).	25
2.9	STM images of Ag and Pd on NiAl(110) at coverages of ~ 0.5 ML.	26
3.1	Size and orientation of the alumina unit cell with regard to the NiAl(110) substrate, and STM image of the oxide film.	28
3.2	Structure of the thin alumina film on NiAl(110), investigated by STM and DFT calculations.	31
3.3	Structure of straight antiphase domain boundaries (APDB) in the thin alumina film, investigated by STM and DFT calculations.	34
3.4	Structure of zigzagged APDB in the surface Al layer.	36
3.5	Burgers vectors of APDB with respect to the NiAl substrate.	37
3.6	Constant current and conductance images of straight APDB in the alumina film on NiAl(110).	39
3.7	Bias dependence of apparent height and dI/dV intensity of APDB with respect to defect-free alumina domains on NiAl(110).	40
3.8	Conductance spectra taken on a straight APDB and on a regular region of the alumina film on NiAl(110).	41

3.9	Partial density of states of surface Al and surface O in the perfect oxide and in APDB.	42
3.10	Constant current and conductance images of two zigzagged APDB in the alumina film on NiAl(110).	43
4.1	Silver atoms on partially and fully oxidized NiAl(110), where they are easily desorbed during the scan process.	47
4.2	STM images of Au atoms on a partially and a fully oxidized NiAl(110) sample.	48
4.3	Bias dependent imaging of Au atoms on alumina / NiAl(110).	49
4.4	Self-assembled Au chains on alumina / NiAl(110), imaged by STM . . .	50
4.5	Desorption of one Au atom of a dimer during the scan process.	51
4.6	Adsorption site of Au chains on alumina / NiAl(110).	51
4.7	Statistical analysis of the orientation of Au dimers on the alumina film.	53
4.8	Preferential orientation of Au chains on alumina / NiAl(110).	54
4.9	Desorption of Au monomers during image acquisition if the sample bias equals the highest occupied state of the Au adatom.	55
4.10	Electronic states of Au monomers, detected by STS and conductance imaging.	56
4.11	Constant current and conductance images of a typical Au dimer.	58
4.12	Conductance spectra and conductance images of Au dimers with different adsorption configuration on the thin alumina film.	59
4.13	Spectroscopic data of Au trimers on alumina / NiAl(110).	60
4.14	Constant current and conductance images of a typical Au tetramer. . .	61
4.15	Electronic properties of a typical Au pentamer, studied by STM, STS and conductance imaging.	62
4.16	Constant current and conductance images of a Au pentamer, the structure of which changes reversibly during the scan.	63
4.17	Schematics showing a possible interaction mechanism between a Au adatom and alumina / NiAl(110).	67
5.1	STM images of Ag clusters on alumina / NiAl(110).	76
5.2	Conductance spectra of Ag particles on the alumina film on NiAl(110).	77
5.3	Energy separation ΔE of measured dI/dV peaks versus cluster volume V for Ag particles on the alumina film on NiAl(110).	77
5.4	Series of 25 dI/dV spectra taken along a line across a Ag cluster on the alumina film on NiAl(110).	78
5.5	Constant current and conductance images of a Ag cluster on the alumina film, recorded at the different sample bias.	79

5.6	Conductance spectra of a Ag cluster dependent on the sample bias used for stabilization of the tip-sample distance.	80
5.7	STM images of Pd clusters on a thin alumina film on NiAl(110).	81
5.8	Conductance spectra of Pd clusters on alumina / NiAl(110), recorded at different setpoint conditions.	82
5.9	Experimental and simulated dI/dV spectra of a Ag cluster on alumina grown on NiAl(110).	86
5.10	Calculated dI/dV spectra of metal clusters on a thin alumina film, whereby the increase of the tip-sample distance is simulated.	87
5.11	Measured and calculated dI/dV spectra of a Pd cluster.	88
5.12	Schematic of the tunneling junction, showing the projected "overlap" area between tip and Ag cluster dependent on the tip position.	90
5.13	Calculated level energies for a particle-in-a-box with box lengths L comparable to real cluster heights.	91
5.14	Potential diagrams for tunneling over center and edge of a cluster.	93
5.15	Band diagrams of Ag and Pd.	94

List of Tables

5.1	Calculated capacitances C_2 dependent on the diameter d_b of the bottom facet of the Ag cluster.	85
5.2	Calculated capacitances C_2 dependent on the diameter d_b and shape of the bottom facet of the Pd cluster.	85

Chapter 1

Introduction

Heterogeneous catalysis plays a tremendous role in chemical industry, since it is involved in the synthesis of more than 90% of all products [2]. Another field of increasing importance is environmental chemistry, where heterogeneous catalysts are used, for instance, to clean exhaust gases in industry and cars. Despite their relevance, the optimization of heterogeneous catalysts can often be achieved only empirically, because structural key parameters and underlying reaction mechanisms are unknown. This is mainly due to the high structural complexity of these catalysts. Usually, they consist of an active species, e.g. a transition metal, which is dispersed onto an inert support with high surface area. Frequently used support materials are metal oxides, such as alumina, silica and titania.

Mainly two strategies are employed to investigate processes involved in heterogeneous catalysis. In the “top-down” approach, working catalysts are used, which are successively modified and simplified to determine parameters relevant for their activity. An example for such “simplification” is the replacement of porous supports by flat surfaces to allow their investigation by surface sensitive techniques. In general, the study of active catalysts is especially suited to gain information on kinetics, working conditions, and regeneration, but also to analyze how structural parameters, e.g. the size of active particles, influence the catalytic activity. However, these systems are usually too complex to analyze properties and processes on the atomic level.

The second strategy, which was used in this thesis, is the surface science (“bottom-up”) approach, where real catalysts are modeled by very simple systems with well-defined structure and properties. These systems have often a strongly reduced catalytic activity but allow to explore and modify the influence of specific parameters, e.g. the shape of the active particles, in a well-defined way. The simplest model systems are metal single crystals. They can be studied by a huge variety of surface science techniques. Most notably, no charging of these samples occurs when bombarded with

electrons or ions, which is essential for the application of many techniques such as low energy electron diffraction (LEED) or scanning tunneling microscopy (STM). The first catalytically relevant studies on metal single crystals were performed in the 1960s and gained interest very rapidly [3–5]. It turned out, that these model systems behave in some cases almost like technical catalysts. A well-known example is the CO hydrogenation to methane, where a Ni(100) surface and a high-area supported Ni catalyst were found to have similar properties with respect to specific rates, activation energy and product distribution [6]. Another example is the ammonia synthesis over iron catalysts, where studies on differently orientated Fe single crystals provided important information for the determination of catalytically active structures and mechanisms in the industrial process [7, 8]. Generally, metal single crystals are suited as models only for structure insensitive reactions or for the investigation of the interplay between different components, which are responsible for the catalytic activity. An example for the latter case is the acetoxylation of ethylene, which is realized industrially on silica-supported Pd-Au bimetallic catalysts. This catalyst was recently modeled by Au single crystals, onto which Pd atoms were deposited. Thus, structural parameters promoting the mentioned reaction could be identified [9].

However, many reactions depend on structural features, which cannot be investigated using metal single crystals, e.g. the size of the active particles, their shape and the interaction with the support. In the case of such structure sensitive reactions, more complex model systems are required. One possibility is to deposit metal clusters onto single crystal metal oxides. If the oxide is sufficiently conductive, charging effects induced by electron or ion based analytical methods can often be avoided, and a variety of surface science techniques can be employed. One of the most intensively studied supports is TiO_2 [10, 11], which becomes an n-type semiconductor after annealing to ~ 1000 K. Another example is CeO_2 , which has normally a band gap of ~ 6 eV. However, reduction and elevated temperatures ($300^\circ\text{--}400^\circ$) induce enough conductivity to make this oxide suited for surface science techniques based on charged particles [12]. Other oxides that have been successfully studied by such methods are Cr_2O_3 [13], SnO_2 [14], NiO [15] and ZnO [16–18]. The number of available techniques is more restricted for highly insulating surfaces, such as MgO, SiO_2 or Al_2O_3 , where charging effects can hardly be avoided. To circumvent this problem, these oxides can be grown as thin films on metal supports [19–23]. In many cases, the band gap of such films resembles that of the corresponding bulk oxide already at a thickness of two or three monolayers (ML). A thin alumina film on NiAl(110), for instance, consists of two aluminum/oxygen layers and has a band gap of 7–8 eV [24, 25] which is close to the value of 8.8 eV measured for $\alpha\text{-Al}_2\text{O}_3$ [26] (9.5 eV for $\gamma\text{-Al}_2\text{O}_3$ [27]). The development of a band gap as a function of film thickness was studied in detail for MgO on Mo(001), where it already amounts

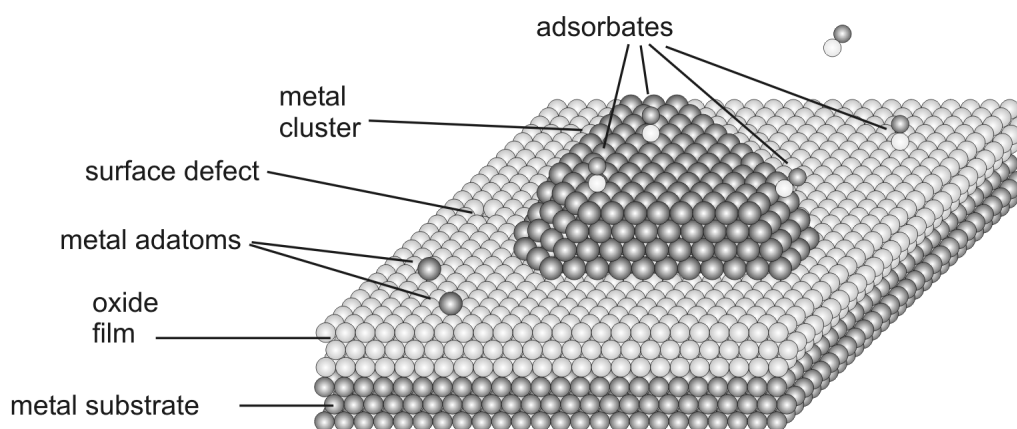


Figure 1.1: Schematics of a model catalyst based on a thin oxide film. Surface science techniques can be used to study the properties of deposited clusters, the adsorption behavior of gases or defects.

to 6 eV for 3 ML films [28]. However, STM studies are possible for much thicker films, consisting of 8 ML or even more [28]. During the past decades, a variety of oxide films have been prepared, e.g. Al_2O_3 [24, 29], MgO [30, 31], SiO_2 [32, 33], and TiO_2 [34, 35]. Each of these oxides was grown on different metal substrates in order to optimize the film properties. The support influences, for instance, the long-range order and structure of the oxide layer as well as the density and nature of defects, which in turn affect the electronic properties. Thus, an alumina film on Ni_3Al exhibits a smaller gap (~ 4.3 eV) [29] than an alumina film on $\text{NiAl}(110)$ (7–8 eV [24, 25]). This effect is ascribed to structural differences of the Ni_3Al -supported film.

If an oxide film has similar chemical and electronic properties as the corresponding bulk oxide, the film is usually considered suitable as support for metal clusters, and the whole system might be used as model catalyst. The structure of such systems is shown schematically in Fig. 1.1. Surface science techniques can now be used to study a variety of their properties, e.g. the diffusion and nucleation of metal adatoms [36], the growth of metal clusters [37], the adsorption of molecules on these clusters [38], as well as the presence of active sites responsible for catalytic activity [39]. The structural discrepancy between model and real catalysts, commonly referred to as *materials gap*, is strongly reduced for oxide film based model catalysts as compared to metal single crystals, making the former superior for the exploration of heterogeneous catalysis. Apart from structural simplifications, the surface science approach deviates from real catalysts also with respect to the experimental conditions. This concerns sometimes the temperature, but more severely the pressure: while industrial catalysts work often at some 100 bar, the described model systems are investigated at ultra-high vacuum (UHV) conditions, i.e. at about 10^{-10} to 10^{-11} mbar. However, this so-called *pressure gap* can be bridged by several techniques which are able to locally create or to deal with

high pressures, e.g. molecular beam experiments [40], sum frequency generation [41] or polarization modulation infrared absorption spectroscopy [42–44]. Here, adsorption and reactivity measurements on model catalysts can be performed at pressures of up to 1 bar.

The aim of this thesis was to study structural, electronic and adsorption properties of a thin alumina film on NiAl(110) with high spatial resolution, using low-temperature scanning tunneling microscopy (STM) and spectroscopy (STS). This film was established as model support for bulk alumina already in the 1990s, even though its atomic structure was not known in detail. Later on, studies on this substrate reached beyond the model catalyst approach: the alumina film was used as non-interacting spacer layer in order to explore the vibronic signature [45, 46] and light emission [47] of single molecules as well as the spin flip in single magnetic adatoms [48]. The increasing interest in this film and thin oxide films in general [9] was motivation for the present work, which investigates the atomic structure and electronic properties of the alumina film that are crucial for the understanding of the various studies using this support.

The thesis is structured as follows: Chapter 2 gives an overview over the experimental setup as well as techniques employed in this work. Afterward, the scientific results are presented, which are divided into three parts. Chapter 3 is dedicated to the alumina film. The structure of the oxide film was characterized by atomically resolved STM images. Furthermore, STM, STS and conductance imaging were used to investigate the correlation between the geometric and electronic structure of oxide defects, specifically antiphase domain boundaries (APDB). The latter are regularly appearing line defects of the oxide film, which play an important role for the nucleation of metal clusters [37] and the decomposition of NO [49]. The adsorption behavior of the alumina film toward single metal adatoms (Ag, Au) is described in Chapter 4. Such studies can be very helpful to compare the properties of oxide films and bulk oxides, as shown recently by density functional theory (DFT) calculations [50]. These theoretical studies predict different adsorption behavior for thin MgO films on Mo(100) and bulk MgO, respectively, toward metal adatoms with high electron affinity (e.g. Au). The results shown in Chapter 4 elucidate this question for the first time experimentally for an oxide film with a wide band gap. Chapter 5 presents STM studies on metal clusters (Ag, Pd) on the thin alumina film. The differential conductance through the clusters is investigated dependent on their size, revealing a series of equally-spaced resonances. The effect can be either ascribed to intrinsic cluster properties or to phenomena inherent to the experimental setup, namely tunneling through a double-barrier junction. Both possibilities are discussed in detail.

Chapter 2

Methods and Experimental Setup

This chapter aims to present the basics and the potential of scanning tunneling microscopy (STM) as well as the experimental realization. Within the scope of this work, the scanning tunneling microscope was operated mainly in three different modes: constant current imaging, scanning tunneling spectroscopy (STS) and conductance imaging. Apart from explaining principles and theoretical approaches for each method, special importance is attached to phenomena which are specifically related to the systems investigated here. This concerns, for instance, tunneling through thin oxide films or imaging of samples with large corrugation, as encountered for three-dimensional (3D) metal clusters. Finally, the experimental setup and the sample preparation are presented.

2.1 Scanning Tunneling Microscopy

2.1.1 Introduction

The invention of scanning tunneling microscopy by Binnig and Rohrer in the year 1982 [51] can certainly be regarded as the beginning of a novel era of surface science, since it enabled the local investigation of geometric and electronic properties of surfaces with unrivaled spatial resolution. This new technology was awarded with a Nobel prize only four years later, and rapid advancements in this field followed. On the one hand, STM-based analogs to conventional averaging spectroscopic techniques were developed, allowing to locally study sample properties. Fascinating examples include STS [52], inelastic tunneling spectroscopy (IETS) [53] and photon emission spectroscopy performed with a photon STM (PSTM) [54, 55]. STS and conductance imaging could be used, for instance, to study the local density of states (LDOS) of confined electron systems, thus visualizing basic principles of quantum mechanics [56–60]. IETS provided

vibrational spectra of single adsorbed molecules [53, 61–63], not obtainable otherwise; and photon emission STM could be used, for instance, to detect plasmon resonances of single metal clusters [64, 65]. Accomplishing STM in an external magnetic field with appropriate tips, spin-polarized tunneling and mapping of magnetization are possible [48, 66, 67]. Another key feature of STM is the possibility of atom and molecule manipulation, which has a certain potential in the emerging field of molecular electronics [57, 60, 68].

This short presentation of some highlights only scratches the surface of the numerous applications of STM, and one has to bear in mind that STM can also be performed in different environments (in liquids, in air) at various temperatures. Especially with regard to heterogeneous catalysis, quite an effort has been made to study dynamic processes, such as diffusion of atoms or defects [11, 69, 70]. A detailed overview over capabilities of STM can be found in [71].

2.1.2 Principle

The functionality of STM is based on the quantum mechanical tunneling effect of electrons, saying that an electron can overcome a finite energy barrier even if the latter exceeds its potential energy. In practice, this barrier is the vacuum which separates a

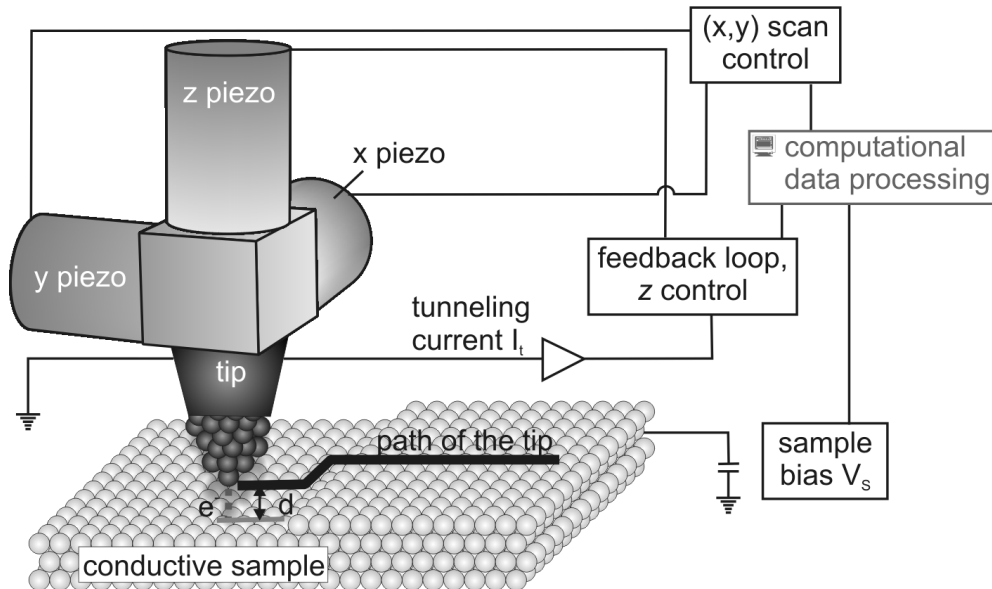


Figure 2.1: Schematic setup of a scanning tunneling microscope.

metallic tip from the conductive sample. If a bias voltage is applied between tip and sample, a current will be observed prior to electric contact between the two electrodes. This so-called tunneling current I_t drops exponentially with the distance d between tip

and sample. Typically, d is in the range of a few Å for tunneling currents of some pA or nA. Such small distances can be adjusted with piezo ceramics, which are also used for the lateral displacement of the tip. The piezo responsible for the height correction is referred to as z piezo in the following, the others as x and y piezo. The STM setup is shown schematically in Fig. 2.1. Basically two scan methods can be distinguished. In the *constant current mode*, I_t is kept constant by a feedback loop, and the recorded signal is the motion of the z piezo, regulated by the controller. In the *constant height mode*, the tip is kept at constant distance over the sample during the scan process, and I_t is recorded. The advantage of the latter technique is its increased scan speed which is especially important for the study of dynamic processes. However, its applicability to samples with large corrugation is limited. Therefore, we operated our STM exclusively in the constant current mode for imaging the sample.

2.1.3 Theoretical Approaches

An exact theoretical description of STM is extremely difficult because of the lack of translational symmetry of the tunneling junction and the variety of contributing factors. The tunneling process is mainly determined by the electronic states of the tip and the sample, but also by the sample bias V_s , the tip-sample separation d and the tip shape. Not all of these parameters are known or can be taken into account correctly. Thus, theoretical models underly permanent refinement [72, 73].

Many approaches trace back to a model of Bardeen which describes electron tunneling in a layer system consisting of a metal, an insulator and a superconductor by one-dimensional perturbation theory [74]. Here, both electrodes are considered to be independent from each other with known eigenfunctions. According to Bardeen, the electron tunneling between the two electrodes can be regarded as transition from an initial to a final state, whereby the transition probability obeys Fermi's golden rule. Tersoff and Hamann extended this theory to describe electron tunneling in STM junctions [75, 76]. Their main additional assumption concerned the nature of the tip, which was considered to have s -character. Thus, they could calculate transition matrix elements and show that the tunneling current is proportional to the local density of states (LDOS) of the surface at the position of the tip. Later models considered also p_z and d_{z^2} states of the tip [72, 77] which often provides a better description of STM images.

Equation (2.1) shows an analytical expression for the tunneling current, I_t , based on a generalized form of the Tersoff-Hamann model [28, 73].

$$I_t \propto \int_{-\infty}^{\infty} \varrho_s(E) \varrho_t(E - eV_s) T(d, E, eV_s) [f(E - eV_s, T) - f(E, T)] dE \quad . \quad (2.1)$$

According to this, the tunneling current I_t can be understood as convolution integral

of the LDOS of the tip (ϱ_t) and the sample (ϱ_s). Characteristic tip properties, such as the shape and the symmetry of the electronic states, are contained in ϱ_t . $T(d, E, eV_s)$ is the transmission coefficient describing the tunneling probability [75, 78, 79], which depends on the work functions of tip (Φ_t) and sample (Φ_s), the tip-sample separation d , the energy E and the sample bias V_s as follows:

$$T(d, E, eV_s) = \exp \left(-\frac{2d\sqrt{2m}}{\hbar} \sqrt{\frac{\Phi_s + \Phi_t}{2} + \frac{eV_s}{2} - E} \right) \quad . \quad (2.2)$$

In Eqn. (2.1), f is the Fermi distribution function describing the energy distribution at a temperature T . At temperatures close to 0 K, i.e. $k_B T \ll eV$, f can be approximated by a step function, and Eqn. (2.1) simplifies to:

$$I_t \propto \int_0^{eV_s} \varrho_s(E) \varrho_t(E - eV_s) T(d, E, eV_s) dE \quad . \quad (2.3)$$

It is important to point out that the description of electron tunneling by perturbation theory implies a weak tip-sample interaction and thus large separations d . Thus, the validity of Eqns. (2.1) and (2.3) is somewhat limited, and further models use scattering theory to overcome this constraint [73, 80]. However, it could be demonstrated for some oxide films, that the Tersoff-Hamann approach provides a good description of imaging properties even at small tip-sample separations [81]. Therefore, the scattering theoretical approach is not discussed here in more detail.

A different theoretical model is also necessary if eV_s exceeds Φ_s and Φ_t , i.e. in the field emission regime (Fowler-Nordheim regime [82]). Here, electron standing waves can form between tip and sample, leading to field emission resonances of the current [83, 84]. The oscillations of I_t with V_s depend on the local work function and the image force potential [71] and can thus be influenced by the chemical composition of a sample and/or potential variations at the surface [85, 86].

2.1.4 STM on Thin Oxide Films

As seen in the previous section, a variety of factors contribute to contrast formation in STM images, which makes their interpretation often difficult, even for “simple” tunneling junctions consisting of a metallic tip, a vacuum barrier and a metal surface. More complications arise for oxides and thin oxide films because of their band gap and/or insulating character. Generally, such oxidic materials are suited for STM investigations only if no sample charging occurs. In the case of bulk oxides, this condition can be met at elevated temperatures [87, 88] or for bulk conductive materials such as titania [10], where the conductivity arises from defects. Otherwise, oxides with wide band gaps can

be grown as thin films on conductive substrates [28, 89, 90]. Here, charging is avoided when electrons overcome the oxide barrier sufficiently fast, which implies that the film thickness is limited. The influence of the film thickness on electronic and imaging properties has been studied systematically for several systems, e.g. for NaCl films on Al(111) and Al(100) [81] and for MgO films on Ag(100) [91]. Accordingly, band gaps as large as in the corresponding bulk oxide are already reached for 2–3 monolayer (ML) thick films. They are still conductive and can often be imaged with atomic resolution. However, a detailed theoretical description of tunneling processes on thin oxide films is still lacking. Such tunneling junctions consist of two electrodes (tip and metal substrate) separated by two barriers: the vacuum and the oxide film. The situation is visualized in Fig. 2.2. The oxide layer can be considered as perfect dielectric, i.e. the electric field \vec{E} drops linearly across this layer dependent on V_s , leading to a bending of the oxide valence and conduction band, VB and CB, respectively.

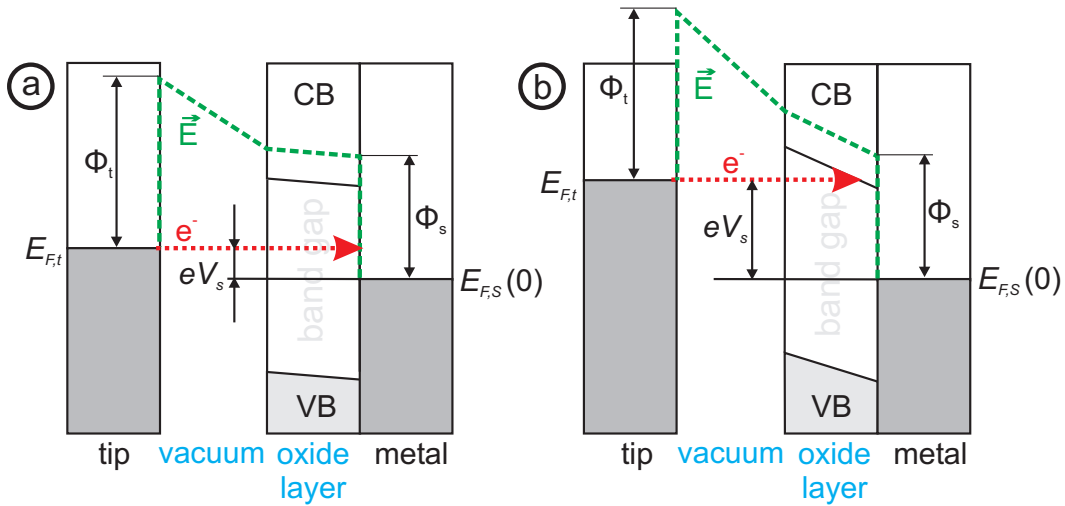


Figure 2.2: Potential energy scheme of a tunneling junction, consisting of a metallic tip, a vacuum barrier and a thin oxide film on a metal. The oxide layer can be considered as perfect dielectric, i.e. the electric field \vec{E} drops linearly across this layer dependent on V_s , leading to a bending of the oxide valence (VB) and conduction (CB) band. The situation is depicted for (a) low and (b) high sample bias V_s . At low V_s , only metal states are expected to contribute to the tunneling current, while oxide states should be accessible by STM only at higher V_s .

Phenomenologically, two scenarios can now be distinguished for electron tunneling. If V_s is chosen within the oxide band gap, close to the Fermi level, E_F , oxide states would not contribute to the tunneling current. Instead, STM should be sensitive only to states of the metal substrate or of the interface. This supposition seems to be supported by the finding of a reduced apparent thickness of oxide films for small V_s [92]. On the other hand, we obtained atomically resolved images of a thin alumina film on NiAl(110) for small V_s . These images could be assigned to distinct layers of the

oxide film by comparison with a calculated structural model [1]. This suggests, that oxide properties can influence the tunneling matrix elements even at low bias, most likely due to an extension of metal states into the vacuum as a result of the atomic arrangement in the oxide (cf. chapter 3). Thus, oxide states can (but do not need to) be indirectly probed by STM even at low V_s , enabling atomic resolution. Nevertheless, the determination of oxide film structures only from STM experiments remains almost impossible so far, because the underlying contrast mechanisms do not follow a general rule. It is often unclear, whether cations or anions dominate the tunneling and produce the contrast [10, 81].

If V_s is chosen outside the oxide band gap (Fig. 2.2 b), oxide states are directly accessible by STM. The apparent height of the film is then in the range of the real film thickness [92]. Usually, no atomic resolution can be obtained under these tunneling condition because of the large distance between tip and sample.

2.1.5 Imaging of Supported Metal Clusters

If STM is applied to samples with large corrugation, e.g. supported 3D metal clusters, care has to be taken when extracting geometric parameters. STM images represent a convolution of tip and sample states, hence the tip shape strongly influences the apparent lateral extension of adsorbates on the surface. This is shown schematically in Fig. 2.3 for 3D metal clusters with the shape of a hemisphere (a) and a prism (b). The cluster diameters d_c are not imaged correctly because electrons tunnel from different parts of the tip depending on where the latter is placed with respect to the cluster center. Thus, the cluster diameters $d_c^*(r_t)$ measured with STM depend strongly on the tip radius r_t (assuming the tip end to be spherical).

The knowledge of d_c is often essential, e.g. for a proper description and understanding of the electronic properties of clusters. However, r_t is usually not accessible. Therefore, the measured values $d_c^*(r_t)$ have to be corrected otherwise. One possibility is to compare the amount of deposited metal with the amount determined from STM images. For that purpose, the cluster volume is calculated from the measured values h_c and $d_c^*(r_t)$, assuming all clusters to have the same shape. The correction factor $g = d_c/d_c^*(r_t)$ can then be determined by comparison of apparent and real metal coverage.

While the determination of cluster diameters with STM is always problematic, the height h_c can usually be obtained with good accuracy. However, h_c is bias dependent for substrates with a band gap [92], i.e. for most thin oxide films. Therefore, V_s has to be chosen outside the band gap in these cases.

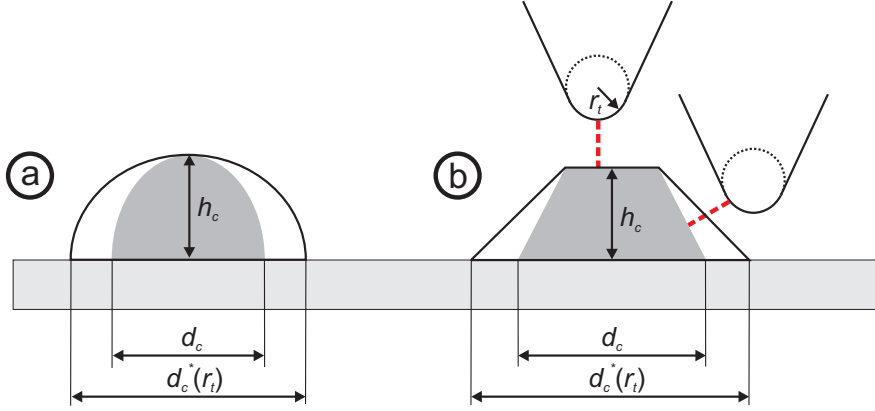


Figure 2.3: Scheme showing the tunneling junction for supported, 3D metal clusters having the shape of a hemisphere (a) or a prism, i.e. with a flat top facet (b). While the height h_c of the clusters appears correct for sufficiently large V_s , the cluster diameter d_c is imaged too large. The measured diameter $d_c^*(r_t)$ depends strongly on the radius r_t of the tip.

2.2 Scanning Tunneling Spectroscopy

2.2.1 Principle and Theory

The sensitivity of STM to the LDOS can be used to determine the electronic structure of a sample surface in an energy range of some eV. As seen in section 2.1.3, the tunneling current detected by STM reflects the integrated LDOS of the sample. To avoid this integration and to obtain the LDOS as a function of energy (i.e. eV_s), a spectroscopic mode called scanning tunneling spectroscopy (STS) can be used. Sometimes, this expression is used as generic term for all spectroscopic methods performed with a scanning tunneling microscope. Following another common nomenclature, we will use it as synonym for conductance (dI/dV) spectroscopy. The first detailed theoretical treatment was accomplished by Tersoff and Hamann [75, 76] for a spherical tip with s -character. Differentiation of the generalized form (2.3) provides:

$$\begin{aligned}
 \frac{dI(eV_s)}{dV_s} &\propto \varrho_s(eV_s) \varrho_t(0) T(d, E, eV_s) \\
 &+ \int_0^{eV_s} \varrho_s(E) \frac{\partial}{\partial V_s} \varrho_t(E - eV_s) T(d, E, eV_s) dE \\
 &+ \int_0^{eV_s} \varrho_s(E) \varrho_t(E - eV_s) \frac{\partial}{\partial V_s} T(d, E, eV_s) dE \quad (2.4)
 \end{aligned}$$

The last two addends (integrals) become small compared to the first one for small V_s . Hence Eqn. (2.4) simplifies to:

$$\frac{dI(eV_s)}{dV_s} \propto \varrho_s(eV_s) \cdot T(d, eV_s) \quad (2.5)$$

This shows that the differential conductance dI/dV is proportional to the sample LDOS if the transmission function is monotonous. Certainly, the theory by Thersoff and Hamann is based on several assumptions which are not always met experimentally, and later theoretical models try to overcome these simplifications by e.g. considering the influence of tip states [93]. Nevertheless, the Thersoff-Hamann theory provides a good phenomenological description of STS data.

It can be concluded from these theoretical considerations that STS provides similar information as ultraviolet photoelectron spectroscopy (UPS), however with the advantage of spatial resolution. On the other hand, not all information accessible by UPS can be obtained by STS. So, it is not possible to accomplish angle-resolved studies with STS, thus this techniques has no resolution in the k -space. In contrast, angle resolved UPS (ARUPS) is well-established. Furthermore, only those states can be probed by STS, which extend sufficiently into the vacuum. As a result, it is often difficult to study occupied states which are much more contracted than unoccupied ones.

Experimentally, various modes have been proposed to measure the differential conductance. All of them have in common, that they use a lock-in-amplifier, which adds a modulation voltage V_{mod} to the sample bias and then detects the differential conductance dI/dV . This technique was established by Feenstra *et al.* [52]. The difference in various STS operation modes concerns the adjustment of the tip-sample separation, which can be kept constant [52] or varied in a specific way (linear ramp, constant gap resistance, constant current). Advantages and disadvantages inherent to each method can be found in a recent review article [28]. All dI/dV spectra presented in this work are recorded with disabled feed-back loop at constant tip-sample distance. This permits to take spectra across $V_s = 0$. The lock-in amplifier was typically operated with $V_{mod} = 10 - 20$ mV (rms) and $f_{mod} = 300 - 700$ Hz.

2.2.2 Spectral Resolution

The peak width, ΔV , of dI/dV spectra has mainly three components: the intrinsic width ΔV_i of the peak, which is broadened by ΔV_T and $\Delta V_{V_{mod}}$ arising from the finite temperature and the bias modulation, respectively [94]. These factors contribute to ΔV as follows:

$$\Delta V = \sqrt{(\Delta V_i)^2 + (\Delta V_T)^2 + (\Delta V_{V_{mod}})^2} \quad , \quad (2.6)$$

whereby each width corresponds to the full width at half maximum (FWHM). ΔV_i

is mainly determined by the natural line width and by tip-induced broadening. The influence of the latter factor can be estimated by comparing spectra recorded with different tips. The thermal broadening, ΔV_T , can be derived from Eqn. (2.1), where the Fermi function $f(E) = [\exp(E/k_B T) + 1]^{-1}$ reflects the energy distribution at a temperature T . As shown in detail in [95], the derivative dI/dV can be approximated by a Gaussian distribution with a FWHM of $2\sigma = 3k_B T/e$, thus:

$$\Delta V_T = 3k_B T/e \quad . \quad (2.7)$$

The operation temperature of our microscope is ~ 5 K. According to Eqn.(2.7), the thermal broadening is here ~ 1.3 mV and can be neglected for the spectral features investigated in this work. To evaluate the influence of the modulation voltage, the signal of the amplifier has to be analyzed. As demonstrated in [96], the FWHM of the broadening function is $\sim 0.87 V_{pp}$, whereby V_{pp} is the peak-to-peak voltage of the modulation. This corresponds to an rms-value of $2 \cdot 0.87 \cdot \sqrt{2} \cdot V_{mod} \approx 2.5 V_{mod}$. Hence

$$\Delta V_{V_{mod}} = 2.5 V_{mod} \quad . \quad (2.8)$$

Typical modulation voltages used in this work are 10–20 mV (rms). They lead to a broadening of 25–50 mV. The peak width

$$\Delta V = \sqrt{(\Delta V_i)^2 + (3k_B T/e)^2 + (2.5V_{mod})^2} \quad (2.9)$$

is therefore mainly determined by the intrinsic peak width and by the modulation voltage for the chosen experimental conditions.

2.2.3 Probing LDOS with STS

STS is a powerful technique to investigate the electronic structure of surfaces and adsorbates on surfaces. Depending on the physical background, different mechanisms are responsible for the dI/dV signature. In the following, a brief overview is given over phenomena observable with STS, and a simple model for STS on adsorbates on thin insulating films is presented.

Electronic Properties of Surfaces

Because of its sensitivity to the LDOS, STS can be used to determine several characteristic surface properties, such as surface states, adsorbate electronic structures and band gaps in semiconductors and in thin insulating films [28, 52, 97]. A vast amount of STS studies address surface states, which occur on surfaces with a projected bulk band gap, such as noble metal (111) surfaces. Surface states show up as distinct step in

dI/dV spectra, related to the onset of the free-electron like band. STS can be used to determine the band onset energy for occupied and unoccupied surface states, which is not accessible by non-local methods, i.e. photoelectron spectroscopy (PES). Moreover, it is possible to study surface states in confined systems and their lifetimes [59, 98–100].

Band gaps are manifested by regions of vanishing dI/dV intensity around E_F . To determine the correct gap size, it is important to take band bending effects into account. Thin insulating films can be regarded as dielectrics where an applied potential drops linearly in the film. This effect is schematically shown in Fig. 2.2. As a consequence of electric-field induced band bending, band gaps determined by STS are slightly too large dependent on the dielectric properties of the layer. The situation is more complicated for semiconductors because of non-linear band bending effects [88]. This issue is, however, not important for this work and will not be further discussed.

Another field, where STS offers clear advantages, is the investigation of surface defects. They often exist only in low concentration and can therefore barely be studied with integrating techniques, though they might change the properties of surfaces drastically. STS can provide local information on, for instance, discrete electronic states induced by defects (cf. Chapter 3) or their scattering behavior with respect to surface states.

Electronic Properties of Adsorbates

The interactions between adsorbates (adatoms, clusters, molecules) and surfaces are manifold with regard to mechanisms and strength. Consequently, STS is used to investigate a variety of different phenomena and properties, such as the Kondo effect, electronic levels of adatoms and clusters, as well as HOMO/LUMO and vibronic states of molecules. In the following, a brief overview is given, starting with investigations on metallic surfaces and followed by examples for inert substrates with special focus on thin insulating films.

On metal substrates, a vast number of studies is dedicated to the Kondo effect, evoked by magnetic adatoms on non-magnetic metal surfaces [59, 101, 102]. Magnetic impurities lead to divergence of the electrical resistance as the temperature approaches 0 K, and a minimum resistance exists for a non-zero temperature. This minimum resistance is due to interaction between the localized magnetic impurities and the itinerant electrons, and can be detected by STS, as dI/dV spectra recorded on such impurity atoms below the Kondo temperature reveal a narrow resonance close to the Fermi level. Fewer studies address the electronic structure of nonmagnetic adatoms and small clusters on metal surfaces [60, 103]. In this case, distinct resonances are only obtained if the adatoms or clusters are sufficiently decoupled from the substrate electronic states. Usually, only unoccupied states are detectable with energy levels in

the range of some eV, depending on the element and the interaction with the substrate. Quite fascinating results have been reported for metal (Au and Cu) adatoms and assembled, one-dimensional (1D) clusters on NiAl(110) [60, 104, 105] and Cu(111) [106], respectively. With increasing number n of chain atoms, the dI/dV signature changes from a distinct unoccupied resonance to an electron band with decreasing onset energy. Theoretical investigations have shown that such behavior can be described by a cylindrical [107] and a 1D [106] particle-in-a-box model on NiAl(110) and Cu(111), respectively. Thus, the electrons in the chain form a free electron gas, where the energy levels are given by:

$$E_n = E_0 + \frac{\hbar^2}{2m_{\text{eff}}} \left(\frac{\pi n}{l} \right)^2 \quad (2.10)$$

for 1D delocalization (m_{eff} is the effective electron mass and l the chain length). The observed resonances are suggested to originate mainly from s and p derived states [106, 108–110], whereby the weak coupling to substrate electronic states is ascribed to pseudo band-gaps in both NiAl(110) and Cu(111) projected parallel to the surface.

Electron confinement in metal clusters has been investigated on non-metallic substrates, e.g. for Ag and Au clusters on graphite [111], where 2D and 3D electron confinement were observed. The electronic coupling between adsorbate and substrate is usually less pronounced on inert surfaces, such as thin insulating films or graphite, than on metal substrates. In some cases, the coupling is so weak that specific adsorbate properties can be investigated by STS. This has been performed for different molecules on metal-supported thin insulating films, where the HOMO and LUMO [112] as well as vibronic states [45] could be detected. It was also possible to study the charge transport through adsorbed molecules [113, 114]. The involved tunneling processes are often quite complicated due to the double-barrier (vacuum and oxide film), and a *bipolar tunneling mechanism* (see below) was established by Ho and co-workers [113, 114]. STS studies, which characterize the interaction between oxide films and metal adatoms are still sparse [115, 116], though of high interest in terms of a fundamental understanding of preferential adsorption sites, nucleation behavior and diffusion properties (cf. Chapter 4). This point is addressed within the scope of this work, therefore possible mechanisms determining the dI/dV signature are briefly discussed in the following.

Fig. 2.4 shows potential energy schemes of a tunneling junction, consisting of a tip, a vacuum barrier and an adsorbate with discrete electronic states on a metal-supported oxide film for (a) positive and (b) negative sample bias. At positive sample bias, electrons tunnel from filled tip to empty metal states. As soon as eV_s meets the energy of a discrete state in the adsorbate, a resonant tunneling channel opens, leading to an increase of the differential conductance. At negative sample bias, the mechanism

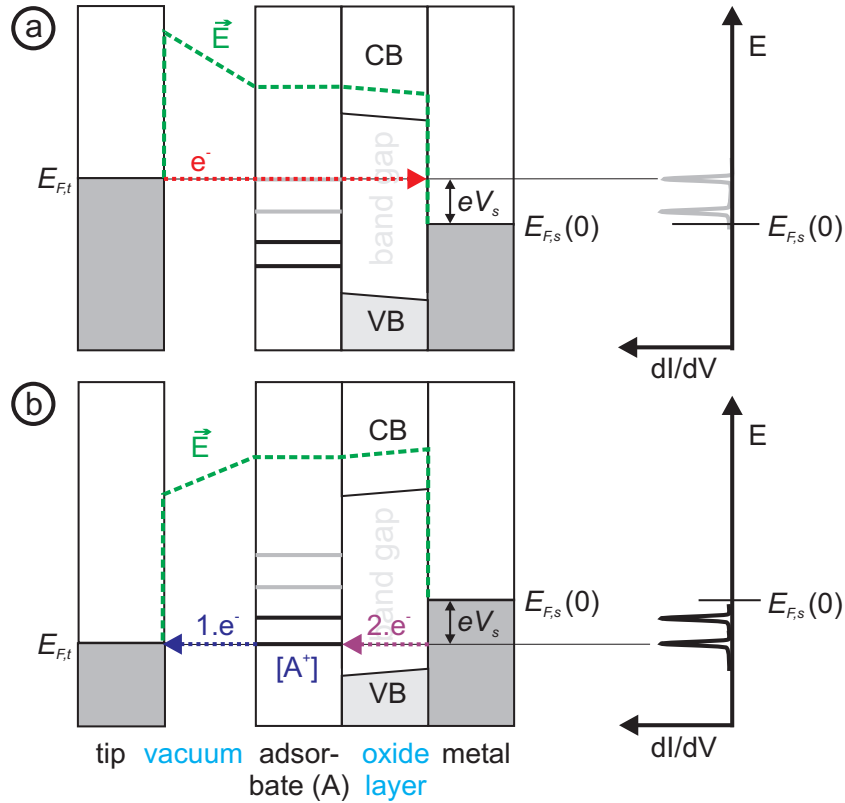


Figure 2.4: Schematic of the tunneling junction, consisting of the tip, the vacuum barrier and an adsorbate on a metal-supported oxide film. The electronic states of the adsorbate are assumed to be pinned with respect to the NiAl Fermi level. (a) If electrons tunnel from filled tip to empty sample states, an increased conductance is observed as soon as the energy eV_s equals the energy of a (discrete) adsorbate state. (b) Tunneling in the inverse direction is probably based on a two-electron process, where an electron tunnels from an occupied adsorbate state to an unoccupied tip states, leaving a charged transient state $[A^+]$ of the adsorbate. This empty state can then be filled with an electron from the NiAl. If, however, this process too slow, desorption of the adsorbate can occur.

is much more complicated. In this case, a two-electron process is likely because of the lower tunneling probability for electrons through the vacuum barrier than through the oxide film. Thus, electrons would first be drawn from the adsorbate and then refilled from the metal substrate, leading to a charged transient adsorbate state. Such states can be stable, as shown recently for Ag and Cs doped C_{60} molecules on a thin alumina film [46, 114]. Here, a resonance at an energy eV_s evokes a pair of dI/dV signals above and below E_F as a result of band bending in the thin oxide film and because of the stability of the charged species. Such bipolar tunneling mechanism can be excluded for single metal adatoms. Instead, tunneling out of filled states causes usually desorption of the adatom (cf. Chapter 4). Even if desorption occurs on a larger time scale than discharging of the ionic species (as observed for small Au clusters on the alumina film), occupied states are more difficult to detect by STS than unoccupied ones because of

their smaller extension into the vacuum. This requires shorter tip-sample separation, facilitating desorption.

2.2.4 Coulomb Blockade and Coulomb Staircase

If STS is applied to metal clusters supported on thin insulating films, some particularities have to be considered because the tunneling junction contains two barriers: the vacuum and the film. A potential energy scheme for such tunneling junction is shown in Fig. 2.5 (a), whereby the metal clusters are supposed to be large and to have continuous LDOS. The tunneling junction can also be understood in terms of an electric circuit which is depicted in Fig. 2.5 (b). It consists of three electrodes (tip, metal

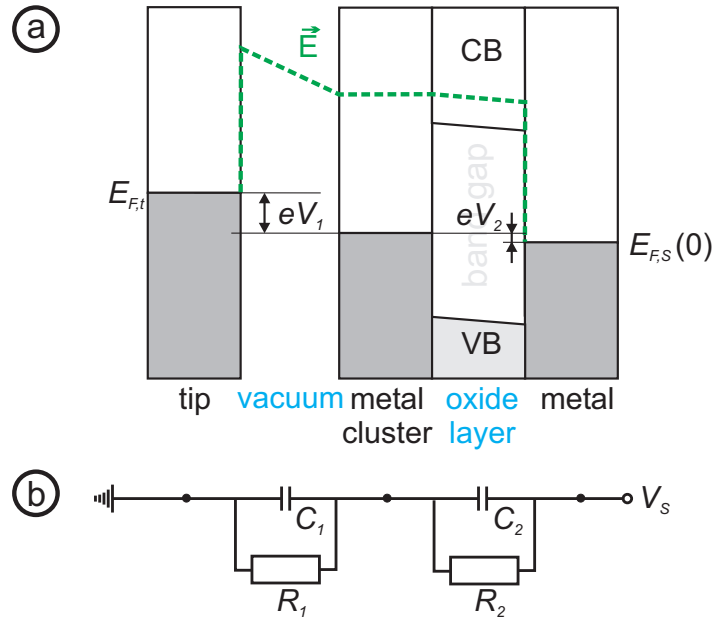


Figure 2.5: (a) Potential energy scheme for a tunneling junction, consisting of a tip and a metal cluster, supported on an oxide film on a metal substrate. Such junction contains three electrodes (tip, cluster, and metal substrate) which are separated by two gaps (vacuum and oxide film). The voltage drops by V_1 between tip and metal cluster and by V_2 between cluster and metal substrate. (b) Electric circuit which is equivalent to such junction.

cluster, metal support), separated by two barriers (vacuum and oxide film) that are each characterized by a resistance R_j and a capacitance C_j . If the electrostatic energy exceeds the thermal energy, i.e. if $e^2/2(C_1 + C_2) \gg k_B T$, the number of electrons on the center electrode (metal cluster) is fixed for constant bias. Applying an external voltage, V_s , the capacitances C_1 and C_2 must first charge to a certain threshold voltages before tunneling can occur. Depending on the ratio $(R_1 C_1)/(R_2 C_2)$, two phenomena can result from this charging: (i) If the time constants $(R_j C_j)$ for electron tunneling

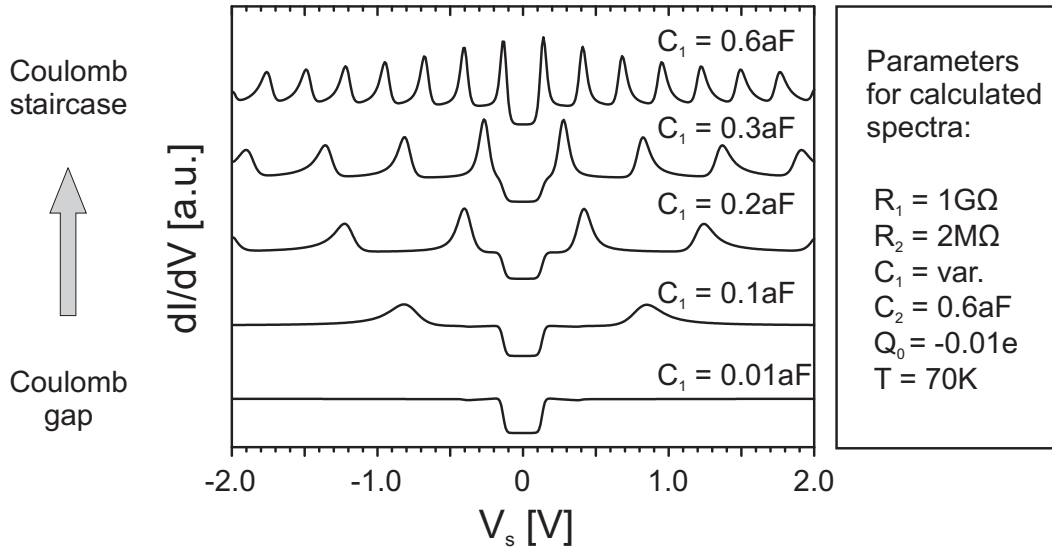


Figure 2.6: Calculated dI/dV spectra [122], which are characteristic for double barrier tunneling junctions (see Fig. 2.5). Different phenomena are observed, dependent on the resistances R_1 , R_2 and on the capacitances C_1 , C_2 . If $R_1 C_1 \approx R_2 C_2$, dI/dV spectra exhibit a characteristic dip (Coulomb gap) around $V_s = 0$. Otherwise, dI/dV spectra show equidistant peaks (Coulomb staircase in $I(V)$ spectra).

across each barrier are similar, the differential conductance shows a characteristic dip (Coulomb gap) around $V_s = 0$ [117]. (ii) If the time constants, $R_j C_j$, are very different, the center electrode (metal cluster) is charged quickly to the equilibrium level by tunneling through one junction, but can only lose charge through the other junction slowly. The successive charging of the center electrode by an electron opens new tunneling channels, increasing the conductance of the junction in a quantized fashion with bias voltage, i.e. the tunneling current increases stepwise. Fig. 2.6 shows calculated dI/dV spectra, whereby the time constants ($R_j C_j$) are similar for the lower curve and differ increasingly for the upper curves. As a result, the spectra exhibit a Coulomb gap (bottom), which changes gradually into a Coulomb staircase (top). Experimentally, Coulomb blockade effects, i.e. gaps and staircases, were first observed for planar tunneling junctions [118, 119]. Later, theoretical descriptions for nanoscopic junctions followed [117, 120–122], which were confirmed by STM measurements [123].

To evaluate the tunneling current as a function of the sample bias, the tunneling rate $\Gamma_j^\pm(n)$ of electrons is regarded, whereby the sign, + or –, defines whether tunneling occurs to or from the cluster, respectively. The index j refers to the junction, i.e. $j = 1, 2$ (cf. Fig. 2.5). According to [122, 124] one obtains:

$$\Gamma_j^\pm(n) = \frac{1}{R_j e^2} \left(\frac{-\Delta E_j^\pm}{1 - e^{\Delta E_j^\pm / k_B T}} \right) \quad , \quad (2.11)$$

where ΔE is the energy change of the system when an electron tunnels across the barrier. The center electrode is characterized by an excess charge, Q , which can be written in terms of an integer part $n \cdot e$ and a fractional charge Q_0 as: $Q = n \cdot e + Q_0$.

¹ Taking furthermore $C_\Sigma = C_1 + C_2$, the energy changes ΔE_j^\pm are given by:

$$\Delta E_1^\pm = \frac{e}{C_\Sigma} \left(\frac{e}{2} \pm (ne - Q_0) \pm C_2 V \right) \quad (2.12)$$

$$\Delta E_2^\pm = \frac{e}{C_\Sigma} \left(\frac{e}{2} \pm (ne - Q_0) \mp C_1 V \right) \quad (2.13)$$

and the tunneling current can then be written as:

$$I(V) = e \sum_{n=-\infty}^{\infty} \sigma(n) \cdot [\Gamma_2^+(n) - \Gamma_2^-(n)] = e \sum_{n=-\infty}^{\infty} \sigma(n) \cdot [\Gamma_1^-(n) - \Gamma_1^+(n)] \quad . \quad (2.14)$$

Here $\sigma(n)$ is the ensemble distribution of the number of electrons on the center electrode. Equation (2.14) can be solved numerically considering that (i) the net probability for a transition between adjacent states is zero, i.e.:

$$\sigma(n) \cdot [\Gamma_1^+(n) + \Gamma_2^+(n)] = \sigma(n+1) \cdot [\Gamma_1^-(n+1) + \Gamma_2^-(n+1)] \quad , \quad (2.15)$$

and that (ii) the ensemble distribution $\sigma(n)$ is normalized:

$$\sum_{n=-\infty}^{\infty} \sigma(n) = 1 \quad . \quad (2.16)$$

The simulation of dI/dV spectra using Eqn. (2.14) is a good tool to elucidate whether a spectroscopic signature originates from Coulomb repulsion or not. However, the model assumes that the resistances R_j are constant during spectra acquisition. This assumption is never met experimentally. As a result of this, the intensity of features (peaks and gaps) can be considerably reduced close to the sample Fermi level, whereby this effect is most pronounced for large tip-sample distances (large V_s). The influence of the electrode geometry is difficult to estimate, especially for tip-vacuum-cluster junction, since both the tip and the surface area of the cluster are not perfectly planar. Examples for calculated dI/dV spectra and typical parameters are shown in Fig. 2.6.

¹The fractional charge, Q_0 , determines the symmetry of dI/dV spectra with respect to the sample Fermi level. If, for instance, $Q_0 \approx 0$, Coulomb gaps and staircases are symmetric around $V_s = 0$.

2.3 Conductance Imaging

Conductance (dI/dV) imaging is a method which aims to map the LDOS of a surface for a chosen bias voltage. Principle and theoretical background of this technique are the same as for STS. Experimentally, a small modulation voltage is added to the sample bias, and the differential conductance dI/dV is then detected with a lock-in-amplifier. The sample bias is kept constant and the feed-back loop closed during the scan process. This allows the simultaneous recording of constant current and dI/dV images.

A main application of this method is the investigation of standing wave patterns resulting from electron confinement on terraces, artificial quantum structures, clusters or islands [56, 59, 60, 98, 105, 111, 125]. Furthermore, conductance imaging is a valuable technique to study the electronic structure in the environment of local defects (point or line defects) [126, 127].

2.4 Experimental Setup

2.4.1 The UHV System

All experiments have been accomplished with a home-built low-temperature STM [128–131], which is operated in UHV. The UHV system is shown schematically in Fig. 2.7 and consists of three parts: the pendulum accommodating the microscope, the main chamber and a preparation chamber. The latter one is used for sample storage and sample preparation. It is equipped with a turbomolecular pump, an ion getter pump, a sputter gun, a sample heating on the basis of electron bombardment, an Omicron evaporator EFM 3T, a mass spectrometer and gas supply. Once the sample is prepared, it is transferred to the main chamber, where LEED and Auger electron spectroscopy can be used to check the long-range order, the cleanness, and the chemical composition of the surface. The main chamber has a separate pump system consisting of a titan sublimation pump, an ion getter pump and a turbomolecular pump which is switched off during operation of the STM. The base pressure during STM operation was in the range of $2 \cdot 10^{-10}$ mbar. A bellow connects the main chamber with a pendulum accommodating the microscope head. Such design was first realized by Eigler and co-workers [132]. The main advantage of this setup is its high stability against vibrational perturbations (see below) due to the low eigenfrequency of the pendulum of ~ 1 Hz. Sample transport between the three chambers is performed with mechanical transfer systems.

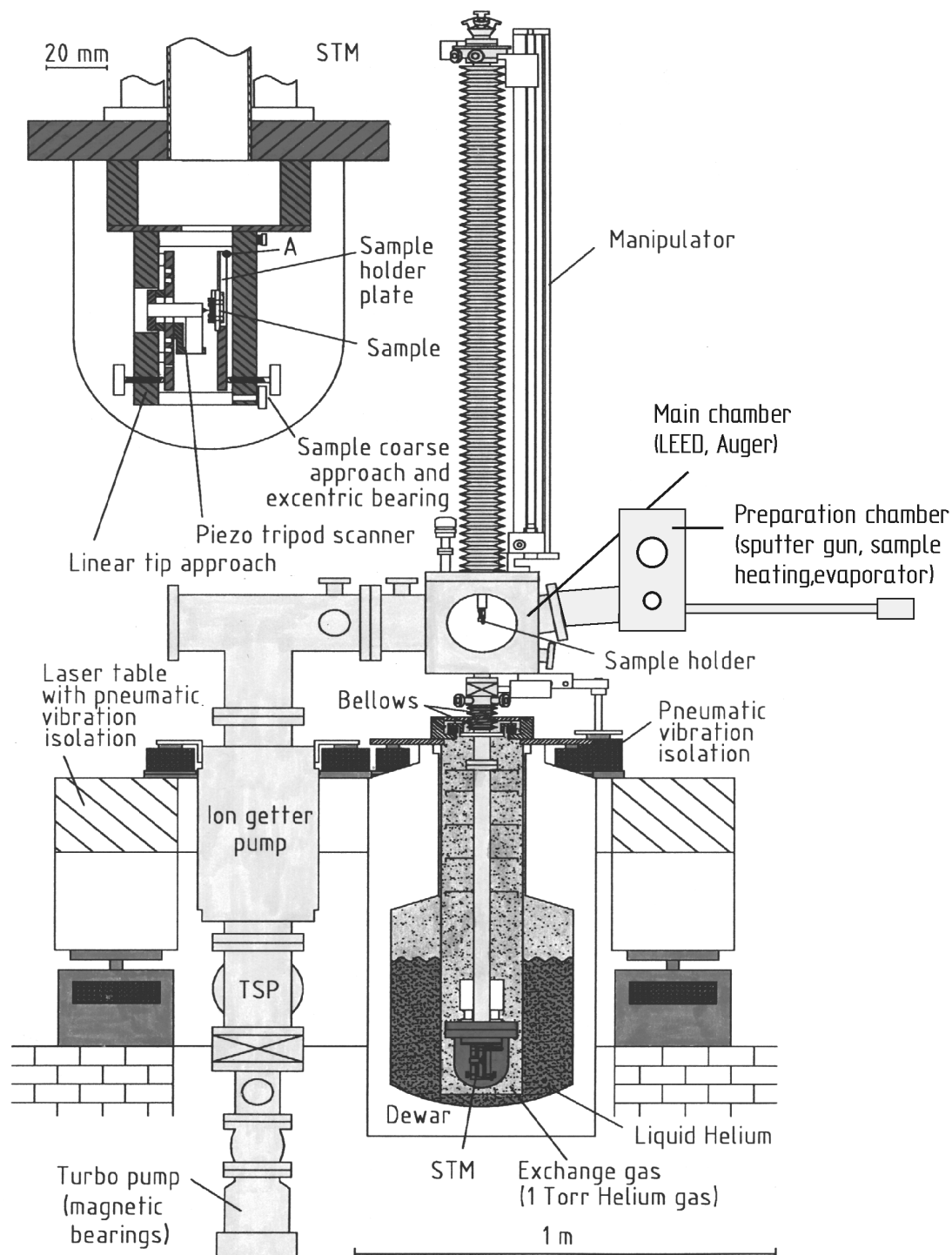


Figure 2.7: Schematic of the experimental setup of our home-built low-temperature scanning tunneling microscope. The design, where the STM is located at the bottom of a pendulum was first realized by Eigler and co-workers [132]. The inset on top shows the microscope head in more detail.

2.4.2 The Microscope Head

The microscope head contains devices which realize a coarse and a fine approach between tip and sample. The coarse approach is used to reduce the distance between tip and sample until both are in tunneling contact, while the fine approach is responsible for the tip motion during image acquisition. Both devices are briefly presented in the following.

The coarse approach in our STM is realized mechanically in contrast to most STM designs, which use piezo ceramics with relatively large strokes. The advantage of the mechanical approach is its high reliability at various temperatures. On the other hand, it is slower than piezo-based devices. The design is shown schematically in the inset of Fig. 2.7. Tip and sample are aligned horizontally. The tip is mounted onto a plate, which can be moved linearly in z -direction, i.e. toward the sample. In contrast, the plate bearing the sample performs an eccentric motion. This leads to a displacement in z direction. At the same time, the sample performs an elliptical motion parallel to the surface, such that a displacement in the (x, y) plane is realized. Both the sample holder plate and the tip plate are moved with screws which are driven by motors outside the UHV chamber. A detailed description of the coarse approach is given in [128, 129].

The fine approach of the tip is accomplished with a piezo tripod scanner. It consists of three PZT (lead zirconia titanate) tubes which are glued together such that they are oriented along x -, y -, and z -direction. The z -piezo is equipped with Macor plate containing a cannula, where the STM tip is plugged in. The tubes have an outer diameter of 6.13 mm, a wall thickness of 0.4 mm, and 24.5 mm (with 10 mm clamped). The application of a voltage leads to the extension of the piezo tubes along their axis, whereby field strengths of 2kV / mm result in an expansion of 0.15 % of their length at RT. At lower temperatures, the extension is smaller, and the maximum field which can be scanned in x, y -direction at 5 K has a size of about $1300 \text{ \AA} \times 1300 \text{ \AA}$.

2.4.3 Vibrational Isolation

Several parts inside and outside the UHV system serve for vibrational isolation, whereby each device covers a specific frequency spectrum. The penetration of acoustic waves (10–1000 Hz) is highly reduced by a massive acoustic chamber (delivered by IAC) which surrounds the whole instrument. Perturbations from lower frequencies (0.1–10 Hz) are transmitted mainly through vibrations of the building. Therefore, the UHV system is mounted onto a laser table, containing four pneumatic damping units.

To vibrationally decouple the pendulum (with the microscope) from the rest of the UHV chamber, several other devices are integrated. Thus, the pendulum is mounted onto a plate (supported on the laser table) via bellows, whereby the relative position

of the pendulum to the plate can be adjusted by the pressure in the bellows. The only further connection to the UHV chamber is another bellow, which rarely transmits vibrations. The plate with the pendulum is connected to the laser table via four small pneumatic damping units.

Finally, it is important that all stiff connection of the mechanical approaches of tip and sample can be decoupled to obtain a good vibrational isolation of the pendulum. A quantitative characterization of the damping performance is given in [128].

2.4.4 Cooling

The STM can be cooled down to 5 K. For that purpose, the pendulum is mantled with an exchange gas chamber containing gaseous He, which, in turn, is immersed into a dewar. Depending on the desired temperature T_s of the STM, the dewar can be filled with liquid N₂ ($T_s \sim 78$ K) or liquid He ($T_s \sim 5$ K). Temperatures between 5 K and 78 K can be adjusted by varying the He pressure in the exchange gas chamber [131]. Another possibility to warm up the microscope to a well-defined temperature between 5 and 40 K is resistive heating of a filament. The latter method usually provides faster temperature equilibrium. The measurement of the sample temperature is performed with a calibrated Si diode directly contacting the sample holder. As a control, another diode is mounted outside the vacuum on top of the microscope flange. Usually, both sensors display the same temperature in equilibrium condition, because of the good thermal connection of the microscope.

2.4.5 Electronics

The electronics used to control the operation of our low-temperature STM was built and developed at the Fritz-Haber Institute and is described in detail elsewhere [128]. A key element in STM operation is the I/V converter which amplifies the tunneling current in the range of some pA to nA by transformation into a voltage. The dI/dV converter used in this work can be operated with two different conversion factors, 10^7 V/A and 10^8 V/A. The cut-off frequency, where the intensity drops to $1/\sqrt{2}$ of its initial value, is ~ 600 Hz.

To detect the differential conductance in STS and conductance imaging, a commercial lock-in amplifier of the type EG&G 7260 was used. It can be operated in a range between 0.001 Hz and 250 kHz, the voltage sensitivity is 2 nV to 1 V.

2.5 Tip and Sample Preparation

2.5.1 Tip Preparation

Various materials are suitable for STM tips, and the choice depends mainly on the specific requirements (e.g. magnetic properties). Among the most common tip materials are W and Pt / Ir. Tungsten tips have good properties [72] and are easy to prepare by etching in an aqueous solution of NaOH. However, they get readily covered with an insulating oxide layer and are thus not suited to investigate oxide surfaces (unless the tip can be easily exchanged, what is not the case for our microscope design). Therefore we used Pt / Ir tips, which are very inert toward oxidation. These tips were obtained commercially, however it is also possible to etch or to cut a Pt / Ir wire.

Once the tip is integrated in the UHV system, it can be prepared *in situ* by (i) a controlled crash with a metal sample or (ii) by field emission. In the latter case, a high electric field (100–300 V/nm) is applied between tip and sample, the tip having negative polarity. This procedure leads to a rupture of the foremost parts of the tip. Here, a high resistance (10 M Ω) is integrated in the circuit to limit the current. Moreover, the I/V converter is disconnected.

2.5.2 Sample Mounting

The samples are metal single crystals with a diameter of 1 cm and a thickness of 2 mm, which are cut and polished in the crystal laboratory of the institute. The crystal is mounted onto a sapphire plate (15 mm \times 20 mm \times 2 mm), equipped with each two molybdenum bars and tantal sheets holding the sample. This mounting serves for the sample transfer and guarantees moreover a good thermal and electric connection in the microscope. The sapphire plate has a hole of 8 mm diameter in the middle, such that heating of the sample can be performed by electron bombardment from the back. The temperature can be measured with a thermocouple, whereby a Ni and a CrNi wire are twisted in a small hole of the crystal, then separated and thread through small holes in the sapphire plate.

2.5.3 Preparation of The Thin Alumina Film on NiAl(110)

The clean NiAl(110) surface was obtained by repeated cycles of Ar⁺ sputtering and annealing to 1300 K, whereby the quality of the surface was checked by LEED and STM. Afterward, the NiAl(110) sample was oxidized either partially or completely by dosing varying amounts of oxygen at 550 K and annealing to 1100 K for about 10 min [24]. For the completely oxidized alumina film 1200 L oxygen were dosed twice, while a single

dosage of ~ 150 L oxygen led to a well-ordered alumina film with patches of pristine NiAl. Such incomplete oxidation offers several advantages, e.g. with regard to tip preparation and examination of electronic properties of the tip. The long-range order of the film was again checked with LEED. Here, the alumina film has a characteristic pattern which is depicted in Fig. 2.8.

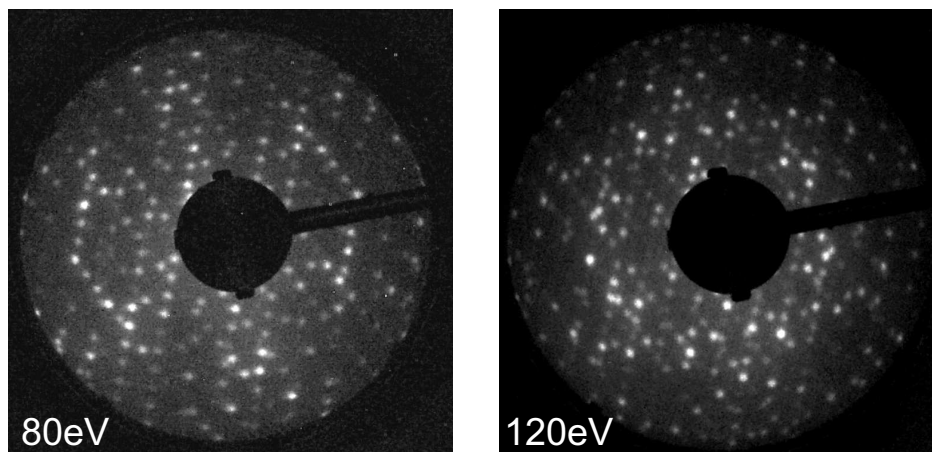


Figure 2.8: LEED pattern of the alumina film on NiAl(110), measured at two different energies.

2.5.4 Deposition of Metal Atoms and Clusters

Silver and palladium clusters were deposited at room temperature (RT) using an Omicron evaporator EFM 3T equipped with a crucible and a rod, respectively. The amount of deposited material was estimated from Ag/Pd deposition onto clean NiAl, where growth occurs in a layer-by-layer fashion. The coverage can then be determined directly from STM topographic images (Fig. 2.9).

The intended investigation of single metal atoms on a thin alumina film required the implementation of a new evaporator. Since most metal atoms are mobile and form clusters at RT, the evaporation has to be accomplished at cryogenic temperatures. The main requirement was therefore a compact design such that evaporation could be performed directly within the cooled part of the STM. For that purpose, a tungsten wire of a commercially available lamp was processed in the following way: the glass housing of the lamp was opened and the filament baked in vacuum. Afterward, a metal wire (Ag, Au) was wrapped around the tungsten filament and heated in UHV. Melting of the metal provided a homogeneously covered tungsten wire, from which Ag and Au, respectively, could be evaporated. After baking, these lamps were mounted in the STM head at ~ 1 cm distance from the sample. Gold and silver atoms could be deposited onto the surface by heating the described silver and gold-plated filaments, respectively.

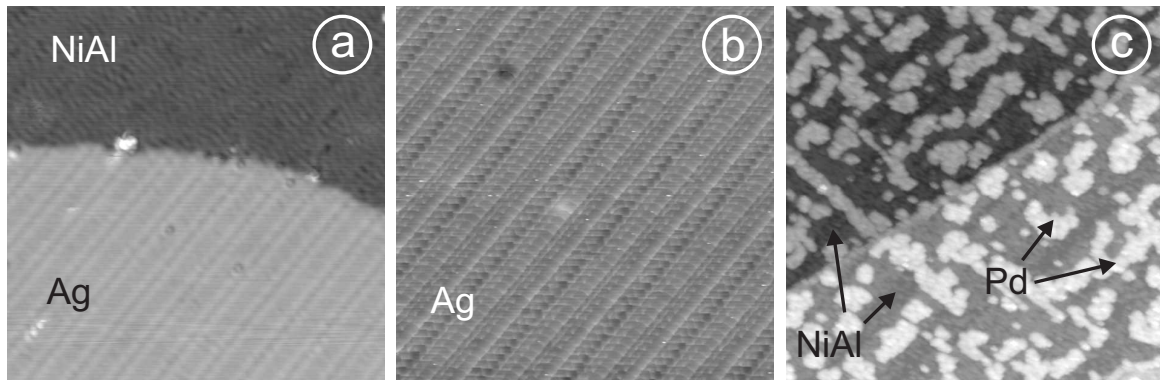


Figure 2.9: STM images of Ag (a-b) and Pd (c) on NiAl(110) at coverages of each ~ 0.5 ML. Deposition occurred at RT with an Omicron evaporator. Both metals grow on the NiAl layer by layer. (a) Ag overlayers can be easily distinguished from the NiAl substrate since they exhibit characteristic stripes along the NiAl [001] direction. They are shown with atomic resolution in (b). The image parameters are: (a) $V_s = 0.10$ V, $I_t = 2.5$ nA, $258 \text{ \AA} \times 258 \text{ \AA}$, (b) $V_s = 0.15$ V, $I_t = 2.5$ nA, $129 \text{ \AA} \times 129 \text{ \AA}$, and (c) $V_s = 1.0$ V, $I_t = 1.5$ nA, $1300 \text{ \AA} \times 1300 \text{ \AA}$.

During this procedure, the sample warmed up slightly from 5 K to 8 K (Ag) and 10 K (Au), respectively. The coverage was simply determined from counting the number of atoms in STM images (cf. Chapter 4).

Chapter 3

The Thin Alumina Film on NiAl(110)

During the last years, the thin alumina film on NiAl(110) attracted much interest as model for bulk alumina supports in heterogeneous catalysis [21]. Though the well-ordered alumina film is only 5 Å thick, it exhibits main properties of bulk Al₂O₃, notably a similar band gap of 7–8 eV [24, 25]. At the same time, the thin alumina film is conductive, allowing its investigation with methods such as STM or LEED. Charging, which is the main problem related to the study of bulk oxides, can be circumvented. Furthermore, the thin film decouples efficiently magnetic and electronic properties of adsorbates from the underlying NiAl [45, 48, 114] and has therefore high potential as support material in fields beyond catalysis, such as microelectronics and single molecule investigations. Despite its relevance, the structure of the film remained unresolved until very recently and should therefore be investigated within the scope of this work. The results of our STM studies on the pristine film [133] are presented in the first section of this chapter. They were crucial for the following theoretical work performed by Kresse and co-workers who could finally present a convincing structural model for the whole film [1]. The stoichiometry of the alumina film turned out to be Al₁₀O₁₃. Another important question connected with the thin alumina film concerned the structure of antiphase domain boundaries (APDB), which are regularly appearing line defects of this film [134]. These defects do not only play a central role for cluster nucleation [21, 135], but they also seem to have an increased reactivity, e.g. toward NO [49]. The determination of their electronic and geometric structure was therefore of great interest. Using STM and STS, it was possible to provide a detailed characterization of APDB and to resolve their structure [126, 133, 136]. These studies are presented in the second part of this chapter.

3.1 Growth and Orientation

Following the procedure described by Jaeger *et al.*, the oxidation of NiAl(110) leads to a well-ordered, atomically flat alumina film [24, 134]. The growth is commensurate only along the $[1\bar{1}0]$ direction of the NiAl substrate, but incommensurate along the $[001]$ direction. Due to the C_{2v} symmetry of NiAl(110), the alumina film grows on this substrate in two reflection domains A and B. These domains are tilted against the NiAl $[1\bar{1}0]$ direction by $\pm 24^\circ$. Size and orientation of the alumina unit cells with respect to the NiAl substrate are shown schematically in Fig. 3.1 (a). Fig. 3.1 (b) displays an STM image of the alumina film, where the two domains can be easily distinguished. Unit cells are marked with white rectangles.

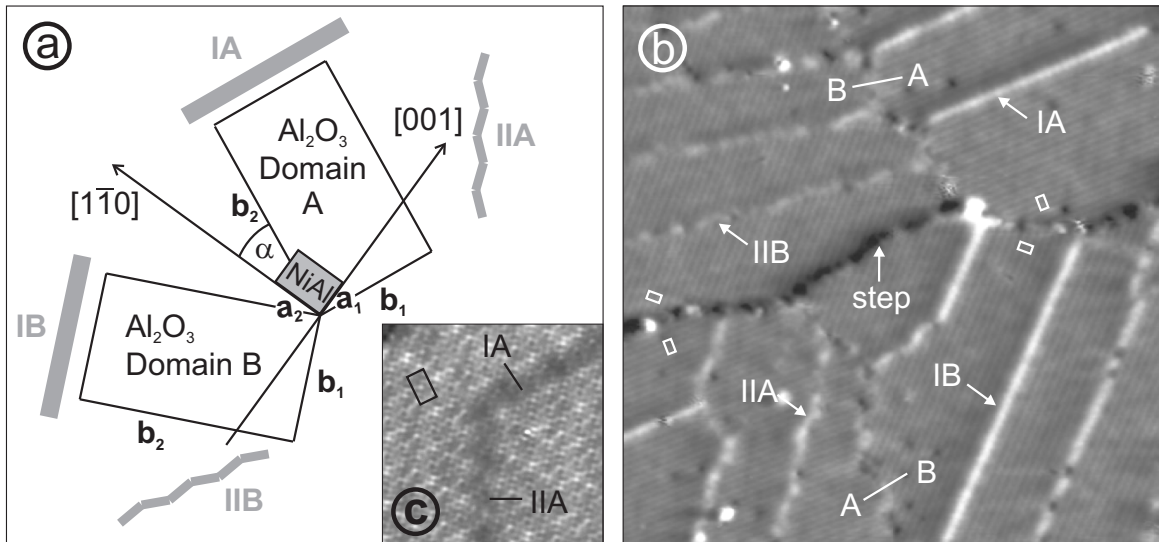


Figure 3.1: (a) Dimension of the alumina unit cell ($b_1 = 10.55 \text{ \AA}$, $b_2 = 17.89 \text{ \AA}$, $\alpha = 88.6^\circ$) and orientation with respect to the NiAl(110) substrate ($a_1 = 2.89 \text{ \AA}$, $a_2 = 4.08 \text{ \AA}$). The orientation and schematic structure of antiphase domain boundaries (APDB) are marked with gray lines. Four different types (IA, IB, IIA, IIB) can be distinguished. (b) STM image of the alumina film on NiAl(110) ($V_s = 4.5 \text{ V}$, $I_t = 0.5 \text{ nA}$, $378 \text{ \AA} \times 378 \text{ \AA}$). The z-signal was differentiated, thus both terraces appear on the same height. Size and orientation of the alumina unit cell are marked with a white rectangle in each domain. APDB appear as bright lines at the indicated sample bias. A straight (IA and IB) and a zigzagged (IIA and IIB) type can be distinguished for each domain. In contrast to reflection domain boundaries (A–B), each of them runs along a characteristic direction. (c) STM image with higher resolution ($V_s = -2.0 \text{ V}$, $I_t = 0.5 \text{ nA}$, $129 \text{ \AA} \times 129 \text{ \AA}$) of a straight (IA) and a zigzagged (IIA) APDB in the A domain.

3.1.1 Defects

The existence of two reflection domains as well as a slight lattice mismatch between NiAl substrate and alumina film leads to a characteristic network of line defects [134].

They appear as bright lines in the STM image in Fig. 3.1 (b). Two types of line defects can be distinguished on the alumina film: reflection domain boundaries separating the areas A and B and antiphase domain boundaries (APDB) between domains of equal orientation, i.e. A–A or B–B. The structure and the direction of the reflection domain boundaries are primarily determined by the growth of the domains A and B. They do not show local order and are not further discussed here. In contrast, APDB form very regularly with a mean distance of approximately 100 Å [134]. They run along two well-defined directions in each domain, which is schematically shown in Fig. 3.1 (a). When parallel to the short alumina unit cell vector (b_1), they appear as straight lines (IA and IB). In contrast, the thinner, zigzagged type follows the diagonal of the unit cell (IIA and IIB). Fig. 3.1 (c) displays an STM image of a straight and a zigzagged APDB with higher magnification. Both the geometric and electronic structure of APDB were central questions of this work. They are discussed in detail in section 3.3.

While line defects in the thin alumina can be easily detected by STM [134], point defects could not be observed. However, their existence was suggested by electron spin resonance and cathodoluminescence experiments [137]. Furthermore, systematic studies on the nucleation of various metals indicate the presence of point defects in a concentration of $\sim 1.2 \cdot 10^{13} \text{cm}^{-2}$ [37, 138, 139]. This work provides atomically resolved STM images of three out of four alumina layers. None of the images shows evidence for point defects. The thin alumina film was also investigated by conductance imaging, revealing its electronic structure. These studies did not provide indications for localized electronic states induced by point defects, neither. Therefore, their existence has to be doubted. A possible reason for the previously observed nucleation behavior might be the existence of preferential adsorption sites within the alumina unit cell.

3.2 Structure

Main structural features of the thin alumina film on NiAl(110) could be determined already in the beginning of the 1990s using of a variety of spectroscopic methods, such as ion scattering spectroscopy, electron energy loss spectroscopy, X-ray photoemission spectroscopy, angle-resolved ultraviolet photoemission spectroscopy and Auger electron spectroscopy [24, 134, 140]. According to these experiments, the film is built of two aluminum-oxygen layers and has a thickness of $\sim 5 \text{Å}$. The film is oxygen-terminated and accommodates at least two different Al species, indicating a structural similarity to $\gamma\text{-Al}_2\text{O}_3$ or $\kappa\text{-Al}_2\text{O}_3$, where Al is found in both tetrahedral and octahedral coordination. This resemblance and further structural investigations [133, 134, 141] led to several models which tried to assign the structure of the alumina film on NiAl(110) to known alumina bulk phases [142, 143]. However, these models did not account for all

observations made by STM [133]. Fig. 3.2 shows three atomically resolved STM images which were obtained at different tunneling conditions. None of these structures could be fully explained by the existing models. Certainly, it is often difficult to interpret STM images of thin oxide layers, because an intermixing of LDOS located in the oxide film and in the underlying metal support can occur. Under certain conditions, however, such an intermixing is not likely, for instance in the STM image of Fig. 3.2 (b). Here, the imaging properties of the metal tip are modified by an adsorbate, leading to supercorrugation. It can therefore be supposed that only one atom species (Al) close to the surface is imaged. At least in this case, a correct structural model should reflect the STM data. However, this was not the case. Only very recently, a model based on density functional theory (DFT) calculations was presented by Kresse and coworkers which is in agreement with all experimental findings [1]. This theoretical study uses the plane wave code VASP [144] and the PW91 gradient corrected functional [145]. The incommensurate growth of the alumina film along the [001] direction of the NiAl substrate could not be taken into account. Instead, a parallelogram-shaped $\begin{pmatrix} 5 & 1 \\ 2 & 7 \end{pmatrix}$ commensurate super-cell was used with twice the area of the oxide unit cell and 8 NiAl layers. These conditions correspond to unit cell parameters of $b_1 = 10.93 \text{ \AA}$, $b_2 = 17.90 \text{ \AA}$, and $\gamma = 88.16^\circ$. The resulting structural model showed that the STM images of Fig. 3.2 reflect directly the structure of distinct layers of the thin alumina film. Thus, three out of four layers are accessible by STM. In the following, this structure is described in detail, going from the bottom to the top of the film.

Fig. 3.2 (a) shows an STM image reflecting the symmetry of the interface aluminum (Al_i) layer, i.e. that layer which is closest (2.3 \AA) to the NiAl substrate. The sensitivity for this layer at small negative sample bias is quite astonishing and was ascribed to a special structural feature of the thin alumina film, namely to the fact that O atoms in the surface layer (O_s atoms) are located just above of these Al_i atoms. As suggested by simulations [1], this enhances the penetration of NiAl states into the vacuum and increases the tunneling probability. Thus, not the Al_i atoms are imaged but those oxygen atoms which have an Al_i underneath. Each alumina unit cell contains 16 Al_i atoms, which arrange in pentagon pairs and heptagons. They are marked in the STM image and in the model of Fig. 3.2 (a). According to calculations [1], this peculiar structure allows the Al_i atoms to be located close to Ni atoms, being energetically favorable as compared to Al neighbors. The affinity of Al_i atoms for Ni leads to row matching and hence commensurate growth along the $[1\bar{1}0]$ direction of NiAl, where Al and Ni rows alternate (the lattice parameter is $a_2 = 4.08 \text{ \AA}$, cf. Fig. 3.1). Al_i atoms are suggested to bind to Ni via p_z orbitals, leaving two electrons for anchoring the oxide film. Each Al_i atom is coordinated by three interface oxygen (O_i) atoms, as can be seen in the structural model in Fig. 3.2 (a). The latter shows only those two layers of

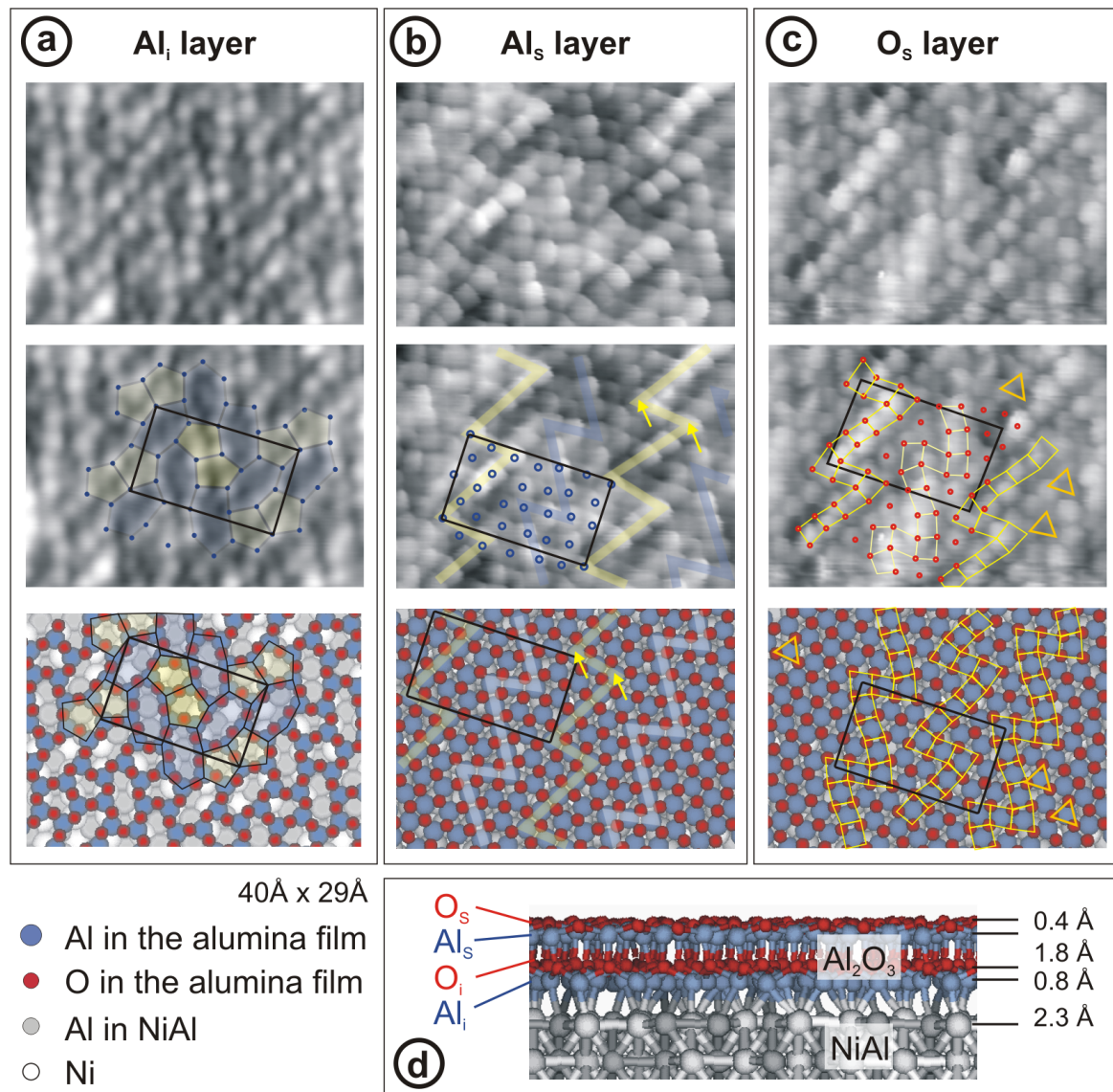


Figure 3.2: Structure of the thin alumina film on NiAl(110), investigated by STM and DFT calculations. The model was provided by G. Kresse [1]. Three of the four oxide layers are “accessible” by STM dependent on the tunneling conditions. (a) At a sample bias V_s of -50 mV and a tunneling current I_t of 0.5 nA, the interface aluminum (Al_i) layer is displayed, which consists of Al pentagon pairs and heptagons. The Al_i lattice is also shown in the model, together with the underlying NiAl and the interface oxygen (O_i) layer. (b) The surface aluminum (Al_s) layer can be imaged, if the tip properties are modified by an adsorbate atom or molecule ($V_s = 225$ mV, $I_t = 0.5$ nA). This layer exhibits a characteristic quasi-hexagonal structure, whereby the apparent corrugation is due to differently coordinated Al atoms. The zigzagged stripes mark Al_i atoms in pyramidal interstices (five-fold coordinated), whereby two per unit cell are strongly distorted (arrows). Other Al_s atoms are tetrahedrally coordinated. (c) The surface O layer (O_s) is accessible for very short tip-sample distances, e.g. $V_s = 12$ mV, $I_t = 1.2$ nA. Oxygen atoms are arranged in squares (yellow) and triangles (orange). (d) Model showing a side view of the oxide film.

the alumina film which are closest to the NiAl substrate. According to the model, the O_i layer has quasi-hexagonal symmetry and contains 24 O_i atoms per alumina unit cell. Presumably, it can not be imaged by STM. However, calculations suggest that the next Al layer is located exactly on top of the O_i layer, hence it has the same quasi-hexagonal symmetry and contains the same number of atoms (24) per unit cell. This surface aluminum (Al_s) layer can be imaged by STM under certain conditions, e.g. if the tip is modified by an adsorbate molecule. Fig. 3.2 (b) displays such an image. Apart from the quasi-hexagonal symmetry, the apparent corrugation of this layer is striking. It is most probably related to the different coordination of Al_s atoms. According to the model, half of them (12 out of 24 atoms per unit cell) are located in pyramidal interstices, i.e. they are five-fold coordinated by O atoms. These Al_s atoms form zigzagged rows, which are marked by yellow stripes in Fig. 3.2 (b). In the STM image, they seem to protrude out of the surface, especially those with a strongly distorted pyramidal coordination (2 per unit cell, marked with an arrow). The other half of the Al_s atoms are tetrahedrally coordinated and appear mostly smaller. At first glance, a pyramidal coordination of Al atoms seems to be unusual, since they are normally found in tetrahedral and octahedral interstices. However, a pyramid just corresponds to a truncated octahedron. Thus, the observed coordination is strongly related to that observed in several Al_2O_3 bulk phases. The mean Al_s - Al_s distance is $\sim 3.0 \text{ \AA}$ and thus in good agreement with Al-Al separations in surfaces of bulk Al_2O_3 [1]. The fact that Al_s atoms are found in both pyramidal and tetrahedral interstices is noteworthy, because that means that the terminating surface oxygen (O_s) layer, which is located $\sim 0.4 \text{ \AA}$ above the Al_s layer, does not have quasi-hexagonal symmetry as suggested in previous work [21, 24]. Such a hexagonal arrangement is typical for bulk Al_2O_3 was therefore considered likely in the case of the thin alumina film, too. However, a deviating structure where O_s atoms form both triangles and squares is proposed by the model of Kresse *et al.*. Indeed, such features are observed in STM if V_s is chosen in the range of a few mV (Fig. 3.2 c). These STM images are now ascribed to the O_s layer, which contains 28 atoms per alumina unit cell.

The stoichiometry of the alumina layer can be directly derived by counting the atoms per unit cell in each layer. This provides $Al_{16}O_{24}Al_{24}O_{28}$ which corresponds to $4(Al_4O_6Al_6O_7)$, i.e. to $Al_{10}O_{13}$. Thus, the film contains less oxygen than Al_2O_3 . This deviating stoichiometry can be explained by the formal charge of the Al_i atoms. The latter are coordinated to each three oxygen atoms, which in turn have three Al neighbors (2 Al_i and 1 Al_s). The formal charge of the Al_i atoms is given by the number of the oxygen atoms in the coordination sphere (3) times their formal charge (-2) divided by the number of coordinating species (3). Hence, Al_i atoms have a formal charge of +2. The third electron is used to bind to the underlying NiAl(110). Thus, this layer

anchors the film on the support. A more precise description of the film stoichiometry would therefore be $4(\text{Al}^{2+}_4\text{O}^{2-}_6\text{Al}^{3+}_6\text{O}^{2-}_7)$, also reflecting the charge neutrality of the thin alumina film. Moreover, the alumina film is not polar, in contrast to some other thin films, such as FeO on Pt(111) [86, 116].

3.3 Antiphase Domain Boundaries

3.3.1 Geometric Structure

Atomically resolved STM images were obtained for three out of four layers of the thin alumina film (Fig. 3.3). Based on these results, a complete structural model of APDB can be derived, allowing a correlation of geometric and electronic properties (cf. section 3.3.2). In the following, this is demonstrated in detail for straight APDB separating two B domains (type IB). Apart from orientation, these results do also apply to APDB of the type IA. A different structure is observed for zigzagged APDB. However, significant features determining their electronic properties are similar. Therefore, only some main structural aspects are discussed here.

Straight APDB

Fig. 3.3 shows atomically resolved STM images of different layers of a straight APDB, which is marked by a red arrow. Additionally, the structure was analyzed by G. Kresse and M. Shishkin [136] using the DFT plane-wave package VASP [144] to optimize the structure and to calculate the energetics. The supercell was constructed in a different way than that described for the pristine film. Here, a $\begin{pmatrix} 5 & -3 \\ 1 & 4 \end{pmatrix}$ NiAl cell with 23 elementary surface cells was used, whereby only 4 NiAl layers were considered. The shorter NiAl lattice vector was changed such that alumina film and NiAl were commensurate, and the substrate was not allowed to relax. A more detailed description of the applied methods is found in [136].

In the following, the structure of straight APDB is described layer by layer, starting at the bottom of the film and going to the top. Figure 3.3(a) shows an STM image of the Al_i layer, as identified by its characteristic pattern consisting of pentagons and heptagons. The displayed region contains a straight APDB (red arrow), where the symmetry of the unperturbed film is altered. Thus, the unit cell around the APDB is elongated. Furthermore, the series of pentagons and heptagons are pulled apart, such that Al_9 rings (nonagons) and heptagons are formed instead. However, it is questionable, whether all Al_i atoms can be visualized by STM, since the presence of nonagons would lead to undercoordinated oxygen in the next layer (O_i). This can be referred from the building principle of the alumina film described in Section 3.2 and

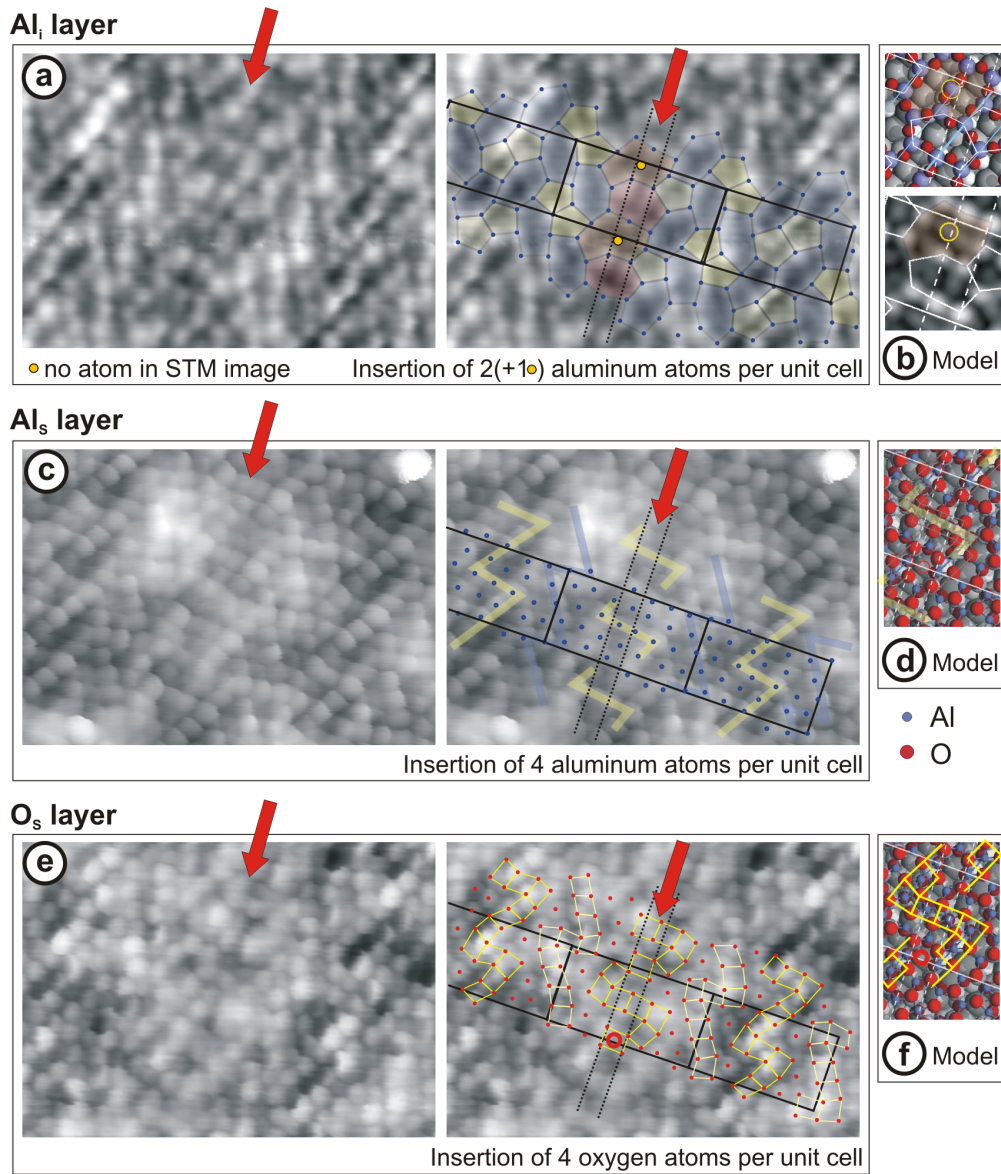


Figure 3.3: Structure of straight APDB (type IB) in different layers of the alumina film, investigated by STM (image size: $56 \text{ \AA} \times 40 \text{ \AA}$) and DFT calculations. The models (b), (d) and (f) were provided by G. Kresse [136]. Perfect and extended unit cells are marked with rectangles, the broken lines indicate the APDB. (a) STM image ($V_s = -50 \text{ mV}$, $I_t = 0.5 \text{ nA}$) reflecting the symmetry of the Al_i layer of the alumina film. The APDB is imaged as series of heptagons and nonagons. However, another Al_i atom might be present in each nonagon at the position marked by the orange circle, “invisible” for STM. (b) Model showing NiAl, Al_i and O_i layer (top). The corresponding simulation (bottom) of the LDOS probed by STM is based on the Tersoff-Hamann approach [76]. (c-d) STM image ($V_s = 225 \text{ mV}$, $I_t = 0.5 \text{ nA}$) and model of the Al_s layer, where one atom is inserted in direction of the long alumina unit cell vector. Bright lines indicate pyramidally coordinated Al_s atoms. (e-f) STM image ($V_s = 12 \text{ mV}$, $I_t = 1.2 \text{ nA}$) and model of the O_s layer. The red circle marks a position where O–O distances are very large.

from the symmetry of the Al_s layer (Fig. 3.3 c), which should correspond to that of the O_i layer. As a result, another Al_i atom would be located at the position marked with an orange circle. This assumption is also supported by DFT calculations. Here, structures with and without an additional Al_i were modeled, whereby the first one appeared to be more stable by ~ 3.2 eV. Fig. 3.3 (b) shows the resulting structural model (top) where the nonagon visible in STM is decomposed into a hexagon and a heptagon. The LDOS of this structure as probed by the STM can be simulated using the Tersoff-Hamann approach [76]. The result is displayed in Fig. 3.3 (b), bottom. Indeed, the added Al_i atom would not be visible in STM images. The reason for its invisibility is probably related to the imaging mechanism. As described above, Al_i atoms extend the LDOS of NiAl into the vacuum only if an O_s atom is located above. However, this is not the case for the questionable Al_i atom. Thus, the extended alumina unit cell of APDB contains most probably three additional Al_i atoms as compared to the normal cell, i.e. 19 instead of 16. However, only two of the three additional Al_i atoms can be visualized by STM. Fig. 3.3 (c) displays an STM image of the Al_s layer, as can be deduced from its quasi-hexagonal structure prevalent also in the APDB. A row of four Al_s atoms is inserted in the extended unit cell of the APDB [133], which hence contains 28 atoms. Bright stripes indicate pyramidally coordinated Al_s atoms in both the STM image (c) and the model (d). The structure of the O_s layer can also be directly referred from STM images. As shown in Fig. 3.3 (e), the extended unit cell of the APDB inhabits four additional O_s atoms, thus the unit cell contains 32 atoms. It is noteworthy, that some of them exhibit increased O–O distance. This position is marked by a red circle in the model.

The stoichiometry of straight APDB can be deduced directly from the described model. For this purpose, the extended unit cell is considered. Assuming the same symmetry for Al_s and O_i layer (which cannot be imaged), the extended unit cell has the formula $\text{Al}_{19}\text{O}_{28}\text{Al}_{28}\text{O}_{32}$. Compared to the unit cell of the unperturbed alumina film, the structure is oxygen deficient. This induces electronic defect states which are discussed in detail in section 3.3.2.

Zigzagged APDB

An oxygen deficiency also prevails in zigzagged APDB (type IIA and IIB), resulting in a similar electronic structure. This can be deduced from STM experiments, that are not discussed here in detail. Instead, we will focus on structural features which differ from those of straight APDB and which are responsible for the zigzagged shape.

Fig. 3.4 (a-b) displays an atomically resolved STM image of the Al_s layer containing a zigzagged APDB (type IIA). The latter can be easily distinguished because of the apparent corrugation of this layer: as described in section 3.2, Al_s atoms in pyramidal

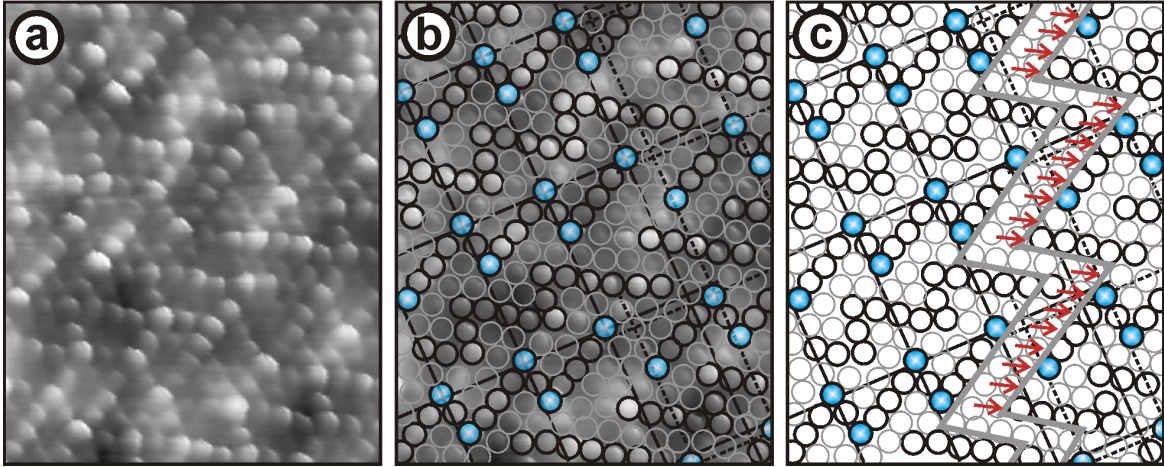


Figure 3.4: Structure of zigzagged APDB (type IIA) in the Al_s layer [133]. The atomically resolved STM image ($45 \text{ \AA} \times 56 \text{ \AA}$) was recorded at $V_s = 0.5 \text{ V}$ and $I_t = 1 \text{ nA}$. The unit cell on either side of the APDB can be easily determined, because Al_s atoms appear with different size dependent on their coordination. This is marked by black and gray circles, reflecting pyramidally and tetrahedrally coordinated Al_s , respectively. Atoms with strongly distorted pyramidal coordination are indicated with blue filled circles. The resulting model is shown in (c). Zigzagged APDB result from the insertion of an aluminum row oriented 60° to the long alumina unit cell vector, which jumps to the 4th next row every eight atoms [133].

interstices (black circles) appear to protrude more than tetrahedrally coordinated Al_s atoms (gray circles). Furthermore, Al_s atoms with strongly distorted pyramidal coordination have the most pronounced height and are marked with blue circles. These atoms are not distributed symmetrically within the unit cell and can therefore be used to determine size and orientation of the latter. The model obtained from the STM image is depicted in Fig. 3.4 (c). Red arrows mark additional Al_s atoms in the APDB. They are inserted in an angle of 60° with respect to the long alumina unit cell vector. In contrast to straight APDB, not a continuous but a broken row of Al_s atoms is inserted: every eight atoms, the inserted line jumps to the 4th next aluminum row. Oxygen deficiency, responsible for the induction of electronic defect states, is only inherent to sections where a continuous row of (eight) Al_s atoms is inserted. Thus, zigzagged APDB are better described as a series of more localized defects, which explains their particular shape. Consequently, the microscopic direction of zigzagged APDB differs from its macroscopic orientation, which is well aligned to the diagonal of the alumina unit cell.

Burgers Vectors

Each line defect is characterized by its displacement vector, the so-called Burgers vector, \mathbf{v}_B . The analysis of its magnitude and direction gives important information on

the strain which induces the line defect. Fig. 3.5 displays \mathbf{v}_B for all types of APDB with respect to the lattice of the NiAl(110) substrate. As deduced from STM images, the magnitude $|\mathbf{v}_B| \approx 3.0 \text{ \AA}$ is identical for both zigzagged and straight APDB. Also their orientation with respect to the NiAl $[\bar{1}\bar{1}0]$ direction is similar: the Burgers vectors of straight and zigzagged APDB are inclined to that direction by $\pm 24^\circ$ and $\pm 36^\circ$, respectively.

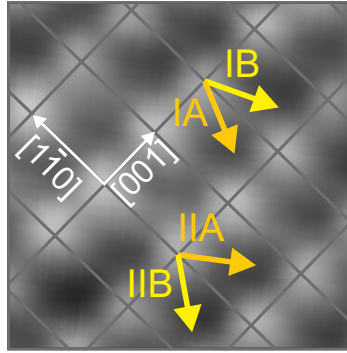


Figure 3.5: Burgers vectors, \mathbf{v}_B , of APDB (cf. Fig. 3.1) with respect to the NiAl substrate. The NiAl lattice and the Burgers vectors are superposed upon an STM image. The length of the vectors was determined from STM images in different layers of the alumina film and is $\sim 3.0 \text{ \AA}$.

Considering O_i and Al_s layer, the Burgers vectors of APDB are oriented along characteristic directions of their quasi-hexagonal lattices. Interestingly, only two of the three possible orientations are observed. The “missing” orientation would result in APDB orientated parallel to the $[\bar{1}\bar{1}0]$ direction of the NiAl(110); atom insertion would here occur perpendicular to that direction. However, such dislocation does not seem to be efficient to reduce the strain in the alumina lattice. The direction of maximum strain can therefore be assumed to run along the $[\bar{1}\bar{1}0]$ direction, which is also the direction of commensurate growth. It can be supposed that the strain is compressive because (i) the extended alumina unit cell of APDB bridges one more Ni row than the unperturbed unit cell and (ii) the contributions of the different Burgers vectors along the NiAl $[\bar{1}\bar{1}0]$ direction are shorter than the NiAl unit cell. For zigzagged APDB, this contribution is $3.0 \text{ \AA} \cdot \cos 36^\circ = 2.4 \text{ \AA}$, for straight APDB it amounts to $3.0 \text{ \AA} \cdot \cos 24^\circ = 2.7 \text{ \AA}$. The extra space of $4.1 \text{ \AA} - 2.7 \text{ \AA} = 1.4 \text{ \AA}$ and $4.1 \text{ \AA} - 2.4 \text{ \AA} = 1.7 \text{ \AA}$, respectively, allows the film to reduce its compressive strain.

3.3.2 Electronic Structure

The structural analysis presented in the previous sections revealed the same film thickness for unperturbed alumina areas and APDB. Nevertheless, the apparent height of APDB shows distinct variations as a function of V_s in STM images recorded in constant

current mode (Fig. 3.6 a) [92, 126]. This clearly indicates the induction of electronic defect states by APDB. A detailed description of these states is of great interest since it allows to correlate structural and electronic properties. STM represents a perfectly suited tool for the local investigation of not only the geometric but also the electronic structure of a sample. Here, it was operated in three different modes: constant current imaging, conductance (dI/dV) imaging and STS. The results are compared to simulations based on the structural model developed in Section 3.3.1, whereby the calculations were accomplished by M. Shishkin and G. Kresse [136]. Again, the focus will be on straight APDB. Zigzagged APDB exhibit similar electronic structure. However, they are less regular. Therefore, only main differences are briefly presented in the end of this section.

Straight APDB – Experimental Results

Constant current images of APDB have been recorded in the range between -4.0 V and 6.0 V. The results for $V_s > 0$ are summarized in Fig. 3.6 (a). At negative and small positive V_s (-4.0 V to 1.0 V), the height contrast to surrounding unperturbed oxide areas is negligible, and line defects are almost invisible in the STM. In images taken around zero bias, APDB are only identified by the deviating atom positions compared to their arrangement in regular oxide unit cells (cf. Fig. 3.3). Above 1.5 V, APDB appear as bright lines in constant current images. Their apparent height gradually increases with increasing V_s and peaks at approximately 2.5 V. The application of higher positive V_s slightly reduces the topographic contrast. However, the one-dimensional defects are imaged as protruding lines for voltages as high as 6.0 V. The bias-dependent corrugation of line defects is summarized in Fig. 3.7. Contrast variations between APDB and regular oxide patches are accompanied by changes in the geometric pattern observed on the oxide surface. In the range between 1.5 V and 3.0 V, APDB are imaged as single white lines. They become double strands with a groove-like depression in the center between 3.5 V and 4.0 V and narrow down to a single line in images taken above 4.5 V.

Whereas constant current images average over the LDOS between tip and sample Fermi level, differential conductance (dI/dV) measurements exclusively probe states with an energy close to the applied bias voltage. The dI/dV signal gives therefore a much better evaluation of the LDOS of the sample surface. Figure 3.6 (b) shows conductance images of APDB, simultaneously measured with the constant current images from Fig. 3.6 (a). In agreement with STM constant current images, dI/dV images of APDB show little contrast with respect to regular oxide patches at negative and small positive V_s . For $V_s > 1.5$ V, the dI/dV signal on line defects strongly increases and passes through a pronounced maximum at 2.5 V. The dI/dV peak reproduces the maximum in apparent height, but shows a much smaller width due to the better energy

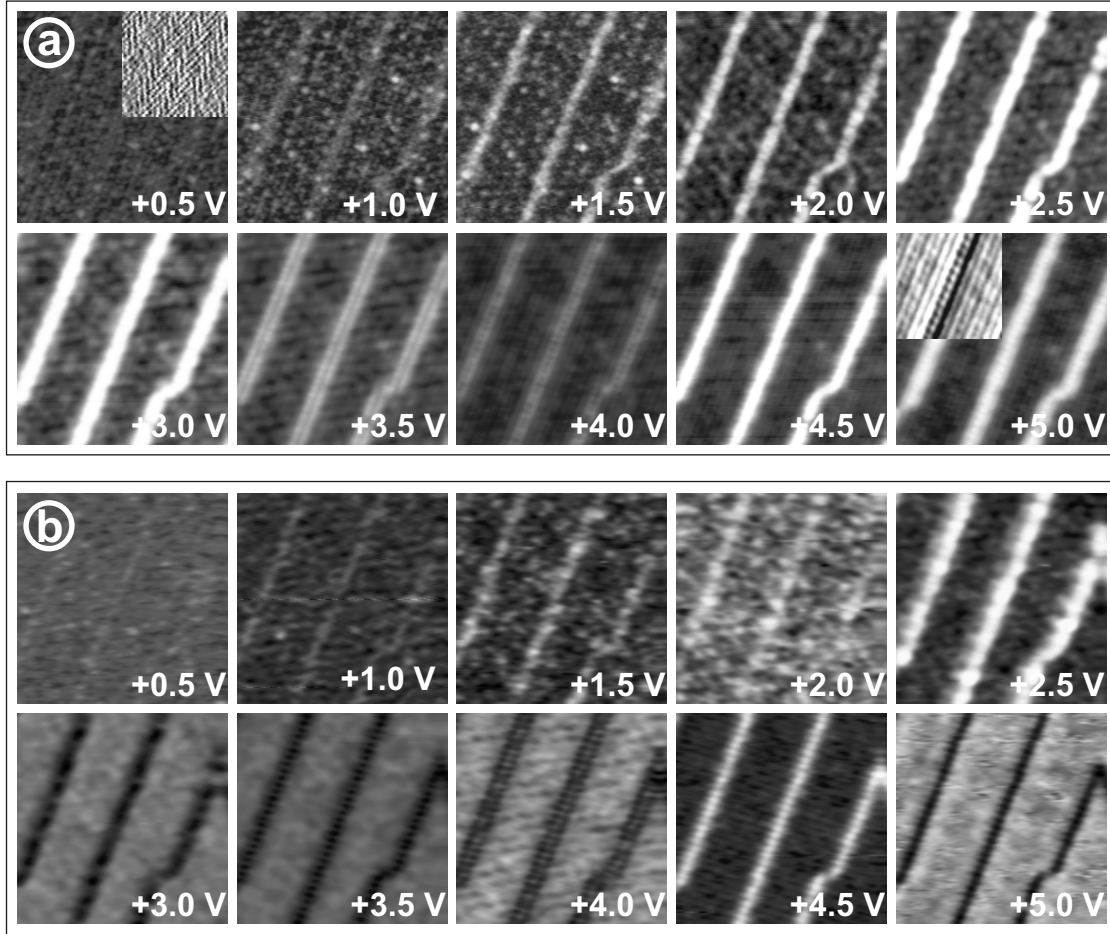


Figure 3.6: (a) STM images of straight antiphase domain boundaries in an alumina film on NiAl(110), recorded in constant current mode at the indicated sample bias (image sizes $300 \text{ \AA} \times 300 \text{ \AA}$, $I_t = 0.1 \text{ nA}$). Differentiated and contrast-enhanced sections of two images are shown in the insets. (b) Conductance (dI/dV) images of the same area ($V_{mod} = 20 \text{ mV}$, $f_{mod} = 580 \text{ Hz}$).

resolution of the differential measurement (Fig. 3.7). Above 2.5 V, the dI/dV intensity of line defects attenuates and drops below the value of regular oxide domains. As a result, APDB appear as depressions in dI/dV images taken around 3.5 V. A further conductance maximum was detected at 4.5 V, indicating a second unoccupied state induced by APDB. Also in dI/dV images, the observed defect pattern changes dependent on V_s , from a single line below 3.0 V to a double strand around 4.0 V and back to a single line at higher energy.

Supplementary information on the electronic structure of APDB in the alumina film was gained by dI/dV spectroscopy. Here, the tip is stabilized on a selected position and the bias-dependent dI/dV signal is measured with lock-in technique and disabled feedback loop. In contrast to dI/dV imaging, the tip height is constant during spectroscopy

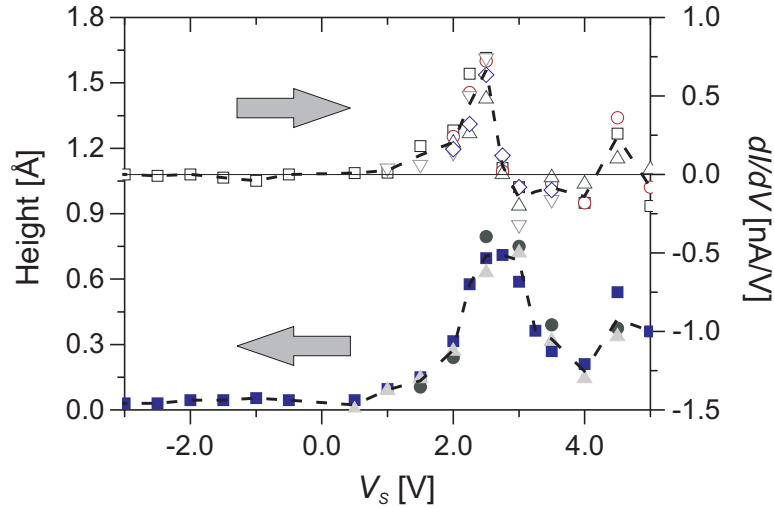


Figure 3.7: Bias dependence of apparent height and dI/dV intensity of APDB with respect to defect-free alumina domains on NiAl(110). The symbols show results from different experimental runs, the broken lines represent the best fit through the data points. The two maxima indicate defect states induced by the APDB.

and the conductance is not influenced by a varying tip-sample separation. Figure 3.8 (a) shows two dI/dV spectra of an APDB in comparison to a spectrum taken above a regular oxide region. In distance to the line defect, the conductance steadily rises with applied sample bias. The slope increase in the dI/dV curve around 3.1 V marks the onset of the alumina conduction band (CB). For tip positions above an APDB, a pronounced dI/dV peak around 2.6 V appears in the spectra, flanked by a smaller maximum at 3.0 V. At higher voltages, the dI/dV intensity falls behind the value measured away from the line defect, which causes the negative contrast of APDB in the respective dI/dV images. The 4.5 V peak observed by dI/dV imaging could not be detected in the spectroscopic mode, because it is covered by the sharply increasing conductance above 3.1 V. A series of 70 dI/dV spectra taken across a line defect clearly demonstrates the development of defect states in vicinity of APDB (Fig.3.8 b).

The investigations of the local electronic properties of the thin alumina film consistently show the presence of gap states induced by APDB. Two pronounced states at 2.5 V and 4.5 V are identified by topographic and dI/dV imaging. An additional shoulder in the LDOS at 3.0 V shows up only in dI/dV spectroscopy due to its better energy resolution. The observed level energies are influenced by the tip-induced electric field, which bends the oxide bands dependent on the actual tip-sample distance. Due to the high dielectric constant of alumina and the small thickness of the oxide film, the level shifts are supposed to be small. The detected defect levels are generally unoccupied. Taking the kink at 3.1 V in dI/dV spectra of the regular oxide as a fingerprint of the

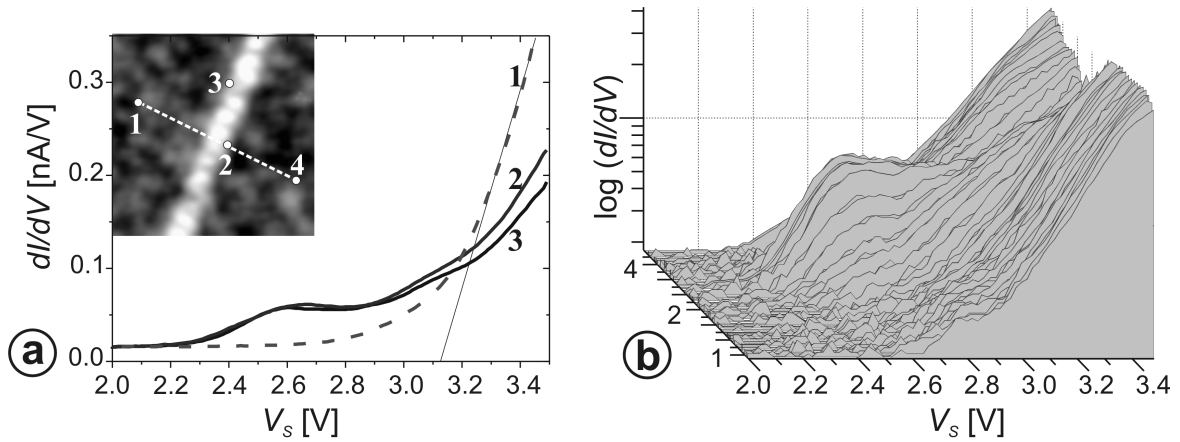


Figure 3.8: (a) Conductance spectra taken on a straight APDB and on a regular region of the alumina film on NiAl(110). The solid line interpolates the onset of the alumina conduction band. (b) Series of 70 dI/dV spectra taken across an APDB. The corresponding tip positions are marked in the inset of Fig. 3.8 (a). To emphasize the additional dI/dV peaks at the line defect, a logarithmic scale is used in the diagram. The gap was set with $V_s = 3.0$ V and $I_t = 0.1$ nA in both cases.

CB edge, the 2.5 V defect state clearly lays inside the alumina band gap. The higher levels are close to or already above the CB edge. From bias-dependent changes in the geometric pattern of APDB, the spatial localization of defect states can be derived. The level at 2.5 V shows up as a single line in STM images and is therefore relatively localized along the dislocation line. In the energy region of the higher levels, a double line is imaged in constant current and dI/dV mode, separated by a region of reduced LDOS. This observation indicates a rather delocalized nature of the higher gap states around the actual topographic defect.

Straight APDB – Comparison with Theory

In order to interpret the experimental results, they are compared to recent theoretical studies accomplished by M. Shishkin and G. Kresse [136]. The methods have been briefly presented in Section 3.3.1. Based on the structural model derived from STM images, the partial density of states (PDOS) was calculated for Al_s and O_s layer in the unperturbed alumina film and in APDB. The results are shown in Fig. 3.9. According to these, the perfect oxide film exhibits a band gap of ~ 6.4 eV, whereby the Fermi level is pinned in the midpoint between CB and valence band (VB) edges. The calculated band gap is smaller than the experimentally determined one, which amounts to 7–8 eV [24, 25]. However, it is a well-known problem related to DFT calculations that the obtained band gaps are too small. Considering this point, experiment and theory agree quite well. The onset of the VB was calculated to be at ~ 2.9 eV, which is only slightly below the value of 3.1 eV, obtained by STS measurements (cf. Fig. 3.8).

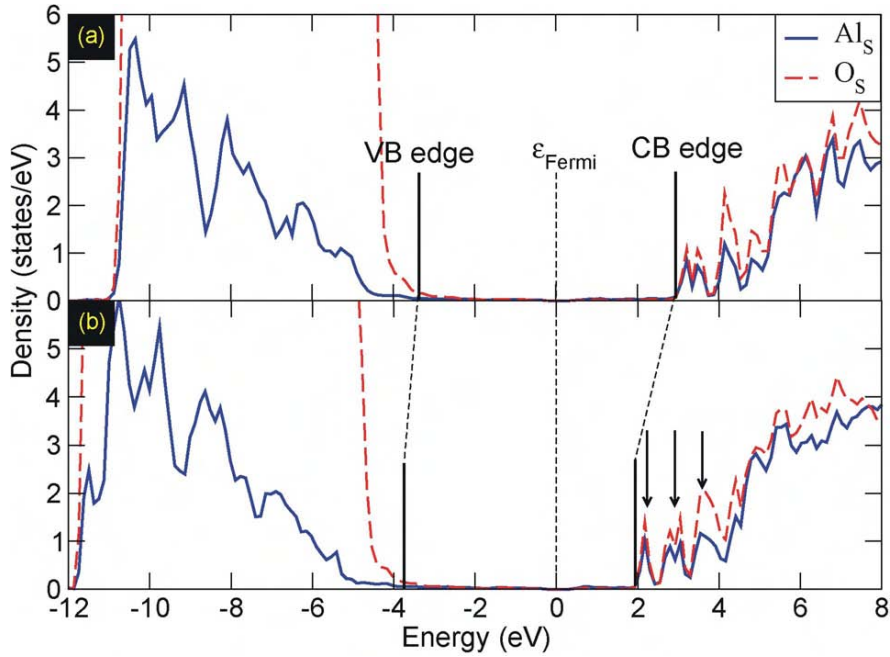


Figure 3.9: Partial density of states (PDOS) of (a) the perfect oxide and (b) the APDB, calculated by M. Shishkin and G. Kresse [136] using a hybrid functional. Three peaks are highlighted by the vertical arrows, and the conduction band (CB) and valence band (VB) edges are marked. The DOS are aligned at the Fermi level.

Furthermore, calculations show that APDB induce three unoccupied defect states at 2.3 eV, 2.9 eV and 3.9 eV. Two of them (at 2.3 eV and 2.9 eV) are located below the CB edge, the third one lies in the CB. Taking into account that the energies of both the VB onset and the defect states are probably shifted toward the Fermi level due to the computational method, these results agree very well with the experimental findings. Thus, the structural model appears to be correct.

Usually, an oxygen vacancy implies that two electrons occupy electronic defect states (color or F-centers) with Al 3*p* character close to the CB edge [136, 146]. However, both experimental and theoretical results contradict the common picture, since all defect states induced by APDB are unoccupied. This can be explained by the transfer of two electrons to the NiAl substrate, as described by the formula $(\text{NiAl})^{2-}(\text{Al}_{19}\text{O}_{28}\text{Al}_{28}\text{O}_{32})^{2+}$. To counterbalance the electron transfer and in agreement with the formal charges, a band bending occurs around the defect, causing a local downward shift of VB and CB by ~ 0.5 eV. This pushes the defect levels above the Fermi level and causes their unoccupied nature.

Symmetry and lateral extent of APDB could be theoretically studied only for the first defect state at 2.3 eV, because of the limited size of the supercell. According to these studies, the state is mainly localized close to the position where O_s atoms have

large separations, i.e. between the two Al_s atoms close to the red circle shown in Fig. 3.3 (f). Apparently, the oxygen deficiency is mainly localized in proximity to this position. LDOS simulations of APDB at 2.3 eV show a single protruding line along the short alumina unit cell vector and agree very well with STM data. However, it is important to note that the building principle of the perfect film is maintained at the position with increased $\text{O}_s\text{-O}_s$ distance. Thus, this oxygen-deficient structure differs significantly from “classical” O vacancies in other oxides, such as MgO.

Zigzagged APDB

Zigzagged APDB exhibit similar unoccupied defect states as straight APDB. However, while the defect levels in straight APDB are delocalized along a line, they are restricted to distinct areas in zigzagged APDB. This is shown in the constant current (a-c) and

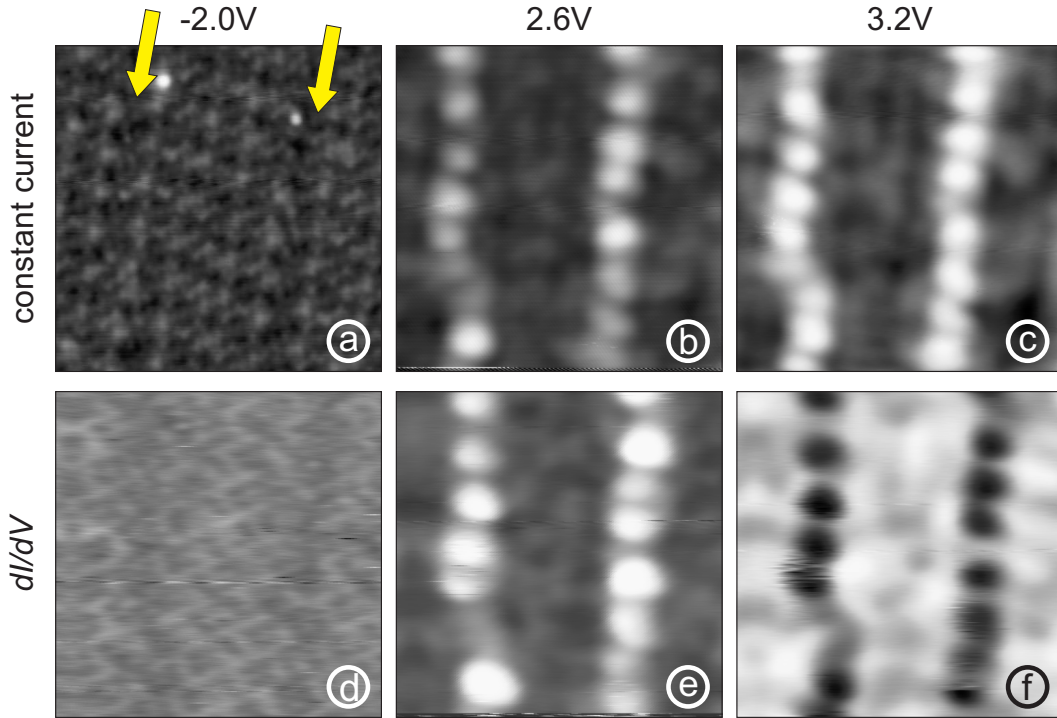


Figure 3.10: Constant current (a-c) and conductance (d-f) images of the alumina film on NiAl(110), containing two zigzagged APDB ($172 \text{ \AA} \times 172 \text{ \AA}$, $I_t = 1 \text{ nA}$). The same area is imaged at different sample bias, indicated on top.

conductance (d-f) images of Fig. 3.10. These images show the same area of the alumina film on NiAl(110) at different sample bias. The appearance of the two zigzagged APDB changes dependent on V_s . At $V_s < 0$, the line defects can hardly be distinguished from the surrounding oxide. At $V_s = 2.6 \text{ V}$, APDB appear as protrusions in both constant current and dI/dV image. This clearly indicates that zigzagged APDB induce a defect

state with similar energy as straight APDB. These defect states are located at round spots with an extension of $20 \text{ \AA} - 24 \text{ \AA}$, which are separated from each other. This extension just reflects the geometric structure described in Section 3.3.1. Accordingly, the defect levels are present only in those regions, where a continuous row of 8 Al_s atoms (spatial extension: $8 \times 3.0 \text{ \AA} = 24 \text{ \AA}$) is inserted. Almost the same symmetry is observed at $V_s = 3.2 \text{ V}$, where zigzagged APDB appear as spots with increased apparent height in constant current images and with reduced conductance in dI/dV images. Again, this behavior is similar to straight APDB, demonstrating the resemblance concerning the electronic properties. The images in Fig. 3.10 show also that zigzagged APDB are not as regular as straight APDB. Deviations in the structure, which are probably determined by the growth of the alumina film, result in deviating electronic properties. Thus, the regions ($\sim 20 \text{ \AA}$ large spots) of increased or reduced conductance, respectively, have not exactly the same extension and intensity in every case. Because of these irregularities, zigzagged APDB are not discussed here in more detail. Their main properties have been presented, notably the resemblance to straight APDB concerning the energy of the induced electronic states. The different localization could be explained with the deviating structure.

3.4 Summary

This chapter provides a detailed structural characterization of the thin alumina film on NiAl(110) and of regularly appearing line defects in this film. STM was used to obtain atomically resolved images of three out of four oxide layers. However, the assignment to distinct alumina layers was possible only after theoretical investigations by Kresse *et al.* [1]. The structure varies from former proposals and does not correspond to a known alumina bulk phase. The accessibility of different alumina layers by STM allowed the structure determination of antiphase domain boundaries (APDB). They represent oxygen deficient line defects which induce three unoccupied electronic states in the oxide film. Occupied defect states are not observed, though they commonly result from oxygen vacancies. This surprising result is explained by a transfer of two electrons from the alumina film to the NiAl substrate, involving a band bending toward the positively charged defect.

Chapter 4

Single Gold Atoms on the Alumina Film

This chapter treats the adsorption properties of a thin alumina film on NiAl(110) toward single metal atoms. Initial studies were performed on Ag atoms. However, their investigation proved to be difficult because of their weak interaction with the alumina film. Therefore, these attempts were abandoned and Au adatoms were investigated instead. For that purpose, Au was evaporated onto the oxide film at low temperature. The resulting Au species (monomers and small clusters) were investigated by STM, STS and conductance imaging. Surprisingly, some of the Au adatoms assembled into one-dimensional clusters. The analysis of their geometric properties (length, orientation etc.) provides important information on the Au-substrate interaction. Further studies by STS and conductance imaging allow to determine the electronic structure of the Au species, which can be used as a fingerprint for the Au-substrate and the Au-Au interaction. Finally, the results obtained for Au atoms are briefly compared with Ag to estimate the influence of the chemical nature of the adatom on the interaction with alumina film.

4.1 Introduction

The interaction between oxide surfaces and metal deposits plays an important role in several technologically relevant fields, such as microelectronics and heterogeneous catalysis. Central questions concern the adsorption of atoms, their diffusion and nucleation on the oxide surface. While there are remarkable advances in the investigation of single metal atoms on metal surfaces [147–150], the knowledge for metal-oxide systems is still sparse. This is, to some extent, owed to experimental difficulties related with oxides, especially their insulating nature. These problems can be circumvented

when investigating thin oxide films, such as the alumina film on NiAl(110) described in Chapter 3 [20, 21, 151]. Commonly, it is accepted that these oxide films reflect the properties of bulk oxides, and many examples show that this is often justified. According to a recent theoretical work, however, a generalization of this assumption to all metal/oxide-film systems has to be doubted [50]. The authors compare the adsorption of Au atoms on bulk MgO with that on MgO films on Mo(100). While Au atoms are found to be neutral on bulk MgO, they appear to be negatively charged on thin MgO films. The effect is ascribed to electron tunneling from the underlying metal substrate [50, 152], induced by the high electron affinity (EA) of Au (2.31 eV). This theoretical work suggests that careful analysis is necessary to evaluate the suitability of thin films as model support. In general, there is a big discrepancy between the number of computational and experimental results: while numerous theoretical studies investigate the interaction of oxides and oxide films with metal adatoms [153–155], only a few experimental papers are dedicated to this question [116, 156, 157]. Most notably, an experimental evidence for deviating properties of wide-gap thin insulating films from bulk oxide has not been reported, yet.

4.2 Preliminary Studies on Silver

Silver atoms were deposited onto the surface using the micro-evaporator described in Section 2.5.4. During this procedure, the sample warmed up from 5 K to 8 K. After reaching the initial temperature, the such prepared surface was studied by STM. Figure 4.1 (a) shows an STM image of Ag atoms deposited onto an incompletely oxidized NiAl(110) sample, i.e. this surface contains areas of pristine NiAl as well as areas with the perfectly ordered alumina film described in the previous chapter. At the chosen sample bias, APDB in the oxide film appear as bright stripes in the STM image, allowing to identify the oxide patches. Almost no Ag atoms are observed in these regions, in contrast to metallic surface areas. This suggests that (i) Ag atoms can move on the surface after evaporation and prior to thermalization and that (ii) they have a higher sticking coefficient on the NiAl surface. The NiAl patches act hence as a trap for the Ag adatoms, reducing the occupation of the oxide surface.

To study Ag atoms on the alumina film, a fully oxidized NiAl(110) sample was therefore used. Such a surface is shown in Fig. 4.1 (b) after evaporation of Ag. All Ag adsorbates appear with round shape and diameters of $\sim 10 \text{ \AA}$ at small sample bias. Larger particles are not observed at that coverage, indicating that these adsorbates are single Ag adatoms. The latter become more and more unstable with increasing absolute bias, and above 2 V, most of them desorb, both during the scan process and during spectra acquisition. Even if V_s is chosen close to the Fermi level, Ag atoms

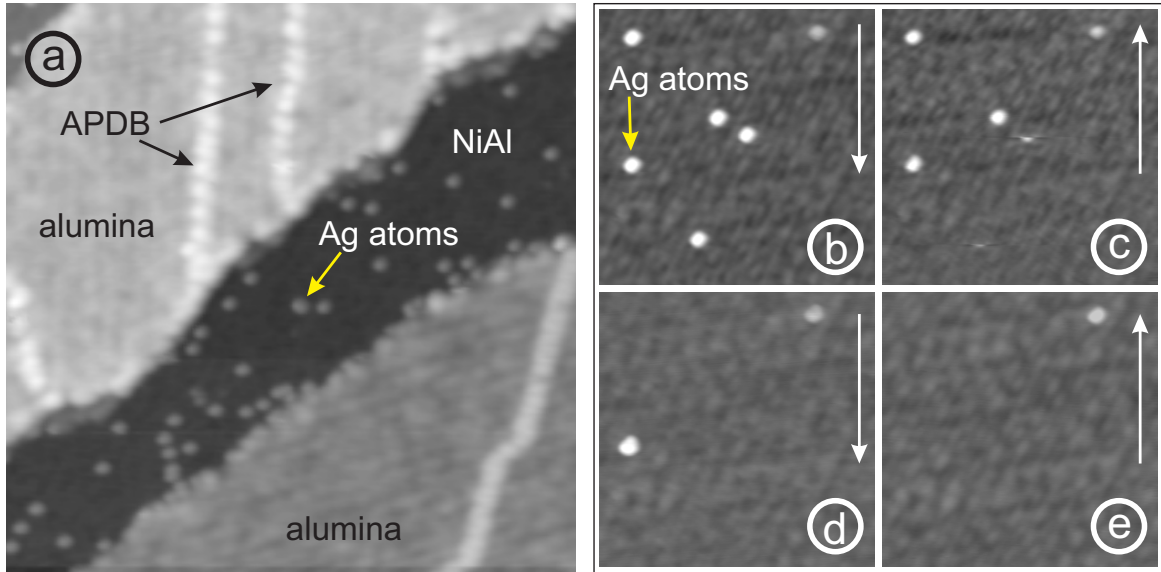


Figure 4.1: (a) STM image ($616 \text{ \AA} \times 616 \text{ \AA}$, $V_s = 3.0 \text{ V}$, $I_t = 1 \text{ nA}$) of a partially oxidized NiAl(110) sample after deposition of Ag atoms at $\sim 8 \text{ K}$. The alumina patches are well-ordered and have the same structure as described in Chapter 3. (b-e) STM images ($258 \text{ \AA} \times 258 \text{ \AA}$, $V_s = -0.5 \text{ V}$, $I_t = 0.5 \text{ nA}$) of Ag atoms on the thin alumina film, i.e. on a fully oxidized NiAl(110) sample. The series of constant current images demonstrates that Ag atoms are easily desorbed during the scan process. The white arrows indicate the y -direction of the tip movement.

desorb easily as shown in the image series in Fig. 4.1 (b-e). Smaller tunneling currents reduce this problem. However, preliminary STS studies showed that electronic states induced by Ag adatoms are often beyond the achievable spectral range, given by the Ag desorption energy. These observations show that Ag is bound to the alumina film only weakly. Therefore, Ag is not a good candidate to study the adsorption behavior of the alumina film toward metal adatoms. It will be especially difficult to investigate the influence of the adsorption site on the electronic properties of the adatoms. Thus, Ag was not further studied, and Au was used instead. The reason for the weak interaction between Ag and the alumina film will be discussed later in this chapter.

4.3 Gold Species and Their Geometric Properties

4.3.1 Deposition of Gold Atoms

Gold was evaporated onto the surface at a sample temperature of $\sim 10 \text{ K}$ using the micro-evaporator described in Section 2.5.4. Due to their initial thermal energy, Au atoms can move on the surface prior to thermalization. This can be referred from Fig. 4.2 (a), which shows an STM image of a partially oxidized NiAl(110) sample after

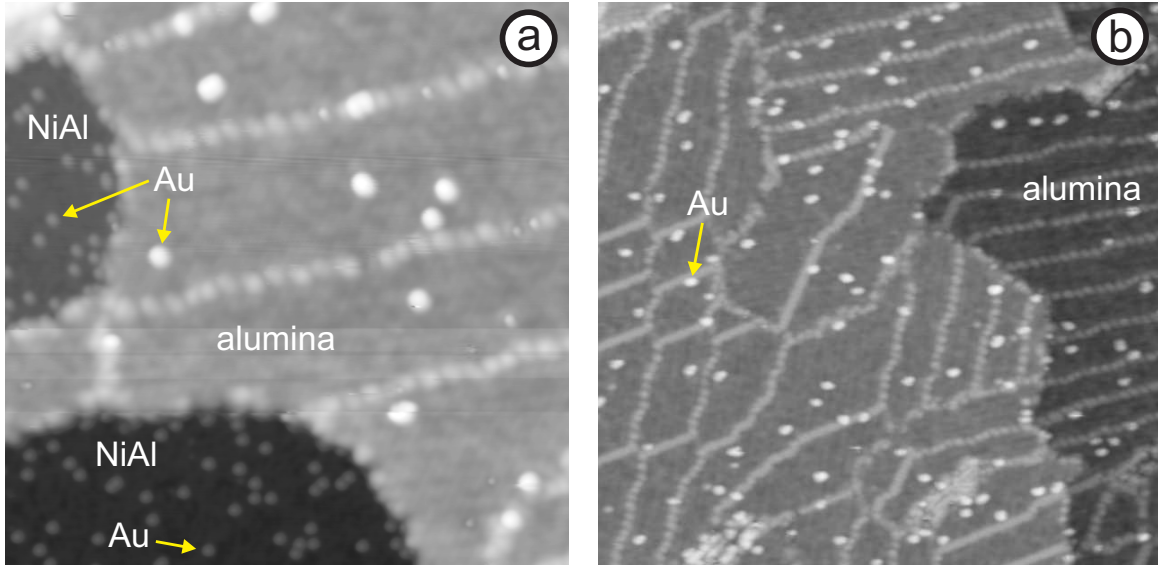


Figure 4.2: (a) STM image ($559 \text{ \AA} \times 559 \text{ \AA}$, $V_s = 3.0 \text{ V}$, $I_t = 0.5 \text{ nA}$) of a partially oxidized NiAl(110) sample after deposition of Au atoms at $\sim 10 \text{ K}$. (b) STM image ($1290 \text{ \AA} \times 1290 \text{ \AA}$, $V_s = 3.0 \text{ V}$, $I_t = 0.5 \text{ nA}$) of Au atoms on a fully oxidized NiAl(110) sample. The shown coverage of Au on the alumina film is representative for all studies within the scope of this work.

deposition of Au atoms. The number of Au atoms on the NiAl patches is much higher than on the alumina film. Thus, Au atoms move on the surface and bind preferentially to NiAl because of the increased sticking coefficient and the better heat dissipation of Au on the metal surface. However, much more Au atoms stay on the oxide surface in comparison to Ag, indicating a stronger interaction with the alumina film. Further investigations on Au atoms were performed on a fully oxidized NiAl(110) sample. A typical coverage ($\sim 0.0005 \text{ ML}$) used for the present studies is shown in the STM image in Figure 4.2(b). Apart from the coverage, this STM image reveals the distribution of Au atoms with respect to line defects of the alumina film, which appear as bright lines at the indicated sample bias. Apparently, Au does not exhibit a preference for adsorption sites on these defects, in contrast to Pd [115].

4.3.2 Gold Species on the Surface

The fact that Au atoms can initially move on the surface leads to the formation of dimers (D) and small clusters (C) beside monomers (M). This is shown in Fig. 4.3. While Au aggregates are imaged with large apparent diameter at positive sample bias V_s (Fig. 4.3 a), they appear much smaller at negative V_s (Fig. 4.3 b), which often allows the determination of their internal structure. The majority are Au dimers (D) with different orientations, but also small clusters are observed. Surprisingly, many of these

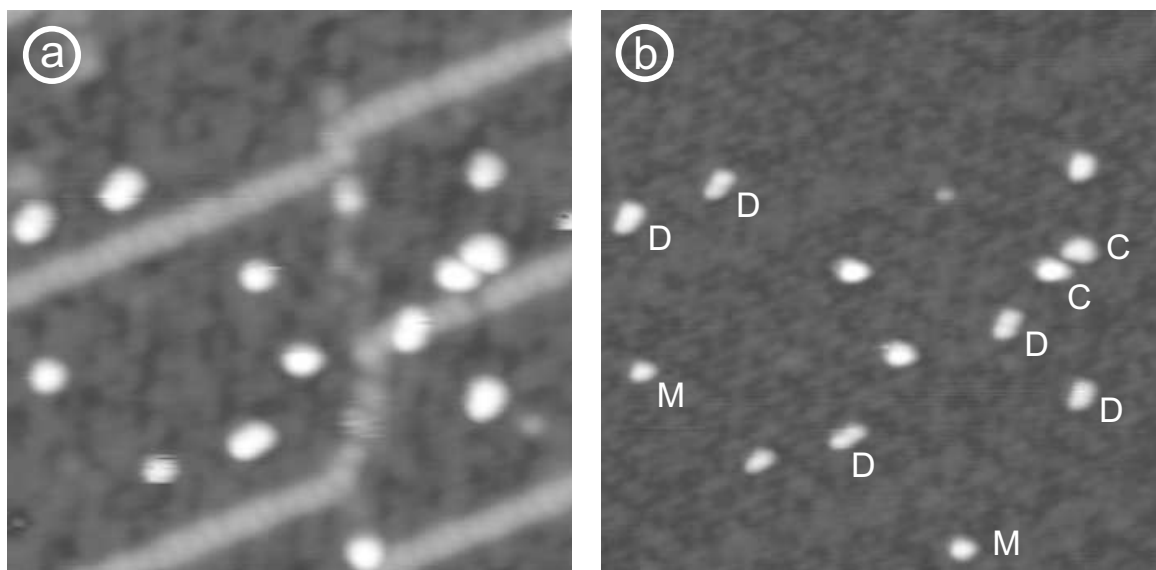


Figure 4.3: STM images of Au atoms on the thin alumina film ($559 \text{ \AA} \times 559 \text{ \AA}$, $I_t = 0.5 \text{ nA}$). The images are recorded at sample biases of 3.0 V (a) and -1.0 V (b), respectively, and show the same surface area. The internal structure of the Au particles is better resolved in (b), where Au monomers (M) can be distinguished from dimers (D) and small clusters (C). The changes in imaging properties as a function of bias indicate a rather inhomogeneous LDOS of the Au aggregates.

clusters are one-dimensional (1D) chains at low coverage.

Fig. 4.4 shows STM images of a Au monomer and such self-assembled Au chains with a maximum length of 22.5 \AA . Longer chains have not been observed. The images are recorded at negative V_s , whereby V_s is chosen well above (top) and close to (bottom) the highest occupied state of the Au chains. In the images on top, the chains appear with a uniform height of $\sim 4 \text{ \AA}$. The imaging properties change dramatically in the case of resonant tunneling into the electronic states of the chain (bottom). The apparent height of the chains is then increased by $1 - 2 \text{ \AA}$. Furthermore, the chains show a distinct substructure, consisting of $3 - 5$ lobes. As can be referred from the height profiles in Fig. 4.4, these lobes are separated by $5.6 - 6.0 \text{ \AA}$, which corresponds to the double Al-Al distance in the surface aluminum (Al_s) layer of the thin oxide film [1]. We suggest that each lobe reflects the position of a Au atom or a Au-induced electronic state, because no intermediate chain lengths have been observed. Thus, the observed chains in Fig. 4.4 would correspond to dimers, trimers, tetramers and pentamers of Au adatoms. This interpretation implies an untypical Au-Au distance, which would be about twice as large as in bulk gold (2.9 \AA) or in gas phase dimers (2.5 \AA) [158].

The hypothesis of large Au-Au separations in dimers and chains is supported by the STM images in Fig. 4.5. Two lobes can be distinguished for the Au aggregate in Fig. 4.5 (a). This indicates that this Au particle is a dimer, which is imaged at a

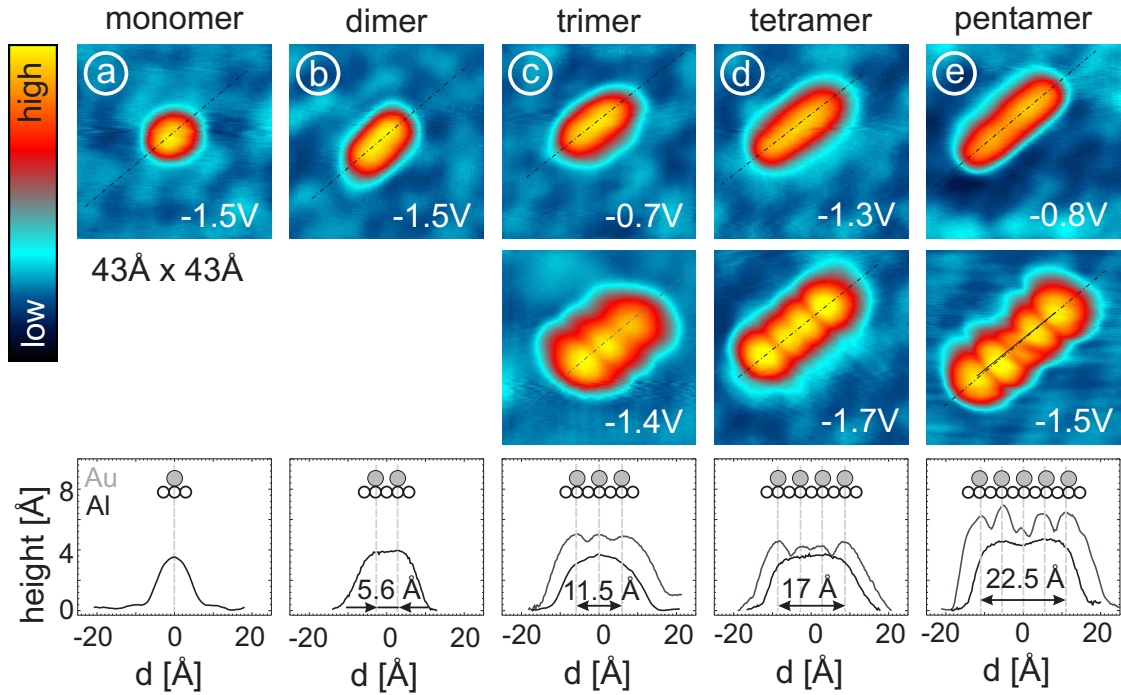


Figure 4.4: STM images of a Au monomer (a) and self-assembled Au chains containing two to five atoms (b–e) on alumina / NiAl(110). The STM images are recorded at negative sample bias V_s , whereby V_s is chosen either well above (top) or close to (bottom) the highest occupied state of the Au chain. The atom positions within the chains are resolved only in the case of resonant tunneling. Line scans along the chain axis reveal a distance of 5.6 – 6.0 Å between two adjacent Au atoms.

sample bias close to a resonance level and therefore appears big. The distance between the lobes is 5.8 Å and agrees well with the separation between adjacent lobes in Au chains determined from Fig. 4.4. During further image acquisition, the structure of the Au aggregate changed such that only one atom remained at the former position of the upper lobe. This suggests that the Au aggregate consisted initially indeed of two atoms, and that each lobe reflects the position of a Au atom.

4.3.3 Adsorption Site

A very important point to understand the interaction between Au and the alumina film concerns the adsorption site. So far, it was found that the distance between two lobes (and thus Au atoms) agrees well with twice the separation of neighboring Al_s atoms, indicating that the Al_s lattice plays an important role for the Au adsorption. Further information concerning the adsorption site of Au atoms can be obtained from supercorrugated STM images.

Figures 4.6 (a-c) show the same Au trimer, once imaged with a metallic tip (c) and once with a tip modified by an adsorbate, leading to supercorrugation and atomic reso-

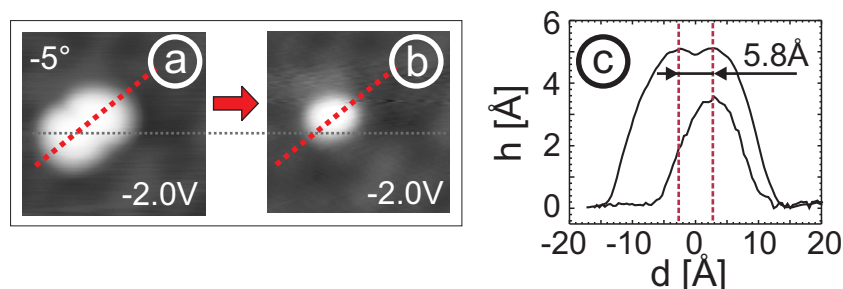


Figure 4.5: (a) STM image of a Au dimer ($47 \text{ \AA} \times 47 \text{ \AA}$, $I_t = 0.5 \text{ nA}$). One Au atom is desorbed during the scan process. The remaining Au atom is shown in (b). (c) Cuts along the dotted lines in (a) and (b). The height difference between monomer and dimer indicates that the sample bias is close to a dimer resonance but well above the resonance of the monomer.

lution (a-b). The atomically resolved lattice corresponds to the Al_s lattice, as deduced from its quasi-hexagonal symmetry and the number of atoms (24) per unit cell [1, 133]. The image clearly reveals the alignment of Au chain and Al_s rows. Furthermore, the atom positions of the Al_s lattice can be extrapolated to the area underneath the Au trimer to identify the Au adsorption sites. The middle atom of the trimer is located on top of an Al_s atom, while the end atoms appear to be adsorbed on Al_s bridge sites. However, the positions of the end atoms might be altered by a slip-stick motion of the adsorbate on the tip when scanning over the trimer, because Au–Au distances

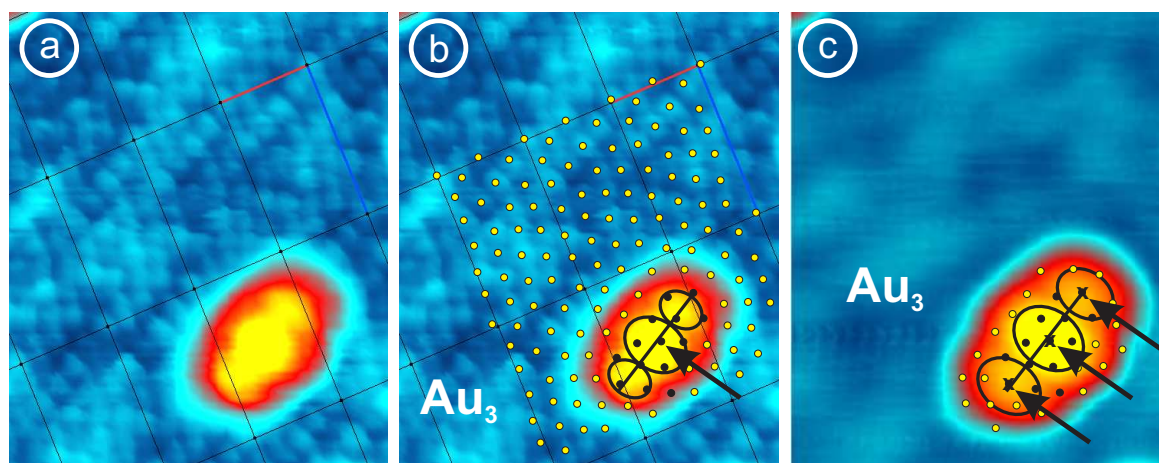


Figure 4.6: (a,b) STM image showing a Au trimer ($V_s = -0.7 \text{ V}$) and the Al_s layer with atomic resolution due to supercorrugation. In (b), the atom positions are marked, whereby the lattice is extrapolated to the area underneath the Au trimer. (c) STM image of the same region at $V_s = -1.2 \text{ V}$. The lattice from (b) is superposed. Image size (a-c): $42 \text{ \AA} \times 50 \text{ \AA}$, $I_t = 0.5 \text{ nA}$.

are considerably shorter than in normal images (cf. Fig. 4.6 (c) and Fig. 4.4). If the lattice is superposed onto the STM image without supercorrugation (Fig. 4.6 c), the adsorption site would be the same for all atoms of the trimer, i.e. on top of Al_s . This

finding contradicts the general intuition: metal adatoms are usually expected to bind on oxygen sites, which are more electrophilic. The adatom–substrate bond is then often associated with a (partial) charge transfer from the metal adatom to the oxygen [153]. The occupation of this site could thus be considered as continuation of the oxide lattice into the vacuum. The opposite observation here indicates a special interaction mechanism between Au adatoms and the alumina layer, possibly related to the high electron affinity of Au, which might disfavor oxygen sites. Calculations for Au atoms on α -Al₂O₃ predict almost equal adsorption energies for O and Al on-top sites with a small preference for O (0.03 eV) [159]. However, the situation can change dramatically for thin oxide films, as demonstrated recently for Au on MgO. While adsorption occurs preferentially on top of O for bulk MgO, cation sites are favorable on thin MgO films on Mo(100) [50]. A similar case might be present here.

4.3.4 Preferential Orientation of Gold Chains

A detailed analysis of the orientation of Au chains reveals that most of them are aligned close to the [001] direction of the NiAl substrate. Figure 4.7 shows statistics for dimers, which have been identified by their elongated shape and the characteristic pattern in conductance images (cf. Section 4.4). The diagrams display the angle between the long dimer axis and the [001] direction of NiAl, whereby the results are shown separately for either oxide domain, A and B. Both statistics reveal a clear maximum at +5° (A domain) and –5° (B domain), respectively. Thus, more than 40% of the dimers have the same, characteristic orientation. This effect is even more pronounced for trimers. Tetramers and pentamers, finally, were observed with no other alignment than $\pm 5^\circ$ with respect to the close-packed substrate rows on unperturbed terraces of the oxide film (Figs. 4.8 a,c).

This finding can be rationalized as follows. The Al_s layer of the oxide film forms a quasi-hexagonal lattice [1], whereby its orientation differs in domain A and B by an angle of $60^\circ - 48^\circ = 12^\circ$. This is visualized in Figs. 4.8 (b,d) for a perfectly hexagonal and thus simplified Al_s lattice (gray circles). The Au chains form along that vector of the Al_s lattice which is closest to the NiAl [001] direction. None of the two other directions of the quasi-hexagonal Al_s lattice was found to coincide with the direction of an adatom chain. The angle between chain axis and NiAl [001] direction is $\pm 6^\circ$ dependent on the domain, which agrees well with the experimentally determined value of $\pm 5^\circ$. The slight difference can be explained with the deviation of the Al_s lattice from the perfectly hexagonal arrangement (cf. Fig. 3.2 and [1]). The misalignment between chain axis and NiAl [001] direction also provides a plausible explanation for the limited chain length of 22.5 Å: Apparently, a favorable constellation between Al_s lattice and close-packed rows of NiAl exists only for some adsorption sites. Already 12 Å away

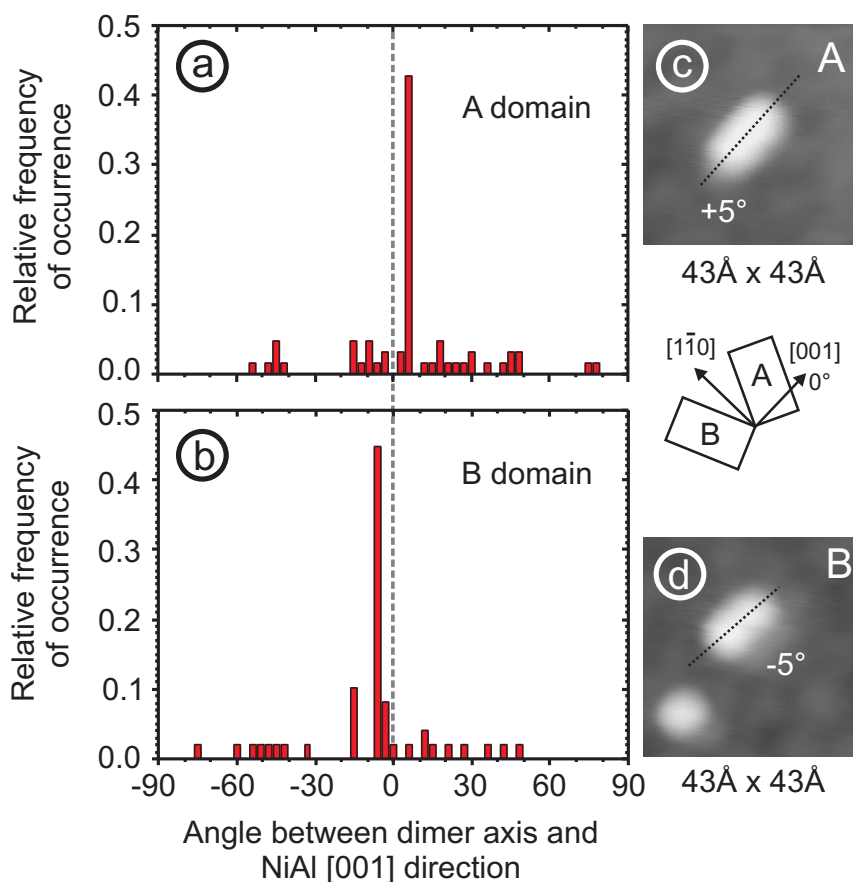


Figure 4.7: Statistical analysis of the orientation of Au dimers on the alumina film, whereby the angle between the long dimer axis and the NiAl [001] direction is investigated. The angular distribution is based on the analysis of 63 dimers in the A domain (a) and 49 dimers in the B domain (b) of the oxide. In either domain, the distribution shows a clear maximum around $+5^\circ$ (A) and -5° (B), respectively. (c-d) STM images of dimers with “typical” orientations. Tunneling conditions: $V_s = -0.5$ V, $I_t = 0.5$ nA (c) and $V_s = -1.5$ V, $I_t = 0.5$ nA (d).

from the optimum position, the divergence is ~ 1 Å, hampering the elongation of the chain. This is shown schematically in Figs. 4.8 (b,d).

The results described thus far indicate unambiguously the participation of the NiAl substrate in the binding of Au adatoms: Au chains form along the close-packed rows of NiAl, whereby the mean Au–Au distance is compatible with twice the Al_s – Al_s distance and twice the Ni–Ni / Al–Al separation in the metal support. Apparently, the most stable Au adsorption sites on the alumina film are the ones where Al_s atoms and atoms in Ni or Al rows have a distinct arrangement, for instance on top of each other. Such preferential adsorption sites are relatively rare and appear randomly on the surface because of the incommensurate growth and the tilted orientation of alumina on NiAl [24, 134].

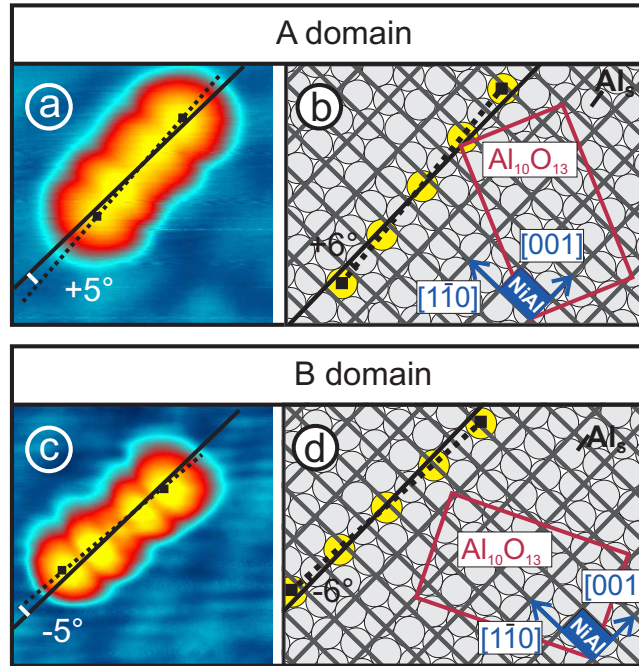


Figure 4.8: (a,c) STM images (size: $47 \text{ \AA} \times 47 \text{ \AA}$, $V_s = -1.8 \text{ V}$) of typical Au pentamers on alumina/NiAl(110). The angles between chain axis (dotted lines) and NiAl [001] direction (straight lines) are indicated. (b,d) Schemes showing the orientation of the (idealized) hexagonal Al_s lattice (gray circles) with respect to the NiAl substrate. Please note that the real Al_s lattice is slightly distorted (cf. Fig. 3.2 and Ref. [1]). The dotted lines reflect the extension and orientation of Au pentamers, probable adsorption sites of Au atoms are marked with yellow circles.

4.4 Electronic Properties

4.4.1 Experimental Results

The electronic properties of Au monomers, dimers and chains have been studied using STS and conductance imaging. Usually, Au adsorbates are stable at positive sample bias until 3.3–3.5 V, allowing a detailed investigation in this range. STM studies at negative sample bias are more difficult, since tunneling out of occupied levels can easily lead to desorption of the Au species, especially in the case of monomers and dimers. This is shown in Fig. 4.9 for three Au particles, **A**, **B**, and **C**. They are investigated by constant current (top) and conductance imaging (bottom) in an energy range of -2.0 to -3.3 eV below the Fermi level. **B** and **C** appear round with a diameter of about 10 Å and are most probably monomers. The composition of **A** cannot be identified unambiguously. It has also round shape but is imaged much bigger than **B** and **C**. Therefore, **A** might be a small cluster or a monomer, which appears bigger due to resonant tunneling into its lower-lying highest occupied level. The latter can be estimated from the dI/dV image recorded at -2.7 V, where **A** is much brighter than

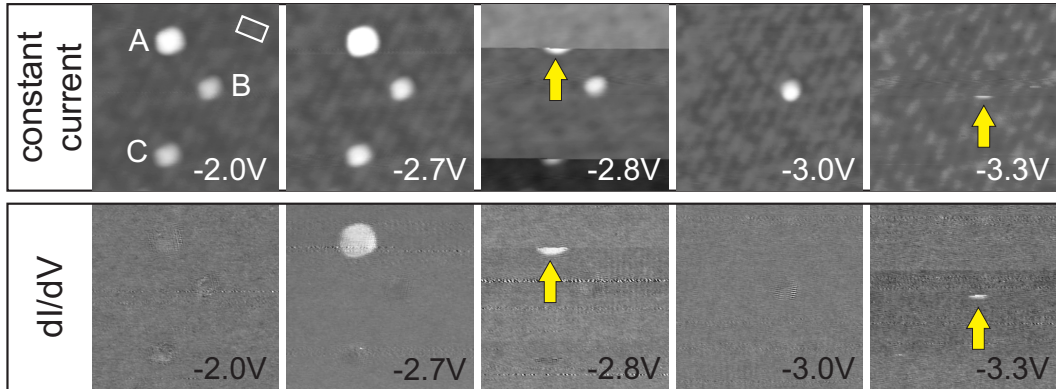


Figure 4.9: Constant current and dI/dV images of three Au species, **A**, **B**, and **C** on the alumina film on NiAl(110) ($129 \text{ \AA} \times 129 \text{ \AA}$, $I_t = 0.2 \text{ nA}$). V_s is indicated at the bottom of the images. The white rectangle marks the oxide unit cell. **B** and **C** have a diameter of $\sim 10 \text{ \AA}$ and are most probably monomers. **A** might be a small cluster or a monomer appearing bigger due to its lower-lying highest occupied state (at about -2.8 eV). **A** and **B** desorb when tunneling into their occupied states at -2.8 eV and -3.3 eV , respectively (arrows). **C** desorbs at $V_s = -2.8 \text{ V}$ though no increased conductivity is detected in the dI/dV image.

the surrounding oxide due to the increased conductance. This indicates the onset of an occupied level close to -2.7 eV . A further decrease of the energy leads to desorption of **A**. Both constant current and conductance image taken at -2.8 V show still the edge of **A**, which then disappears from the image. The same happens to monomer **B** at -3.3 V , whereby the onset of an occupied level can be deduced from the dI/dV image. The dramatic increase of the dI/dV intensity proves that desorption is not the result of a field effect induced by the tip, but follows the depopulation of Au electronic levels at a certain energy below E_F . Monomer **C** desorbs even without evidence of resonant tunneling into an occupied level at $V_s = -2.8 \text{ V}$.

Monomers

The results described in the previous section reveal several difficulties related to the investigation of Au monomers. First of all, monomers cannot always be distinguished from Au aggregates on the basis of STM images. If a Au species has round shape and a size of $\sim 10 \text{ \AA}$, it is most probably a monomer. However, the apparent size will increase if the sample bias is chosen below the highest occupied or above the lowest unoccupied level, respectively. Here, these levels contribute to the tunneling current, since STM detects the integrated DOS between E_F and eV_s . These considerations show that monomers are difficult to identify if no STM image can be acquired under off-resonant tunneling conditions (e.g. for stability reasons) or if the sharpness of the tip hampers the determination of the size. Therefore, it is necessary to find additional

criteria, e.g. electronic properties, which are specific for monomers.

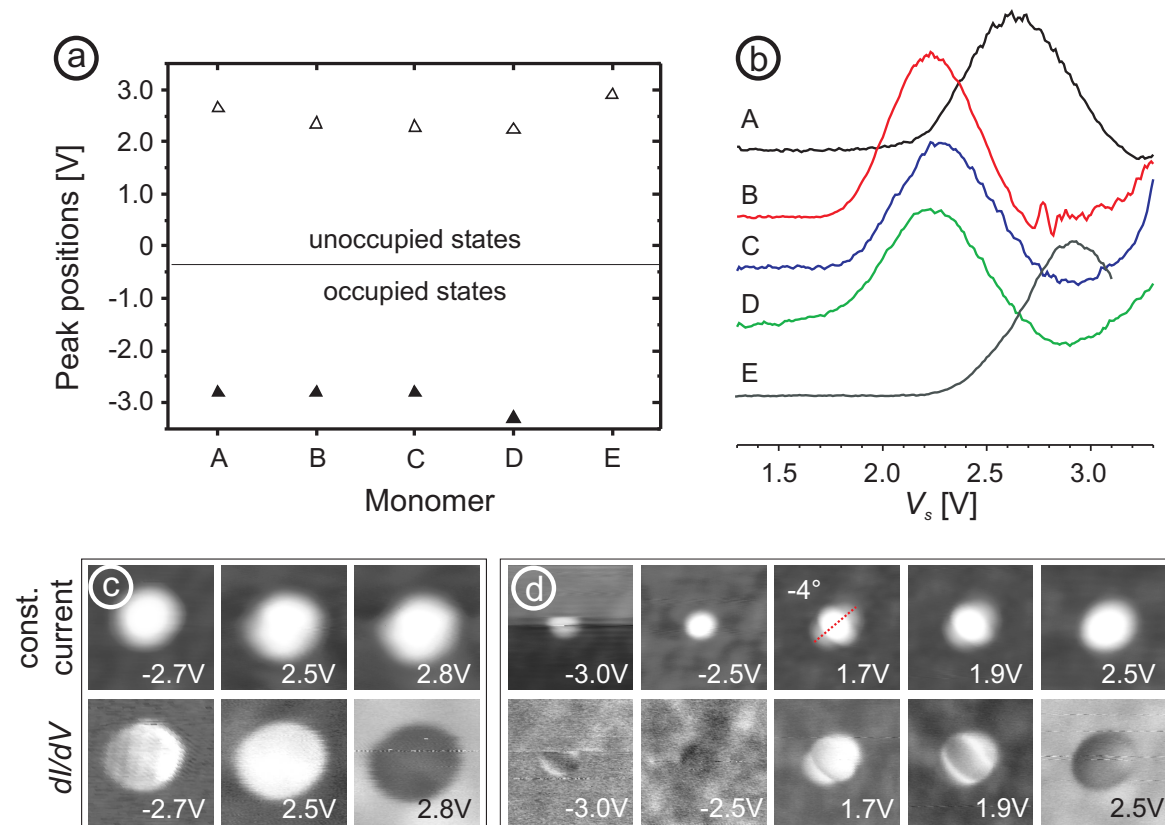


Figure 4.10: (a) Diagram showing typical energy levels of occupied and unoccupied states of Au monomers (A, B, C, D, and E) on the alumina film. The unoccupied states were investigated by STS (b), while the energy of the occupied states could only be estimated from dI/dV images. For monomers with a resonance at ~ 2.9 V (E), the occupied state could not be detected. (c-d) Constant current and dI/dV images of Au monomers ($43 \text{ \AA} \times 43 \text{ \AA}$, $I_t = 0.5 \text{ nA}$). The states are either distributed homogeneously over the monomer (c) or show a distinct substructure (d). The latter symmetry was observed only for Au species with peaks at ~ 2.3 V (cf. atom C in (b)). So far, it is not clear, why this state appears at much lower energy (between 1.7 and 1.9 eV) in conductance images. A small shift between maxima in dI/dV spectra and images is expected from the different tip-sample separations and tip-induced electric fields. However, such a big shift should not be observed.

Figure 4.10 summarizes spectroscopic data for Au particles which are supposed to be monomers because of their size and shape. The diagram in Figure 4.10 (a) shows sets of occupied and unoccupied resonances for five different Au monomers. Occupied levels were estimated from dI/dV images, in which Au monomers exhibited an increased conductance as compared to the surrounding oxide. Because of the facile desorption (see previous section), only a few data could be obtained that way. According to these, typical energies of occupied levels lie around -2.7 and -3.3 eV. Unoccupied levels are much easier to investigate, because no desorption occurs when tunneling into empty states.

The data shown in Figure 4.10 (a) have been determined by STS. The corresponding spectra are depicted in Fig. 4.10 (b) and reveal each a single dI/dV peak with a FWHM of 0.35 to 0.45 V. The peak positions at 2.3, 2.6 and 3.0 V can be considered typical for Au monomers, which is concluded from additional STS data not shown here. The data reported so far suggest that monomers are characterized by each a single occupied and unoccupied level, which have an energy separation between 5.0 and 5.8 eV. The symmetry of these levels was investigated by conductance imaging. Most monomers show a homogeneous LDOS distribution over the whole atom. An example is provided in Fig. 4.10 (c). The large diameter of the Au adatom (20 Å) results from the resonant tunneling conditions and the slightly blunt tip. At -2.7 V and 2.5 V, the Au atom exhibits increased conductance as compared to the surrounding oxide, indicating the presence of discrete electronic states. At energies that do not coincide with an electronic level of the Au monomer (e.g. at 2.8 eV), the latter appears as depression in dI/dV images. The reason is, that in this case only electronic states of the alumina film contribute to the dI/dV signal. However, the distance between tip and oxide is larger if the tip is positioned over the Au adatom, because of the adjustment of the tunneling current. As a result of the increased tip-oxide separation, the dI/dV signal over the Au adatom is weaker. Figure 4.10 (d) shows constant current and dI/dV images of a Au species, which should be a monomer according to its shape and size in the STM image measured at -2.5 V. However, dI/dV images reveal a distinct substructure instead of a homogeneous LDOS distribution. This might be the result of a tip effect, but similar structures were observed repeatedly (cf. the monomer in Fig. 4.16). Thus, the symmetry of the LDOS seems to be an intrinsic property of these Au species. A detailed analysis of the dI/dV images shows, that all of these Au species are characterized by a decreased conductance in the middle at certain energies (here at 1.9 and -3.0 eV). The axis connecting the thus defined ends of the Au adsorbate has the same characteristic orientation as Au chains and most dimers on the alumina film (see Fig. 4.10 (d) and Section 4.3.4). Thus, it might be questioned if these Au species are really monomers on a special adsorption site [149] or dimers with a shorter Au-Au separation, where Au adatoms occupy adjacent Al_s sites instead of every second. To address this question, typical properties of Au dimers were studied for comparison (see next section). The presented results underline the difficulties related to the identification of monomers, which hamper a statistical analysis of the spectroscopic data.

Dimers

Dimers that are oriented close to the [001] direction of NiAl(110) and that have an adatom separation of ~ 6 Å, exhibit very similar electronic properties, which are summarized in Fig. 4.11. The data are all obtained for positive sample bias. No resonances

could be detected at energies below the sample Fermi level due to the stability problems discussed above. Figure 4.11 (a) shows a constant current STM image of three dimers

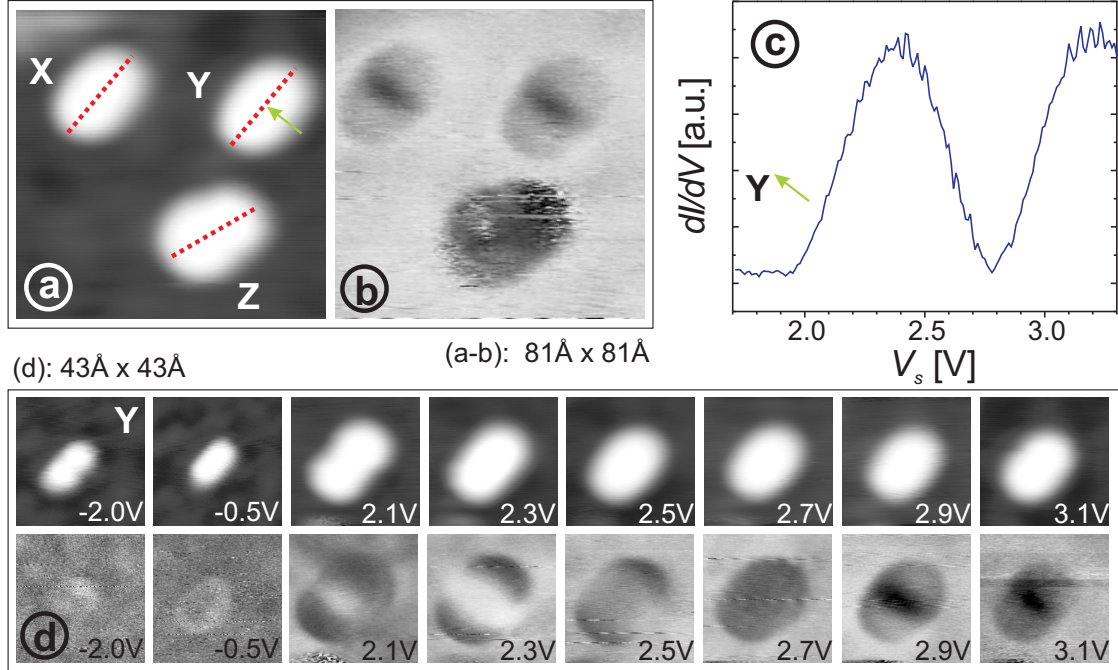


Figure 4.11: Constant current (a) and conductance image (b) of three Au dimers on the thin alumina film ($V_s = 3.0$ V, $I_t = 0.5$ nA). Dimers **X** and **Y** have the same orientation which corresponds to the most frequently occurring in the A domain (cf. Fig. 4.7). They also exhibit very similar electronic properties, shown representatively for **Y** (c-d). (c) Conductance spectrum of **Y**, recorded at the position marked with an arrow. (d) Constant current and conductance images of **Y** at the indicated sample bias.

X, **Y**, and **Z**. Two of them (**X** and **Y**) have not only the same orientation close to the [001] direction of NiAl(110), but they exhibit also the same characteristic signature in dI/dV images, shown in Fig. 4.11 (b) for $V_s = 3.0$ V. The corresponding conductance spectrum is displayed in Fig. 4.11 (c). It was recorded in the middle of dimer **Y** (at the position indicated by the arrow), and is representative for most dimers with this orientation. The spectrum exhibits two peaks at 2.4 and 3.2 V. The spatial localization of either electronic level can be deduced from the conductance images shown in Fig. 4.11 (d). At 2.3 V, i.e. close to the energy of the first dI/dV peak, the conductance of the Au dimer is not homogeneously distributed but has a pronounced maximum between the two Au atoms. The inverse situation is observed if the sample bias is chosen close to the second unoccupied level. Here, the conductance shows two maxima that are localized at both ends of the dimer, separated by a nodal plane. It is important to note, that the dI/dV images display the conductance of the dimer with respect to that of the surrounding alumina film. Since the latter one increases with energy and exceeds

the conductance of the Au dimer above 2.5 V, the second, higher-energy level appears as depression in dI/dV images. For a “free” dimer, the symmetry of the two states resulting from the hybridization of the original adatom orbitals could be described in terms of a bonding and an antibonding orbital, respectively. However, for dimers that are bound to a surface, such description is not necessarily appropriate, since the states investigated here are unoccupied and do not contribute to the Au binding. Therefore, the terms *symmetric* and *antisymmetric* are better suited to describe the symmetry of these levels.

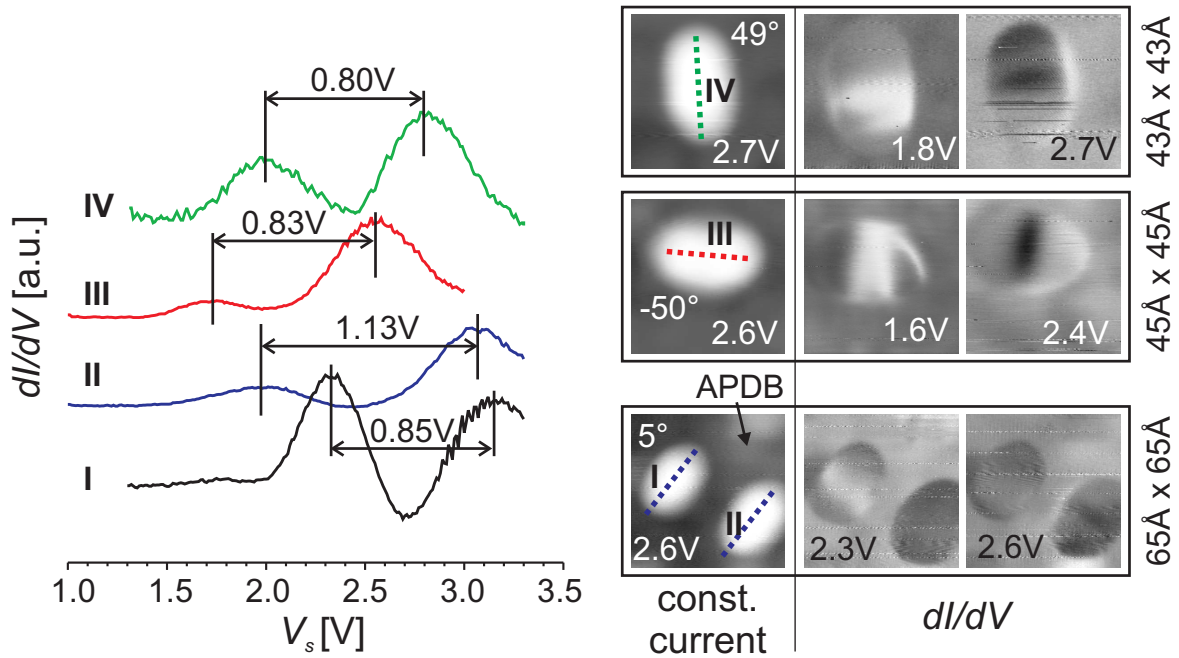


Figure 4.12: Conductance spectra and conductance images ($I_t = 0.5$ nA) of Au dimers with different adsorption configuration on the thin alumina film.

Investigations on dimers with other orientation reveal similar charge distribution, as shown in Fig. 4.12 for four dimers. Dimer I and II have the same orientation, close to the [001] direction of NiAl(110), however II is adsorbed on an APDB. The orientation of dimers III and IV is different. In any of these cases, a set of two unoccupied states can be identified, whereby one is symmetric and the other antisymmetric. The level splitting for dimers on pristine alumina terraces (I, III, and IV) is very similar (between 0.8 and 0.85 V), while the peak positions differ by up to 0.7 V. For adsorption sites on APDB (dimer II), an increased peak-to-peak separation (1.13 V) is observed.

Trimers, Tetramers, and Pentamers

Spectroscopic data for Au trimers on alumina / NiAl(110) are shown in Fig. 4.13. Except from T2, all trimers have the same, characteristic orientation, i.e. $\pm 5^\circ$ with respect to the [001] direction of NiAl(110). Conductance spectra at negative sample bias show

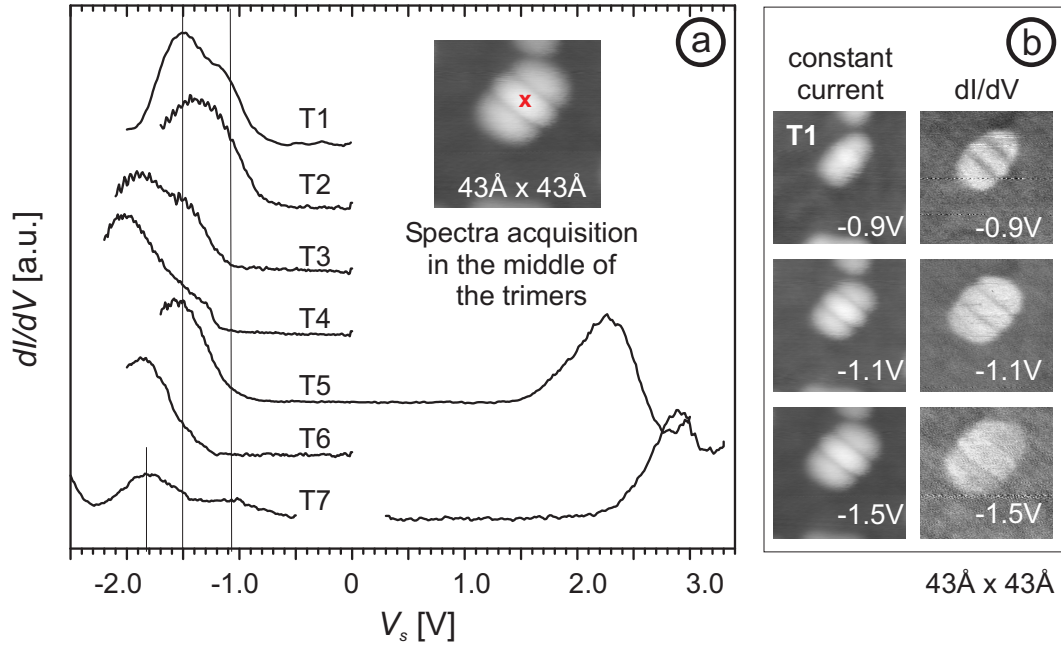


Figure 4.13: (a) Conductance spectra of seven different of Au trimers, T1–T7, on alumina/ NiAl(110). Except from T2, all of them have the same characteristic orientation, i.e. $\pm 5^\circ$ with respect to the [001] direction of NiAl(110) (T2: 25°). For spectra acquisition, the tip was positioned over the middle lobe of the trimer. (b) Constant current and conductance images of trimer T1.

one or two peaks, whereby the energy of the highest occupied level ranges from -1.1 to -1.5 eV. If two peaks are present, their energy difference varies between 0.4 and 0.7 eV. At positive bias, only few data have been obtained, such that relevant information is hardly deducible. Conductance spectra reveal one or two peaks in the investigated range. However, the existence of resonances at higher energy is likely. The spectra shown in Fig. 4.13 (a) are all recorded with the tip being positioned over the middle of the three lobes. Conductance images can be used to detect the spatial distribution of the determined levels. An example is shown in Fig. 4.13 (b) for trimer T1. Both states at -1.1 and -1.5 eV are localized at each of the three lobes visible in constant current images. The same behavior was observed for all Au trimers.

Spectroscopic data on Au tetramers are sparse, and the energy of the highest occupied level can only be estimated from dI/dV images. An example is shown in Fig. 4.14. At -1.5 V, the conductance over each of the four lobes is slightly increased compared

to the surrounding oxide, which indicates the onset of an electronic level. The effect is even more pronounced at -1.7 V. The exact energy of the corresponding electronic state cannot be determined directly from dI/dV images, because the conductance is already increased at the slope of the peak. However, assuming a FWHM of 0.4 V (as observed in other Au particles) the electronic level should have an energy of -1.6 to -1.8 eV. This resonance reflects also the highest occupied state, since no further resonances have been detected at smaller negative sample bias.

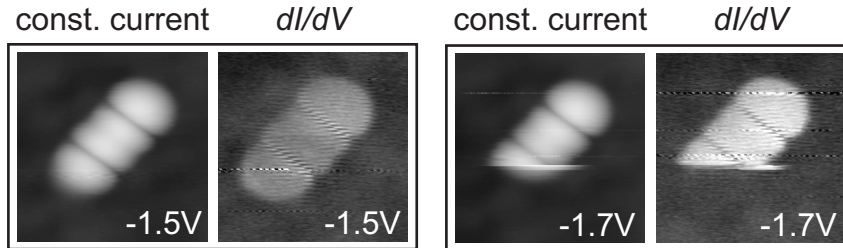


Figure 4.14: Constant current and conductance images of a Au tetramer (43×43 Å, $I_t = 0.5$ nA). The latter desorbed during image acquisition at $V_s = -1.7$ V.

Fig. 4.15 summarizes the STS data of a typical Au pentamer in the range between -2.2 V and 3.4 V. At negative V_s , two resonances can be detected by STS. The highest occupied state has an energy of -1.3 eV, and the energy separation to the next level at -1.8 eV is ~ 0.5 eV. Both states are located at either of the five lobes (Fig. 4.15 (a), spectrum I) and almost vanish in between the lobes (spectrum II). This finding is confirmed by the dI/dV images in Fig. 4.15 (c), revealing the same symmetry for both negative resonances. It is important to note, that the second resonance appears as depression in dI/dV images because of the higher conductance of the surrounding oxide at this bias. As a result, the symmetry of this state is not as well resolved as that of the -1.3 eV level. However, the same five-fold structure is distinguishable as for the higher-energy state. At positive V_s , three states at 1.8 V, 2.5 V and 3.3 V can be identified that are localized only at specific parts of the chain (Fig. 4.15 (b,d)). The peaks at 2.5 and 3.3 V are localized each at one end of the Au pentamer, whereby the 3.3 V level is more difficult to distinguish in dI/dV images because of the comparable conductance of the oxide at that sample bias. The sharp peak at 1.8 V appears always in the middle of the pentamer and, with smaller intensity, at that end of the pentamer, where the 3.3 V state is localized, too. In contrast to peaks at negative sample bias, positive resonances are always delocalized over more than one adatom in the chain. The peak positions and their localization within the chain were obtained repeatedly with different tips for both oxide domains. An influence of the tip can therefore be excluded. Furthermore, this finding indicates a narrow variation of available adsorption sites for Au pentamers.

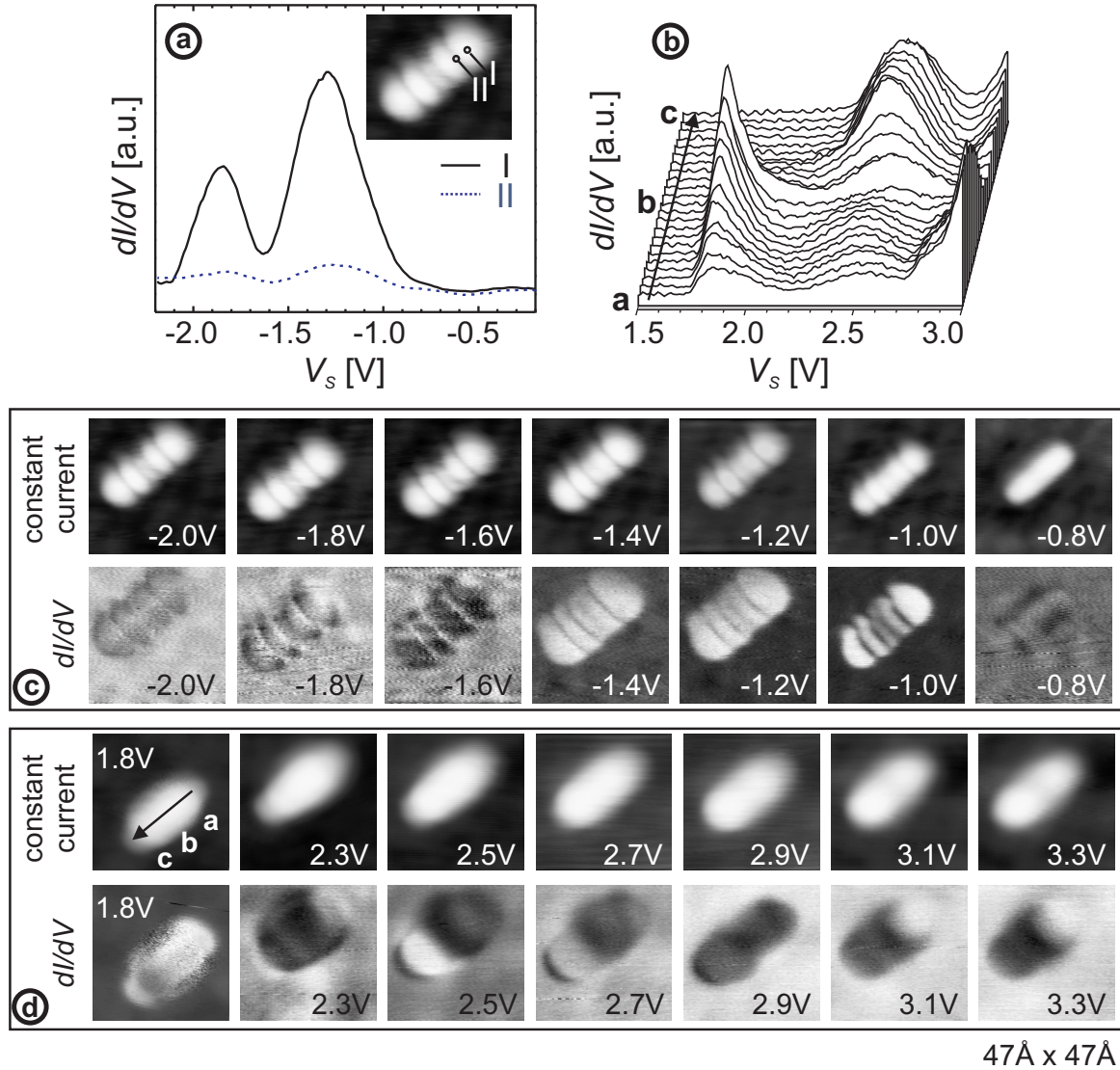


Figure 4.15: Conductance spectra, constant current and conductance (dI/dV) images of a typical Au pentamer on alumina/NiAl(110). For better visualization, the intensity of the dI/dV images was scaled. (a) At negative sample bias V_s , two resonances are detected, which are localized at either of the five lobes visible in the inset (position I). In between the lobes, nodal planes with strongly reduced conductance are observed (position II). The symmetry of these states is also reflected in the dI/dV images of (c). (b) Conductance spectra taken at positive V_s differ along the axis of the Au chain. (d) According conductance images.

Fig. 4.16 shows a series of constant current and conductance images of a pentamer, the structure of which undergoes modifications during image acquisition. Initially ($V_s = -1.5\text{ V}$, structure I), the pentamer is imaged with the typical lobe structure described above. After switching the polarity between tip and sample and starting a new scan, a sudden change in the appearance of the Au chain is observed ($V_s = 1.9\text{ V}$, small arrow). The uniform, elongated shape vanishes, and the middle part of the Au chain appears now bigger. Subsequent imaging of this structure at negative V_s reveals a similar appearance in constant current images (structure II). The initial symmetry reflecting the electronic states is broken, and the characteristic lobe structure is no more observed. Instead, the Au aggregate appears as uniform chain with a bulge at the lower middle part. Conductance images reveal furthermore a new resonance at about -2.2 V , which is localized at two areas: at the bulge and at the uppermost part of the chain, separated by a nodal plane. The resonance does not extend to the lower part of the Au aggregate. Switching the polarity between tip and sample anew, the well-known pentamer structure is obtained again, as can be referred from the characteristic dI/dV signatures at 2.5 V , -1.5 V , and -1.0 V .

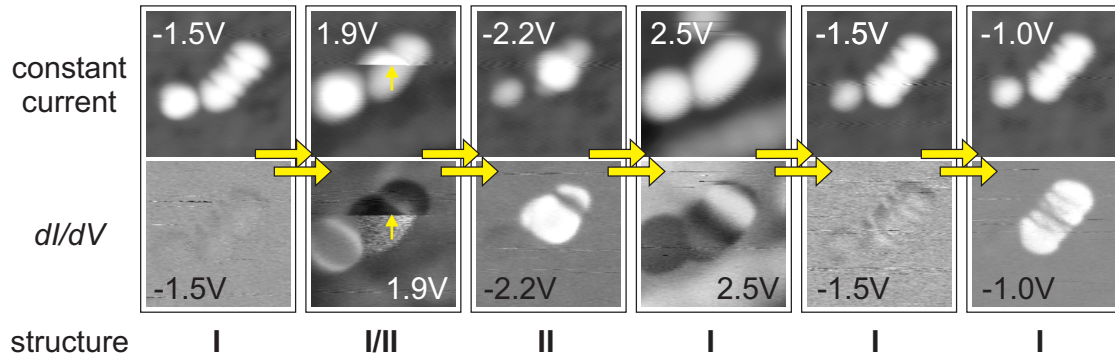


Figure 4.16: Constant current and conductance images of a Au pentamer ($65 \times 65\text{ \AA}$, $I_t = 0.5\text{ nA}$). The structure changes between two structures (I and II), due to interaction with the tip. The large arrows indicate, that further images were recorded, which are not shown here. The small arrows mark the change in the structure. Apparently, structure II is more compact, with at least partially reduced adatom distances than in I.

Usually, pentamers are quite stable even if the polarity of the tunneling junction is switched. The described observations are therefore presumably due to specific tip properties, which cannot be controlled in a systematic way. Two interpretations can account for the described observations. First, an additional Au atom might have been dropped on the initial Au pentamer by the tip. However, since the structural change is reversible, it is more likely that the position of a Au atom changed within the chain. Structure II appears more compact. This suggests that the adatom distance is reduced for some of the chain atoms, such that they occupy adjacent adsorption sites. Possibly,

the separation of the lower chain atoms to its next neighbor is increased in return. At least, this might explain why the resonance at -2.2 V does not extend over the whole chain. Though the structural change cannot be resolved in detail from the STM data, the results indicate that Au atoms can be displaced within the chain, thus supporting the hypothesis of large Au–Au separations. Moreover, this experiment underlines the close relation between a distinct geometric arrangement and electronic properties of the chain. Displacement of a single adatom in the aggregate induces dramatic changes in the LDOS.

4.4.2 Discussion

The interaction of Au atoms with alumina/NiAl(110) has not been studied computationally yet, which is mainly due to the high complexity of the substrate and the size of the alumina unit cell. However, the interaction of Au atoms with related oxide surfaces has been subject of a number of theoretical investigations, which are briefly presented. Furthermore, experimental results on similar systems provide valuable information for the interpretation of our data, notably studies on Pd atoms on alumina/NiAl(110) [115], Au atoms on NaCl/Cu(100), NaCl/Cu(111) [160], and TiO₂/Mo(110) [161] as well as on Au clusters on MgO(100) [162]. Based on these computational and experimental works, the spectroscopic data described in the last section are discussed qualitatively, whereby the focus will be on conclusions for the Au–alumina and the Au–Au interactions on the alumina film.

Binding Mechanisms of Au Atoms on Oxides

Several DFT calculations investigate the interaction of Au atoms with oxides and oxide thin films. Usually, periodic supercells are used, where Au is adsorbed on the oxide with low coverage, e.g. 1/3 ML [153, 154, 159]. Central questions of these studies concern binding mechanisms, preferential adsorption sites, adsorption energies (E_a) and lattice relaxations induced by the adatom. Most models describe the Au–oxide (Al₂O₃, MgO) interaction as covalent bond with partial charge transfer (CT), which is accompanied by substantial lattice relaxations. Accordingly, the adsorption of a Au atom on the oxide induces a pair of states below and above the Fermi level, within the oxide band gap [163]. The character of these states depends strongly on the substrate. For Au on MgO, for instance, it is described as hybridization of O 2*p* levels with Au 5*d* and 6*s* states [163]. In other models, Au is supposed to participate mainly via its 6*s* orbital [153, 154, 159], which is intuitive, considering the electronic configuration of Au: [Xe] 4f¹⁴ 5d¹⁰ 6s¹.

The calculated adsorption energies differ for the various models. On α -Al₂O₃,

$E_a = 0.78$ eV and $E_a = 0.81$ eV are predicted for the adsorption of Au on top of Al and O, respectively. On MgO(100) and Ce₂O₃, similar values are obtained for adsorption on top of O ($E_a = 0.89$ eV [163] and 0.86 eV [164], respectively). For Au adsorption on CeO₂(111), a slightly increased value of 1.26 eV is calculated [164], which can be rationalized by the higher oxidation state of Ce (+4), leading to a stronger oxidation of the Au adatom. In general, Au^{δ+} adatoms bind rather to anion sites (in oxides O²⁻), while Au^{δ-} will preferentially bind to cation sites because of the resulting favorable electrostatic interaction between adsorption site and adatom. The energetic preference for either anion or cation site will depend on the partial charge of the Au adatom.

On thin oxide films, stronger interactions with Au adatoms have been predicted. So, a much higher adsorption energy ($E_a = 2.3$ eV for Al threefold hollow sites) is calculated for Au on Al₂O₃ / Al(111) as compared to α -Al₂O₃. Recent studies on thin MgO films suggest furthermore, that other mechanisms might prevail for the adatom interaction with oxide thin films: A CT in the inverse direction, i.e. from the support to the adatom, is predicted for the Au adsorption on thin MgO films on Mo(100) [50, 155]. The effect is explained with the high EA of Au and with the reduced work function (Φ) of the Mo substrate if supporting MgO films ($\Phi = 2.1$ eV [50, 155]). Accordingly, the energy of the Au 6s level shifts below the Mo Fermi level, resulting in a negative charging of the Au adatom. The electrons are provided by the Mo substrate and are suggested to pass the oxide barrier by tunneling [152, 155]. Thus, such binding mechanism would be possible only in thin oxide films. The comparison of the Au adsorption on bulk MgO and on thin MgO films reveals (i) an increase of the adsorption energy (2.21 eV) and (ii) a preference for cation sites on the oxide film.

The significance of each model for the present studies is difficult to evaluate. At first glance, the studied substrate resembles most the alumina film on Al(111). However, that film has a slightly different structure, which is similar to κ -Al₂O₃. Additionally, and even more important, the authors of that work present also data for Ag adatoms, for which an adsorption energy ($E_a = 3.1$ eV) was calculated that is much larger than for Au. This is in clear contradiction to the experimental data presented in the last section, which reveal a much stronger interaction for Au than for Ag. Therefore, the applicability of this model to the present study has to be doubted. Investigations on bulk oxides will not describe the current data in an appropriate way, neither, since they cannot account for the participation of the NiAl substrate in the Au adsorption, which could already be concluded from the analysis of geometric features (Section 4.3). In this regard, studies on thin MgO films on Mo(100) are most promising. Nevertheless, a direct transfer of this model is not compelling because of the different chemical composition of both the oxide film and the substrate. Thus, the mentioned theoretical descriptions of the Au–oxide interaction are indicative for the interpretation of

the spectroscopic data, but cannot provide a detailed understanding of the involved interaction mechanisms.

Monomers

Experimentally, an occupied and an unoccupied state were detected for Au monomers on the alumina film. This agrees well with the common picture of a Au–oxide interaction, where the adsorption leads to a pair of states within the oxide band gap, presumably under participation of the Au 6s level. The latter fact is concluded from theoretical studies on similar systems and from experimental results for Pd adatoms on alumina / NiAl(110) [115], where the spectroscopic signature was assigned to originate from Pd 5s states. An *s,p* character of the Au–alumina bond is also indicated by the large spatial extension of Au adatoms in STM images, which points to delocalized *s* and/or *p* states above E_F . The charge state of the Au adatoms cannot be concluded directly from the STS data. However, the identification of cationic adsorption sites (Al_s^{3+}) suggests the presence of a $\text{Au}^{\delta-}$ species for the above mentioned reasons. Such negatively charged Au adatoms are known from various experimental and theoretical studies. They are observed, for instance, on oxide films containing oxygen vacancies, such as TiO_2 , CeO_2 or MgO [161, 163, 164]. These point defects usually act as a “trap” for Au atoms, since they contain two electrons, which favors the binding of Au atoms because of their high electron affinity. Experimentally, $\text{Au}^{\delta-}$ species have also been observed on regular sites of thin insulating films, namely on NaCl films on Cu(111) [160]. Both neutral and negatively charged Au adatoms were identified on the film, which are stabilized by the large ionic polarizability of the film. In those experiments, the charge state could be controlled with the STM tip. On regular oxide sites, negatively charged Au adatoms have not been detected experimentally yet. However, their existence has been predicted by a computational work on thin MgO films [50]. The following key factors have been suggested for the formation of $\text{Au}^{\delta-}$ species on the film: (i) the high electron affinity of Au, (ii) the strongly reduced work function of Mo(100) if supporting MgO films ($\Phi_{\text{Mo}(100)} = 4.4 \text{ eV}$, while $\Phi_{\text{MgO}/\text{Mo}(100)} = 2.1 \text{ eV}$ for 3 ML thin films) and (iii) the small film thickness which allows tunneling of electrons from the metal substrate to the adatom. As a result, the Au 6s level shifts below the Mo Fermi level and is thus occupied with two electrons. In the present study, conditions (i) and (iii) are fulfilled. The work function of bare NiAl(110) is $\Phi = 5.1 \text{ eV}$ [36], thus much larger than for Mo(100). It is known for several substrates, that the work function of a metal can be reduced when supporting an oxide film. However, the amount depends strongly on both oxide film and metal support. The decrease in Φ is, for instance, much smaller for MgO / Ag(100) [165] than for MgO / Mo(100) [155]. For NiAl in alumina / NiAl(110), this value is not available, such that condition (ii) cannot be evaluated. However, the

determined cationic adsorption site (Al_s^{3+}) and the participation of the NiAl substrate indicate, that a mechanism similar to the MgO case might prevail for Au adatoms on alumina / NiAl(110).

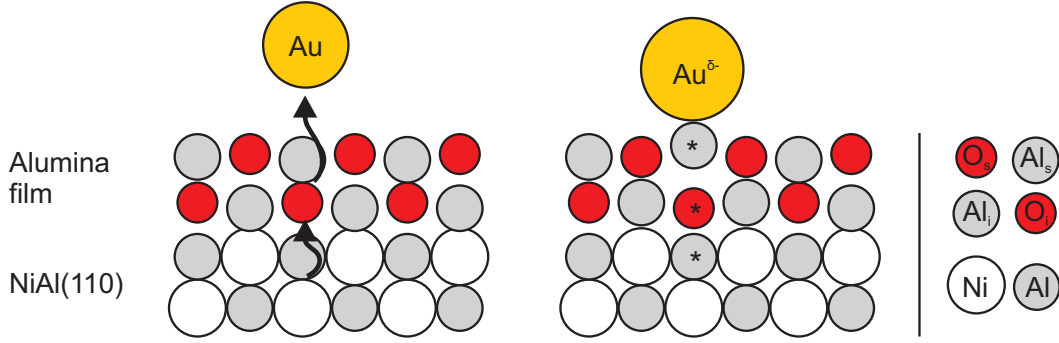


Figure 4.17: Schematics (side view) showing a possible interaction mechanism between a Au adatom and alumina / NiAl(110). The determined adsorption site (Al_s) suggests that Au is partially negatively charged ($\text{Au}^{\delta-}$) when bound to the alumina film. The electron transfer from the NiAl substrate to the Au atom is symbolized by arrows in the left scheme. The existence of a favorable geometric constellation between Au adatom, Al_s atom and the NiAl substrate was deduced from the properties of Au chains. One possible reason might be that the formation of the Au– Al_s bond leads to a break of the Al_s – O_i bond, such that the O_i atom moves downward and binds stronger to the NiAl substrate. The participating atoms are marked with a star. A similar mechanism was suggested for Au atoms on a Ti-doped SiO_2 film on Mo(112) [166]. In the present case, such mechanism has only speculative character. However, it shows how the Au adsorption might induce lattice rearrangements.

Based on these consideration, a simple model for the Au binding can be derived, which is shown schematically in Fig. 4.17. Au occupies Al_s sites and is supposed to have partial negative charge. As deduced from the analysis of Au chains, a special geometric arrangement between Au adatom, Al_s atom and the NiAl substrate is favorable. The exact atomic constellation cannot be resolved without computational support for that special adatoms-substrate system. However, there might be similarities to a recent theoretical work investigating the adsorption of Au atoms on Ti-doped SiO_2 films on Mo(112) [166]. The film consists of a single SiO_2 layer, whereby Si is partially replaced by Ti ($\text{Si}:\text{Ti} = 7:1$). These atoms are connected to the Mo(112) substrate via oxygen bonds. Adsorption of Au occurs preferentially on Ti, leading to a covalent Ti–Au bond at the expense of the Ti–O(–Mo) bond. In other words, Ti keeps its fourfold coordination, but exchanges O against Au. Consequently, the oxygen atom moves downward and binds more strongly to the Mo substrate, where interaction with the Mo $4d$ bands leads to complete spin pairing. The analysis of the DOS suggests that Au is (partially) negatively charged in this case, too [155]. A similar mechanism might prevail for Au atoms on alumina / NiAl(110). As described above, a special configuration between Au, Al_s , and Al/Ni atoms of the NiAl is favorable. This might be necessary to “hand over” an oxygen atom from the Al_s atom, which is now bound

to the Au atom, to the NiAl substrate. Such situation is depicted in the right part of Fig. 4.17. The involved atoms are marked with a star. Certainly, this mechanism is speculative and needs to be checked computationally. However, it gives an idea of how the NiAl support might be involved in the Au binding, and how the Au adsorption could induce lattice rearrangements.

Conductance spectra and conductance images of Au atoms on alumina / NiAl(110) show a relatively broad energy distribution of electronic levels for both occupied and unoccupied resonances. Similar observations have been made for unoccupied levels of Pd atoms on the same substrate [115]. These findings can be explained with the existence of different adsorption sites on the alumina film, which influence the electronic properties of the adatom, and thus the energy of the induced states. Different electronic properties would be expected, for instance, for the adsorption on tetrahedrally and pyramidally coordinated Al_s atoms. Probably, the latter are favorable, because Al can thus reach the preferred octahedral coordination. One also has to keep in mind that metal–oxide interactions vary over a wide range because of the incommensurate growth of alumina along the NiAl [001] direction, resulting in a variety of possible binding configurations.

Line Widths

Adsorbate-induced states in thin insulating films should have relatively narrow line widths, because they are electronically well decoupled from the underlying metal substrate. This seems to be in contradiction with the experimental observations, where dI/dV peaks of Au atoms have typically FWHM of 0.35 to 0.45 V and Gaussian shape. As discussed in Section 2.2.2, the broadening of dI/dV peaks due to finite temperature and modulation voltage should not exceed 0.05 V. Other factors, such as the properties of the tip, can be supposed to be negligible from a number of comparative measurements. Thus, intrinsic FWHM of dI/dV peaks are in the range of 0.3 to 0.4 V. Such broad line shapes were also observed in conductance spectra on other adatoms and molecules on thin insulating films [112, 115, 156]. The line widths are comparable with those of metal atoms on metal surfaces [60, 106]. However, the lifetime-broadening, which is the most important factor contributing to the intrinsic peak width of adsorbates, depends on the coupling of electronic states to the substrate and should be much larger on metal substrates due to their high LDOS as compared to thin insulating films. Therefore, another effect has to be responsible for the broadening of dI/dV peaks in the latter case. This question has been addressed in a combined theoretical and experimental (STM/STS) study of Cl vacancies in thin NaCl films on Cu(311), Cu(100), and Cu(111) [167]. In each case, the vacancy induces an unoccupied defect state with a characteristic energy of 2.0, 2.6 and 2.8 eV, respectively, whereby the dI/dV peaks have

again an unexpected large FWHM of 0.32 V, which is comparable to those detected on other thin insulating films. On the Cu(111) supported film, yet another resonance is observed that could be assigned to an interface-state localization (ISL). This peak, which shows a much smaller line width, results from the interaction of a Cl vacancy with Shockley-like interface state electrons. Comparing the line shapes of both peaks and using DFT calculations, the authors suggest that the vacancy state is broadened by a strong coupling to optical phonons ($\hbar\omega = 32$ meV) of the film, leading to a number of side bands ($E_0 \pm n\hbar\omega$). Presumably, the vibronic contribution is blurred in the spectra due to a band of phonon modes, thus only a broad resonance with Gaussian shape is detected in dI/dV spectra. A similar mechanism is likely to prevail in the thin alumina film on NiAl(110), especially because the film supports a set of intense optical phonon modes (Fuchs-Kliewer) below $\hbar\omega = 100$ meV [168]. Therefore, the observed line shapes are not in contradiction with the interpretation of these states as adsorbate-induced states of the Au adatoms.

Dimers

Conductance images of Au dimers clearly reveal a coupling of electronic levels of the two adatoms, leading to a symmetric and an antisymmetric state. This behavior is also manifested in the appearance of a doublet state above E_F in dI/dV spectra. Similar observations have been made for Au dimers on NiAl(110) [108, 115]. Here, the interaction between two adjacent Au atoms leads also to a splitting of the monomer resonance into two new states with symmetric and antisymmetric character, respectively. The peak-to-peak separation, ΔV , of 0.8 V is similar to that observed for Au dimers on the alumina film. However, this agreement is incidental, as the comparison of the Au–Au distances, d , on NiAl(110) (2.9 Å) and on the alumina film (5.6–6.0 Å) shows. A systematic analysis of ΔV as a function of d on NiAl(110) revealed a decay of ΔV with $1/d$ [149]. For $d = 5.7$ Å, which is similar to the separation here, ΔV is as small as 0.2 V and vanishes completely for larger d . According to DFT calculations, the Au–Au interaction is not only the result of direct orbital overlap between adjacent Au atoms, but strongly influenced by electronic states of the NiAl [108, 115]. For small d , they reduce the direct orbital overlap between Au atoms because of a strong hybridization of Au 6s, p orbitals with NiAl states. For larger d , the Au–Au interaction is mainly substrate-mediated, leading to a slower decay of the energy splitting than the expected exponential decrease. Considering the results for Au / NiAl(110), a direct orbital overlap in Au dimers on the alumina film can be excluded. Instead, the Au–Au interaction seems to be mediated by the substrate, possibly via Au-induced defect states in the oxide film. As shown for APDB, such defect states can have large extensions and might therefore interact over distances as large as observed here. Possible coupling

mechanisms between Au-induced lattice modifications include Coulomb or polaronic interactions via defect states induced in the alumina film.

Trimers, Tetramers and Pentamers

In contrast to Au monomers and dimers, occupied states of longer chains could be studied intensively by STS and conductance imaging. As described above, these 1D Au clusters exhibit a characteristic lobe structure in STM images, if the sample bias is chosen below the highest occupied level. In Section 4.3, each lobe was tentatively assigned to the position of a Au atom or a Au-induced electronic state. However, also other interpretations would be possible, since comparable symmetries are expected for dense-packed Au chains, where the electronic structure can be described in terms of a confined, 1D electron system. Such dense-packed, artificially assembled Au and Cu chains (with interatomic distances close to the bulk metal) were found to show particle-in-a-box like behavior on metal surfaces, i.e. a standing-wave pattern appeared in dI/dV images exhibiting an increasing number of maxima and minima with increasing V_s [60, 106, 108]. For 1D Au clusters on the alumina film, several observations clearly contradict the model of a dense-packed chain, sitting relatively decoupled on the oxide layer: first, the dI/dV patterns observed here are independent of V_s for filled states. This is shown in Figs. 4.13 and 4.15 for trimers and pentamers, where the two observed electronic states have each the same symmetry. Secondly, the energy distance of the highest occupied state to the Fermi level should be smallest for pentamers and increase for tetramers and trimers in that order. However, experimentally, the highest occupied state of trimers was found to be closest to the Fermi level, followed by pentamers and tetramers. Third, the empty states of Au pentamers are rather asymmetric, clearly contradicting a particle-in-a-box like behavior, as expected for dense-packed Au chains. Fourth, the tip-induced, reversible displacement of Au atoms within the chain (Fig. 4.16) suggests the existence of free adsorption sites in between these Au atoms. Based on these arguments, a dense arrangement of Au atoms in self-assembled chains on the alumina film can be ruled out, supporting the hypothesis of large Au–Au separations.

It is important to note that the formation of Au chains is not the consequence of the Au–Au interaction, but the result of the linear arrangement of favorable adsorption sites as induced by the interplay between alumina and NiAl support. Substrate-induced ordering of adatoms was also observed on other oxide films, e.g. for Au atoms on 1 ML thin FeO films on Pt(111) [116]. In that case, no chain-like but a hexagonal arrangement of the adatoms with Au–Au distances of 25 Å was described. The ordering was explained with the commensurate growth of FeO on Pt(111). In the present study, the Au–alumina interaction does not only govern the alignment of Au atoms in chains

but is also responsible for the large Au–Au separations within the chain, which are thus not in contradiction to typical Au–Au distances. Presumably, the Au adsorption on adjacent sites is less favorable because of repulsive interactions (e.g. Coulomb or polaronic), which is a further indication for a CT accompanying the Au adsorption.

The spectroscopic data of Au chains show important differences for the states above and below the sample Fermi level. In the latter case, all electronic levels in the investigated range have the same symmetry and are localized at characteristic lobes, which are separated by nodal planes. At positive sample bias, electronic levels differ dependent on the position in the chain and on the adsorption site. However, these levels extend over more than one atom along the chain, indicating a coupling between these states. The effect was most clearly observed in Au dimers. The different properties of occupied and unoccupied states might be explained with different localization and nature of states below and above the NiAl Fermi level. To analyze whether these states are more localized at the Au adatom or in the alumina film, they are compared with APDB in alumina / NiAl(110), cf. Section 3.3.2. In APDB, a small region in the oxide film with different stoichiometry induces unoccupied defect states in a large area of the surrounding oxide. Each state has a characteristic symmetry and is localized at specific regions in the oxide, such that straight APDB appear, for instance, as single or double strands. Occupied states related to Au chains have similar properties, since they extend over the whole chain, separated by nodal planes. In contrast, unoccupied states of chains are localized only at specific parts of the chain, whereby their energy seems to depend sensitively on the adsorption sites. This suggests, that occupied states are rather localized in the oxide, while unoccupied states seem to have more Au character. At first glance, it appears unreasonable to relate empty defect states in APDB with filled states induced in the oxide by Au atoms. However, taking into account the direction of electron transfer in either case, opposite localization of the defect states with respect to the NiAl Fermi level should be expected: in APDB, electrons are transferred from the oxide to the NiAl. To counterbalance the electron transfer, a band bending occurs around the defect, causing a local downward shift of VB and CB. As discussed above, an electron transfer in the opposite direction is expected for Au adatoms, i.e. from the NiAl to the adatom. This should induce a local upward shift of VB and CB, and hence occupied defect states in the alumina film. Conclusively, the above mentioned arguments suggest that occupied states induced by Au adatoms have more oxide character, while unoccupied states are more Au-like. This assignment is, however, not unambiguous and will require computational confirmation.

4.5 Summary

Gold has been evaporated onto alumina / NiAl(110) at a sample temperature of ~ 10 K and investigated by STM. Due to their initial thermal energy, Au atoms can move on the surface prior to thermalization. As a result, small clusters are observed beside monomers and dimers. At low coverage, some of these clusters are one-dimensional with a maximum length of 22.5 \AA and a preferential orientation close to the [001] direction of the underlying NiAl(110). The precise chain orientation differs by $\pm 5^\circ$ from this substrate direction, dependent on the oxide domain. These findings strongly suggest a participation of the NiAl in the binding of Au atoms, whereby the small domain-dependent deviation in orientation can be rationalized by the alignment of possible Au adsorption sites, most probably Al_s atoms. The limited chain length is then explained with the divergence between Al_s rows and close-packed metal rows of the NiAl substrate. Atomically resolved STM images support the assumption that Au atoms are located on top of Al_s atoms. Gold chains appear with a distinct lobe structure in STM images, if the sample bias is chosen below their highest occupied state. The distance between adjacent lobes is $5.6 - 6.0 \text{ \AA}$ and thus almost twice as large as the Au–Au distance in bulk gold. Despite this fact, each lobe is interpreted as position of a Au atom or a Au-induced electronic state, defining the chains as trimers, tetramers and pentamers.

The electronic properties of Au monomers, dimers and chains have been studied by STS and conductance imaging. Conductance spectra of monomers reveal a single unoccupied level between 2.3 and 3.0 V with a FWHM of 0.3–0.4 V. Electronic states below the Fermi level are not accessible by STS, since electron tunneling out of occupied orbitals induces desorption of the Au adatom. However, conductance images indicate the presence of an occupied level with an energy between -2.7 and -3.3 eV (below the sample Fermi level). The set of unoccupied and occupied resonance is tentatively ascribed to the Au 6s level, which splits due to the interaction with the alumina film. The unoccupied level of Au monomers splits into two resonances for dimers, which are usually separated by 0.80 to 0.85 V on pristine alumina terraces. Conductance images reveal that the resonance at lower energy is located at the dimer center, while the higher-energy level is localized at both ends of the dimer. The large splitting energy indicates a strong interaction within the Au dimer. However, the large Au–Au distance of $\sim 6 \text{ \AA}$ prohibits an interpretation as direct orbital overlap, and a substrate-mediated interaction is suggested instead. The electronic properties of Au trimers, tetramers and pentamers do not evolve in a systematic way, i.e. no clear tendency can be determined for neither onset nor splitting energies of occupied and unoccupied levels when passing from shorter (trimers) to longer (pentamers) chains. This is in agreement with conclusions from spatially resolved spectra and conductance images,

which rule out a dense arrangement of Au atoms within the chain and support the hypothesis of large Au–Au distances.

The observations reveal clearly a participation of the NiAl substrate in the binding of Au atoms. Accordingly, the adsorption properties of the alumina film toward Au atoms differ from those of bulk alumina. Initial, comparative STM studies on other metal adatoms (Pd [115], Ag) on alumina / NiAl(110) do not indicate an influence of the underlying metal substrate in the adatom binding. Therefore, the high electron affinity of Au might be responsible for the participation of the NiAl. In summary, the results show, that adsorption properties of thin films might differ significantly from those of bulk oxides, requiring a careful analysis for each system.

Chapter 5

Metal Clusters on the Thin Alumina Film

This chapter presents STM studies on size-dependent electronic properties and the tunneling behavior through single Ag clusters on the thin alumina film. STS and conductance imaging are used to detect both properties with spatial resolution. The results are compared to preliminary studies on Pd clusters on the alumina film.

5.1 Introduction

Many heterogeneous catalysts consist of oxide-supported metal clusters. As previous studies have shown, both the size and the shape of these clusters can influence or alter the catalytic activity decisively [39], and it is therefore of great importance to investigate this dependence. On the one hand, kinetic studies on (model) catalysts with different composition and geometry can provide information on adsorption and diffusion properties as well as the catalytic activity [40]. However, these methods always average over large cluster ensembles, hampering a direct correlation between cluster parameters and reactivity. Therefore, it is also very important to know how the properties of single clusters are related to their geometric parameters. For such studies, a local method is needed, which is sensitive to characteristic cluster properties. Here, the STM provides a perfectly suited tool. Its unrivaled spatial resolution allows the topographic characterization of single clusters down to the atomic scale [169]. In combination with STS, spatially resolved electronic information can be obtained. The potential of this method has been demonstrated for various cluster-support systems. A series of discrete STS resonances was detected for Pt clusters on HOPG, although a straightforward dependence on the cluster size could not be derived [170]. Quantization of surface states was observed on the top facet of Au and Ag clusters on HOPG [111, 171, 172]. Energy

splitting and spatial localization of the levels could be rationalized by a two-dimensional (2D) particle-in-a-box model. On ligand stabilized metal particles, pronounced peaks in STS were ascribed to Coulomb charging effects caused by the localization of clusters between two tunneling junctions [122, 173, 174]. Similar results have been reported for metal clusters on self-assembled monolayers (SAM) [175].

Electron confinement in oxide supported metal clusters is believed to have a strong influence on their reactivity in heterogeneous catalysis [176, 177]. This has been demonstrated, for instance, for the low-temperature CO oxidation on TiO₂-supported Au clusters [176]. STS, STM and elevated pressure reaction kinetics measurements showed that the sensitivity of this reaction is related to quantum size effects in the Au cluster. Apparently, clusters with two-layer thickness are especially suited to catalyze the CO oxidation, which was ascribed to the specific band gap inherent to these particles. This example underlines the importance of size-dependent investigations of the electronic properties of clusters. Nevertheless, only a few studies have investigated this point for single oxide-supported metal particles, so far. In the present experiments, low-temperature STM and STS were employed to study the electronic properties of single metal clusters deposited on the alumina film on NiAl(110).

5.2 Experimental Results

5.2.1 Silver Clusters

Nucleation and Cluster Shapes

Silver was deposited as described in Section 2.5.4. Nucleation and growth of the clusters occur on oxide step edges, leading to the formation of isolated clusters with an average density of $5 \cdot 10^{11} \text{ cm}^{-2}$ (Fig. 5.1). Cluster diameters could be adjusted between 5 and 12 nm by varying the Ag dose [178]. The particles preferentially grow with hemispherical shapes, but show sometimes well-defined triangular and hexagonal top facets, as depicted in Figs. 5.1 (b-c). Such geometry reflects the threefold symmetry of Ag(111), indicating a crystalline structure and the presence of ordered (111) top facets [169]. The mean diameter-to-height ratio of the clusters was determined to be 1.7, whereby cluster diameters were corrected as described in Section 2.1.5. The cluster volume was taken to be the volume of a semi-ellipsoid with measured cluster height and diameter as input parameters [178]. Cluster shapes reflect the thermodynamic growth regimes of many metals on oxide surfaces. Due to the low surface free energy of oxides with respect to metals and the small metal-oxide adhesion energy, the formation of compact 3D clusters is preferred.

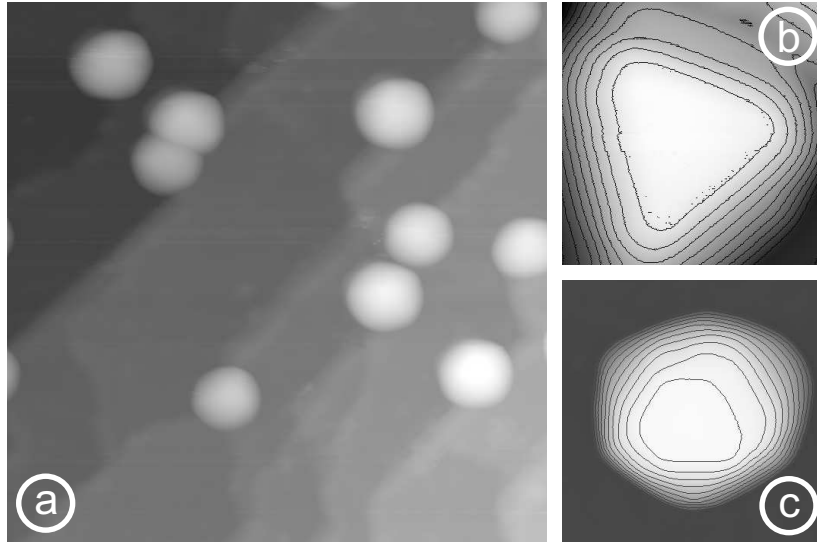


Figure 5.1: (a) Constant current STM image ($260 \text{ \AA} \times 260 \text{ \AA}$) of Ag clusters on the alumina film recorded at $V_s = 1.5 \text{ V}$, $I_t = 0.1 \text{ nA}$. Close-ups ($85 \text{ \AA} \times 85 \text{ \AA}$) of single clusters with (b) triangular and (c) hexagonal shape measured at $V_s = -0.5 \text{ V}$, $I_t = 0.1 \text{ nA}$. Each contour line represents a height change of 4 \AA .

STS and Conductance Imaging

The electronic properties of Ag particles on the thin alumina film were examined by STS (cf. Section 2.2), detecting the first derivative of the tunneling current (dI/dV) as a function of V_s with a lock-in amplifier ($V_{mod} = 10 \text{ mV}_{rms}$, $f_{mod} = 680 \text{ Hz}$). Figure 5.2 shows a series of spectra taken in the center of different Ag clusters in comparison to a spectrum of the bare alumina film. The oxide conductance is characterized by a single broad maximum at -0.5 V attributed to an electronic state localized at the NiAl-alumina interface. The cluster spectra are dominated by a series of discrete dI/dV resonances, which are nearly equidistant in the examined energy range. Typical peak widths are as small as 50 mV (FWHM). The peak positions are not symmetric with respect to the Fermi level and vary strongly from cluster to cluster. However, the energy separation $\Delta E = e\Delta V$ between neighboring peaks exhibits a distinct correlation with the cluster size. The energy separation in Fig. 5.2 decreases from 0.85 eV for the smallest cluster ($d = 75 \text{ \AA}$) to 0.56 eV for the larger ones ($d = 125 \text{ \AA}$). This trend of a decreasing peak-to-peak separation with increasing cluster size was generally observed for Ag clusters on the alumina film and is summarized in Fig. 5.3. The solid line is a least square fit of the data to $\Delta E \propto V^{-\alpha}$ with $\alpha \sim 0.3$.

Information on the spatial localization of conductance peaks within a cluster was obtained from series of dI/dV spectra taken along a line across the cluster surface. For the Ag particle shown in Fig. 5.4, five equidistant resonances P1-P5 have been

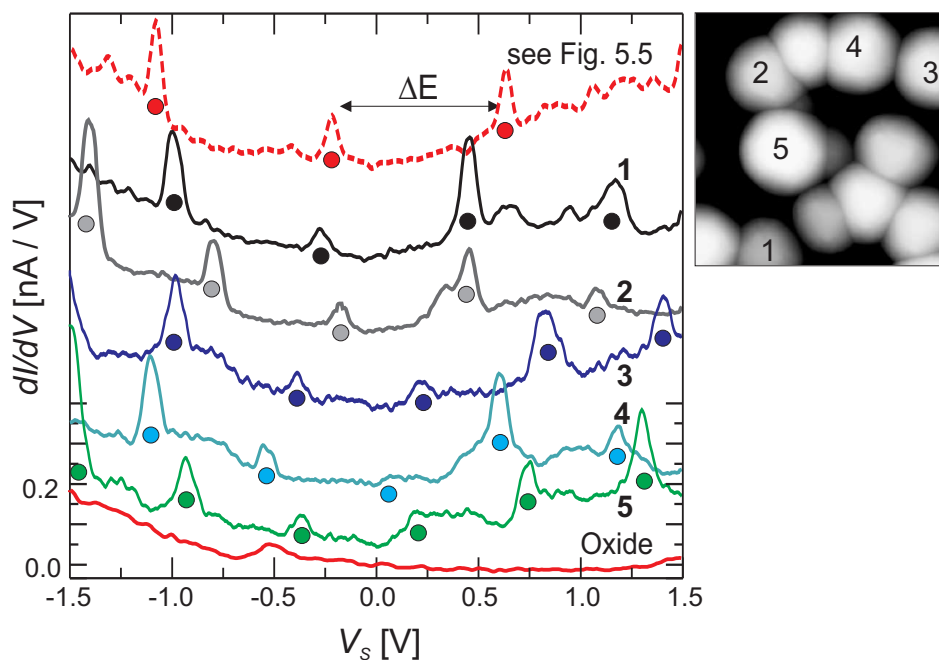


Figure 5.2: Conductance spectra of Ag particles on the alumina film on NiAl(110) and of the bare oxide, taken at $V_s = 1.5$ V, $I_t = 1.0$ nA. Equidistant dI/dV peaks in the clusters are marked by circles. The topmost spectrum refers to the set of dI/dV maps shown in Fig. 5.4. The Ag clusters under examination are shown in the constant current STM image on the right (image size: $500 \text{ \AA} \times 500 \text{ \AA}$).

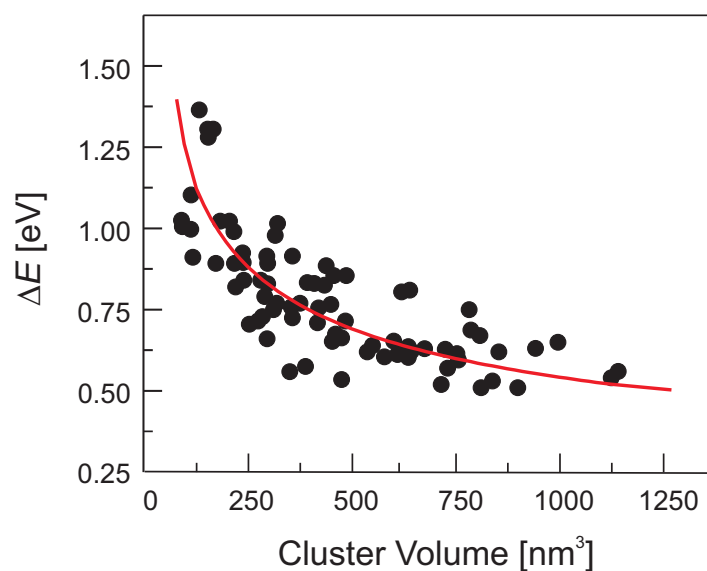


Figure 5.3: Energy separation ΔE of measured dI/dV peaks versus cluster volume V for Ag particles on the alumina film on NiAl(110). The solid line is a least square fit of the data to $\Delta E \propto V^{-\alpha}$ with $\alpha \sim 0.3$.

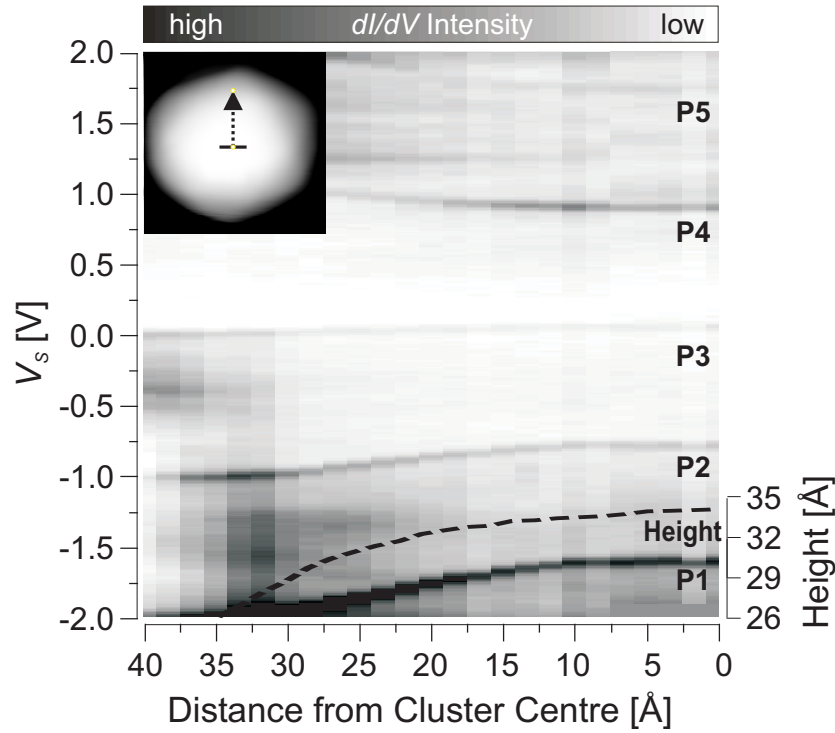


Figure 5.4: Series of 25 dI/dV spectra taken along a line across a Ag cluster on the alumina film on NiAl(110) with $V_s = -1.5$ V, $I_t = 0.1$ nA. The spectra are plotted as a series of vertical lines, yielding a 2D representation of the energy levels as a function of position on the cluster surface. Tip positions are shown in the inset. Five dI/dV peaks P1-P5 can be identified, which shift to larger energies when the tip moves out of the cluster center. The broken line indicates the cluster height at tip positions in the dI/dV series.

identified. They shift to higher absolute energies and enlarge their mutual separation when moving the tip toward the cluster edge. The dispersion disappears for states close to E_F , and becomes larger with increasing distance from E_F . While the magnitude of spectral shifts is independent of the polarity, resonances above and below the Fermi level shift in opposite direction. The faint line between P4 and P5 shows no energy dispersion and is not equidistant to neighboring levels. The respective dI/dV peak is most likely caused by the electronic structure of the tip. The cluster height for the tip positions in the spectral series has been added to Fig. 5.4.

The level shifts with increasing distance from the cluster center were reproduced in dI/dV images, mapping the differential conductance over the cluster surface at a fixed bias value. Characteristic conductance maps for a Ag cluster on the alumina film are shown in Fig. 5.5. The associated dI/dV spectrum taken in the cluster center is presented in Fig. 5.2, uppermost curve. The dI/dV images are dominated by a ring of enhanced conductance, which originates from the resonance peak at -1.05 V in the dI/dV spectrum. The ring emerges in the cluster center at this energy position

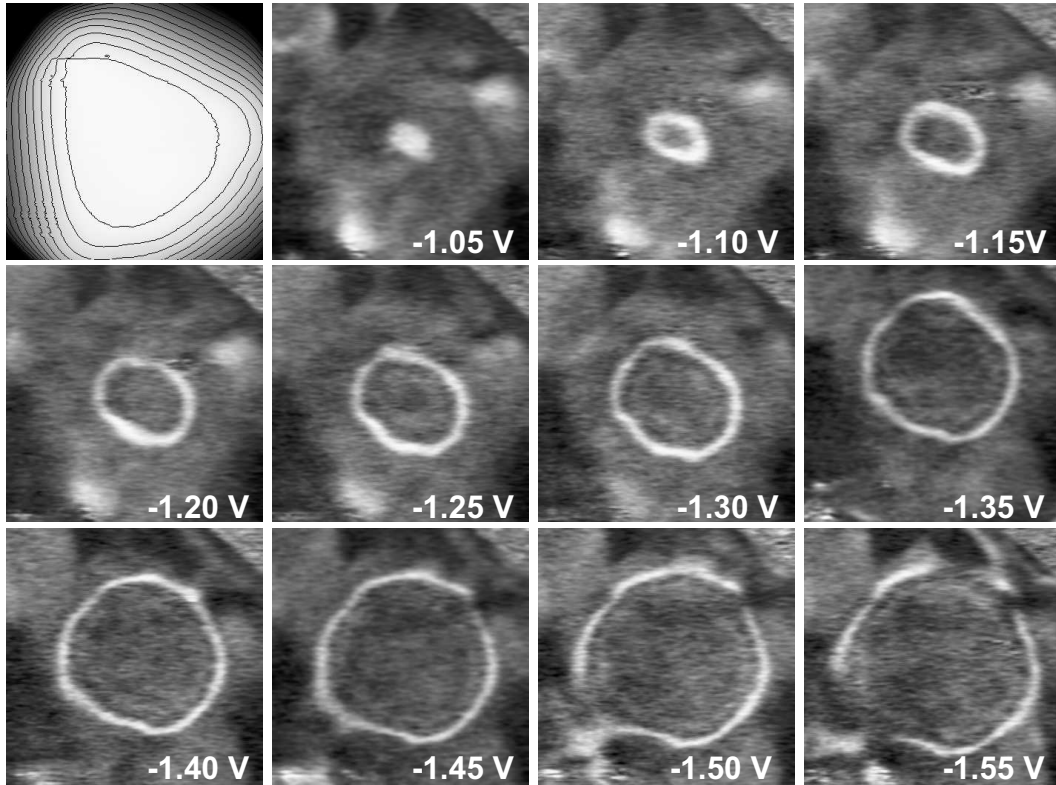


Figure 5.5: Constant current (upper left panel) and dI/dV images of a Ag cluster on the alumina film recorded at the indicated sample bias (image size: $75 \text{ \AA} \times 75 \text{ \AA}$, $I_t = 0.1 \text{ nA}$). Contour lines are separated by 4 \AA . The corresponding dI/dV spectrum taken in the cluster center is shown in Fig. 5.2, uppermost curve. The dI/dV maps exhibit a ring of enhanced conductance, which originates from the resonance at -1.05 V and expands for increasingly negative sample bias.

and grows in diameter with increasing negative sample bias. When the ring diameter becomes comparable to the cluster size, it disappears from the dI/dV images. A similar ring system develops from the dI/dV resonance at -0.20 V and also expands for higher negative voltage. Rings originating from positive dI/dV peaks follow the opposite trend, i.e. they increase in diameter with increasing positive sample bias. The occurrence of rings of enhanced conductance directly reflects the hemispherical cluster shape, where distinct dI/dV resonances appear at the same energy on circles around the cluster center. Obviously, the expansion of dI/dV rings with increasing sample bias is directly connected to shifts of the respective peak in spectra taken more and more outside the cluster center.

So far, dI/dV spectra revealed a series of discrete conductance peaks, which shift dependent on the location of the tip with respect to the cluster center. Often, peak positions depend also on the setpoint, i.e. the sample bias and the tunneling current determining the tip-sample distance. To check, whether such an influence is present

here, dI/dV spectra were recorded for different sample bias. The two diagrams of Fig. 5.6 show each a series dI/dV spectra, where the sample bias was varied between 0.75 and 2.0 V to stabilize the tip before switching off the feedback loop. The spectra in the upper diagram were obtained in the cluster center, while the spectra of the lower diagram were recorded at the cluster edge. In either case, the peaks shift to higher energies with increasing sample bias, i.e. with increasing tip-sample distance. Also the shape of the spectra varies: the conductance shows a gap around $V_s = 0$ for $V_s = 0.75$ V, which gradually vanishes for higher bias voltages.

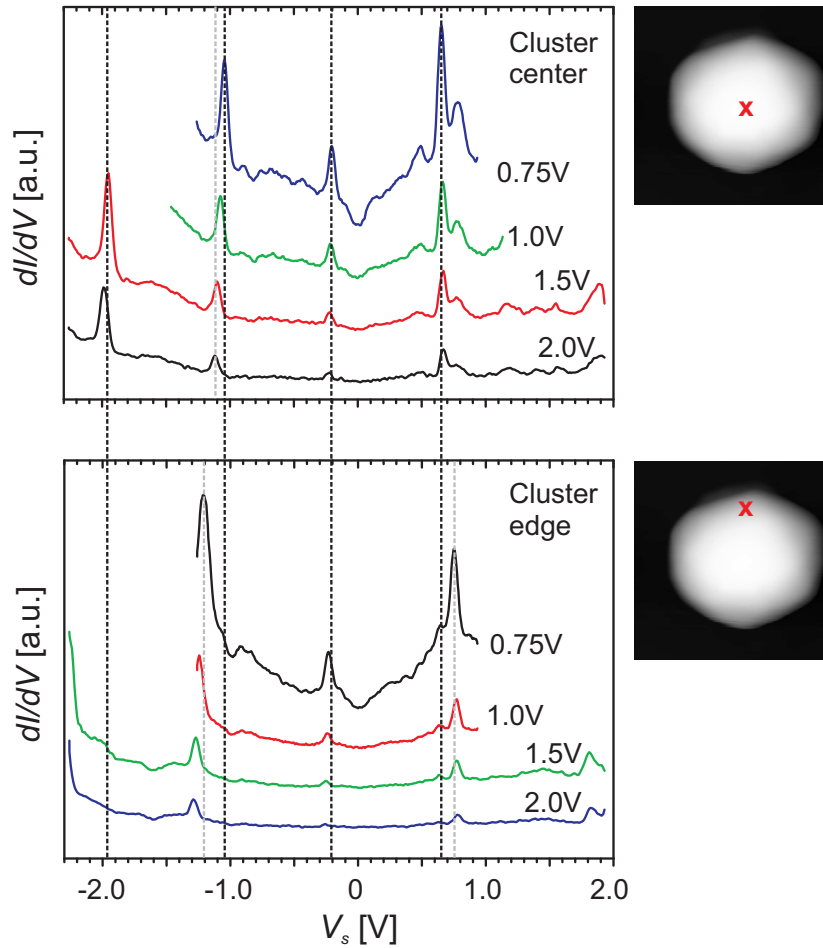


Figure 5.6: dI/dV spectra of a Ag cluster with a diameter of about 85 Å on alumina/NiAl(110). The upper diagram shows spectra, which were recorded above the cluster center, while the tip was positioned above the edge of the cluster in the lower diagram. The sample bias used as setpoint was varied in each diagram. In both cases, this led to a shift of the discrete conductance peaks to higher energies with increasing sample bias (increasing distance).

5.2.2 Palladium Clusters

The studies on Pd clusters are not as detailed as for Ag and aim to provide data for a qualitative rather than a quantitative comparison.

Nucleation and Cluster Shape

Palladium clusters were deposited as described in Section 2.5.4, whereby size and coverage could be adjusted by varying the evaporation conditions (flux, sample temperature, deposited amount of Pd). Clusters investigated here had typically heights h_c between 5 and 15 Å and diameters d_c (surface area at the cluster bottom) of 30 to 80 Å, whereby diameters were corrected as described in Section 2.1.5. The dependence of the diameter-to-height ratio d_c/h_c on the cluster size has been investigated in detail in [169]. According to these studies, the ratio d_c/h_c increases with the cluster size, i.e. small clusters grow preferentially in height, while the growth in width becomes more important for clusters with a height of $h_c \geq 15$ Å. In general, Pd clusters are flatter than Ag clusters. Furthermore, they exhibit ordered top facets (Fig. 5.7 b-d) with hexagonal symmetry. Atomically resolved images revealed a growth in [111] direction [169]. Palladium nucleates preferentially on APDB, as shown in the STM image Fig. 5.7 (a). At the indicated sample bias, APDB appear as bright lines. The nucleation density of Pd clusters is higher than that of Ag clusters, indicating a larger adhesion of the former with the alumina surface.

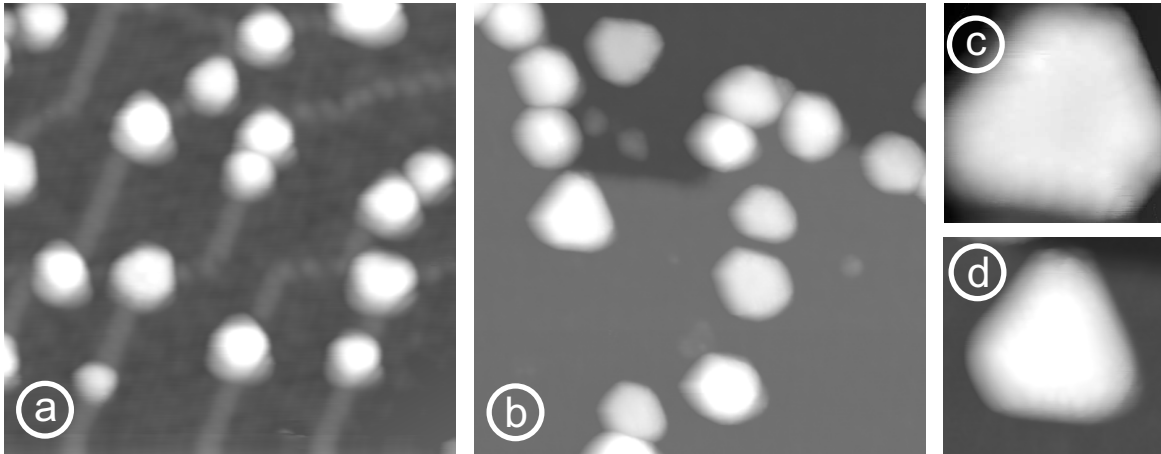


Figure 5.7: STM images of Pd clusters on a thin alumina film on NiAl(110). The slightly blurred cluster shape is due to the tip. (a) Pd nucleates preferentially at APDB, which appear as bright lines at $V_s = 3.0$ V (430×430 Å, 0.9 nA). (b-d) At smaller sample bias, the hexagonal cluster shape is resolved. Image parameters: (b) 390×390 Å, 0.45 V, 0.5 nA; (c-d) 86×86 Å, 0.3 V, 0.5 nA.

Tunneling Spectra

The electronic properties of Pd clusters were investigated by STS. Typical spectra are shown in Fig. 5.8 (b-d) for three differently sized clusters (A–C), whereby the sample bias (setpoint) was varied between 0.5 V and 1.5 V in each of the diagrams (b-d). Conductance spectra of Pd clusters on alumina/NiAl exhibit regions of almost zero conductance around the sample Fermi level. The width of the gap scales inversely with the cluster size, i.e. smaller clusters have larger gaps. The intensity of the gaps diminishes for increasing setpoint bias, and this feature is almost washed out for $|V_s| \geq 1.5$ V.

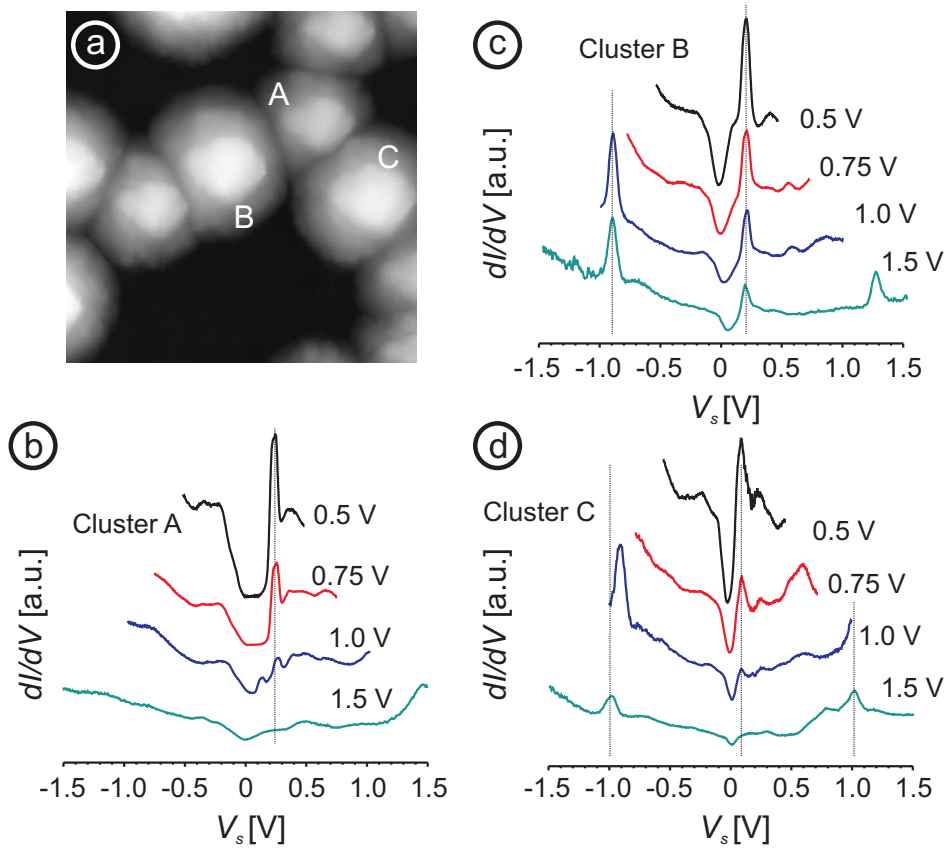


Figure 5.8: (a) STM image ($300 \text{ \AA} \times 300 \text{ \AA}$) of Pd clusters on the alumina film on NiAl(110), recorded at $V_s = 1$ V, $I_t = 1$ nA. (b-d) Conductance spectra taken on top of the clusters B, C, and D, whereby the tip was stabilized at the indicated sample bias. The electronic properties of the tip were checked by STS on the oxide and on oxide defects (APDB).

Beside a gap, dI/dV spectra of Pd clusters show sharp peaks, whereby the number of peaks in the investigated bias range depends on the cluster size. Smaller clusters (such as A) exhibit usually only one resonance close to the Fermi level for $-1.5 \text{ V} \leq V_s \leq 1.5 \text{ V}$, while larger clusters (such as B and C) are characterized by a set of equidistant

peaks. The energy separation between adjacent peaks ranges from 0.8 to 1.2 eV (in the investigated bias range) and scales inversely with the cluster size. As for Ag clusters, a setpoint-dependent peak shift is observed for Pd clusters: resonances shift to higher absolute energy with increasing bias, whereby this effect is most pronounced for energy levels far away from $V_s = 0$.

5.3 Interpretation

The investigation of Pd and Ag clusters on alumina/NiAl(110) by STS revealed a number of similarities for both metals, notably the presence of a gap around the sample Fermi level and a set of distinct dI/dV resonances with equidistant energy separation. The gap width and its intensity with respect to the dI/dV peaks differs slightly for Ag and Pd. However, general trends were found to be similar for both cluster types, such as the setpoint-dependent peak shift. Therefore, it can be assumed that the origin of the STS signature is similar for Pd and Ag.

A gap in conductance can be connected with a Coulomb blockade, and such interpretation would also be in line with the observation of equidistant peaks. However, the latter phenomenon might also be due to a different effect, namely the quantization of intrinsic electronic levels. To address this question, both possibilities (Coulomb blockade and quantization) are discussed in detail in the following, whereby the consistence with respect to all experimental observations is checked in either case.

5.3.1 Coulomb Blockade

Equidistant dI/dV peaks have been earlier measured for metal particles located between two tunneling junctions, the vacuum barrier and an insulating spacer between cluster and support [173, 179]. Electron transport through a double barrier is hindered by the Coulomb repulsion between tunneling electrons and residual charge on the center electrode. Only electrons with an energy exceeding the charging energy can overcome the barrier and contribute to the tunneling current. As discussed in Section 2.2.4, conductance spectra in the Coulomb regime exhibit therefore a gap around $V_s = 0$ and/or a set of equidistant peaks, whereby each peak corresponds to an increase of the cluster charge by one elementary charge. In the present case, the preconditions for the occurrence of a Coulomb blockade are fulfilled, since the tunneling junction contains two barriers: the vacuum separating tip and Ag cluster, and the oxide layer separating Ag cluster and NiAl.

Estimation of the Parameters C_j , R_j

To elucidate whether Coulomb repulsion provides a good explanation of the experimental results, dI/dV spectra are simulated using Eqn. (2.14). Here, four variables (C_1 , C_2 , R_1 and R_2) characterizing the two tunneling barriers have to be fitted (Fig. 2.5), whereby certain estimates can be made on the basis of previous observations. The overall resistance of the tunneling junction, $R_\Sigma = R_1 + R_2$, is known for the setpoint (V_s/I_t), where $R_\Sigma = V_s/I_t$. A typical setpoint condition is ($V_s = 1.5$ V, $I_t = 1$ nA), yielding $R_\Sigma \approx 1.5$ G Ω . Furthermore, the ratio R_1/R_2 can be estimated according to:

$$\frac{R_1}{R_2} = \frac{\epsilon_r/d}{\epsilon_{vac}/z} = \frac{\epsilon_r \cdot z}{d} \quad (5.1)$$

where d is the thickness of the alumina film (5 Å), z the tip-sample distance and ϵ_{vac} , ϵ_r the dielectric constants of the vacuum and the oxide film, respectively. The tip-sample distance ranges roughly from 4 to 8 Å depending on the setpoint. The dielectric constant of the oxide film is not known, but can be approximated by $\epsilon_r = 10$, the value of bulk alumina [179]. STM experiments investigating bipolar tunneling through adsorbates on alumina/NiAl(110) confirm this estimate [45]. According to these considerations, the ratio R_1/R_2 should lay in the range between 8 : 1 and 16 : 1 for larger and shorter tip-sample separations, respectively.

Hanna and Tinkham assume in their model that the double barrier junction can be understood as a series of two capacitors (see Section 2.2.4 and [122]). To calculate the capacitances, the shape of the electrodes has to be known, which is especially difficult for the tip–vacuum–cluster junction, since neither the shape nor the size of the tip can be easily determined. In the following, it is assumed that each barrier can be modeled by a plate capacitor, i.e. that each electrode is planar. Supposing furthermore, that the top facet of the cluster has a larger surface area than the tip, the capacitances C_1 and C_2 can be approximated by:

$$C_1 = \epsilon_0 \cdot \frac{A_t}{z} \quad , \quad (5.2)$$

$$C_2 = \epsilon_0 \cdot \epsilon_r \cdot \frac{A_b}{d} \quad , \quad (5.3)$$

where A_t and A_b are the (planar) surface areas of the metal cluster. In the following, C_2 will be approximated for Ag and Pd clusters. As mentioned before, most Ag clusters have round bottom and top “facets”, i.e. $A_b = \pi/4 \cdot d_b^2$ and $A_t = \pi/4 \cdot d_t^2$. This provides estimates for C_2 , which are summarized in Table 5.1 for different cluster diameters.

For Pd clusters, different surface areas have to be considered because of the hexagonal symmetry of the top and bottom facets. Table 5.2 lists calculated capacitances

	d_b [Å]	20	40	60	80	100	120
Round shape	C_2 [aF]	0.6	2.2	5.0	8.9	13.9	20.0

Table 5.1: Calculated capacitances C_2 dependent on the diameter d_b of the bottom facet of the Ag cluster. The system is modeled by a plate capacitor, where the two electrodes (NiAl and Ag cluster) are separated by a 5 Å thick alumina film (dielectric). The cluster is supposed to have circular shape.

C_2 for typical cluster diameters, assuming that the bottom facet has either the shape of a regular triangle ($A = 1/\sqrt{3} \cdot d^2$, top) or that of a hexagon ($A = \sqrt{3}/2 \cdot d^2$, bottom).

	d_b [Å]	30	40	50	60	70	80
Triangular shape	C_2 [aF]	0.9	1.6	2.5	3.7	5.0	6.5
Hexagonal shape	C_2 [aF]	1.4	2.5	3.8	5.5	7.5	9.8

Table 5.2: Calculated capacitances C_2 dependent on the diameter d of the bottom facet of a Pd cluster, assuming the same model for the capacitor as in Table 5.1. The cluster are supposed to have triangular (top) and hexagonal (bottom) shape, respectively.

The vacuum barrier (C_1) is more difficult to approximate, since neither the tip shape nor the exact tip-sample distance are known. However, it can be supposed that C_1 is significantly smaller than C_2 because of the smaller dielectric constant of the vacuum ($\epsilon_{vac} = 1$) and because the upper facet areas of the clusters are smaller than those at the bottom. Because of the different growth of Ag and Pd clusters, the ratio C_1/C_2 is expected to be larger for Pd than for Ag, whereby C_1 should roughly be in the range of some 0.01 aF or 0.1 aF. As discussed for C_2 , the capacitance C_1 will also increase with the cluster size because of the growing surface area of the top facet.

Simulation of Conductance Spectra

The estimates provided thus far can serve as starting conditions to fit experimental dI/dV spectra of Ag and Pd clusters. To evaluate the quality of the simulations, it has then to be checked if (i) all spectral features can be reproduced assuming a Coulomb blockade and if (ii) the determined parameters are in agreement with the estimates provided above.

(i) Figure 5.9 shows experimental and simulated spectra of a Ag cluster ($d_b \approx 85$ Å) on alumina / NiAl(110). The experimental data correspond to those spectra of Fig. 5.6, where the tip was stabilized above the cluster center at -0.75 V (spectrum I) and 2.0 V (spectrum II), respectively. Spectrum I exhibits both a set of equidistant peaks with a peak-to-peak separation of $\Delta V = 0.85$ V as well as a small dip in the conductance around the sample Fermi level with a width ΔV_0 of 0.10 V. The gap width is mainly

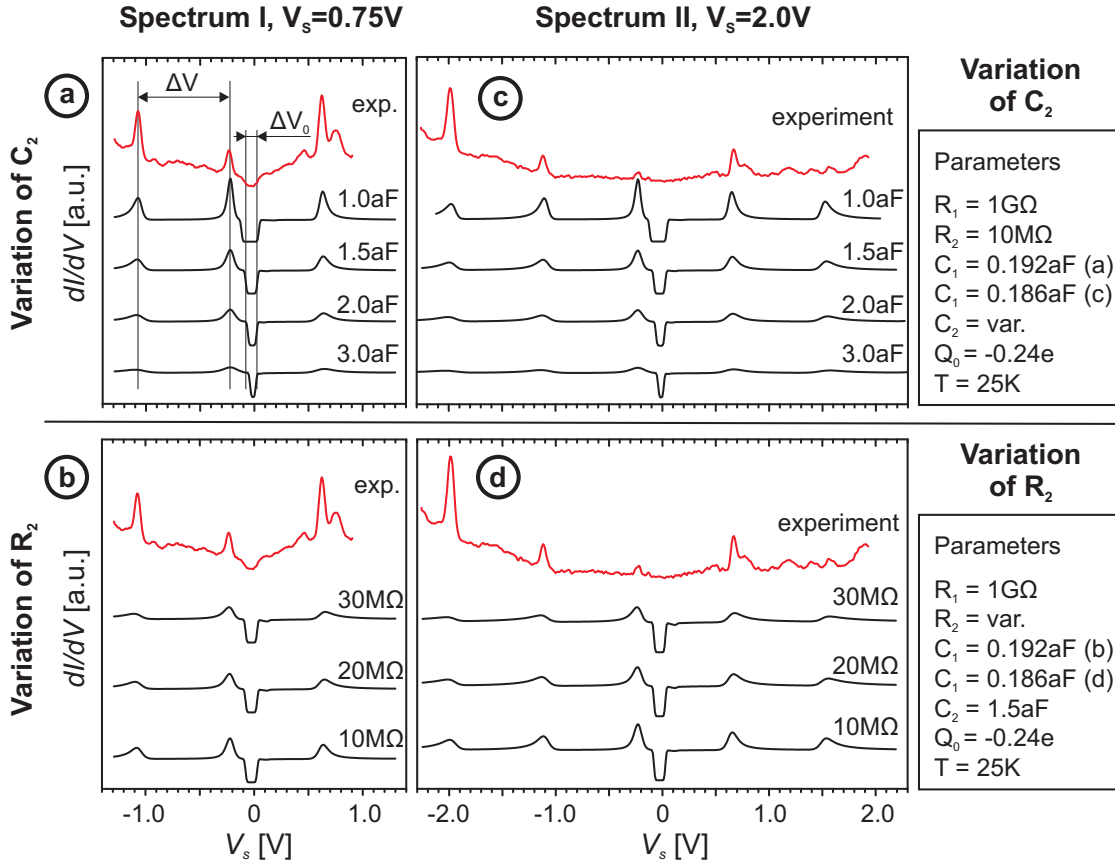


Figure 5.9: Experimental and simulated dI/dV spectra of a Ag cluster with a diameter of about 85 \AA on alumina / NiAl(110). The measured spectra correspond to those data of Fig. 5.6, where the tip was stabilized above the cluster center at -0.75 V (spectrum I) and 2.0 V (spectrum II), respectively. The simulation was performed using Eqn. (2.14), whereby C_2 (a-b) and R_2 (c-d) have been varied for an otherwise fixed parameter set.

determined by the larger of the two capacitances (C_2) and can be approximated by $\Delta V_0 \approx e/C_2$. This dependence is visualized in Fig. 5.9 (a), where C_2 is varied between 1.0 and 3.0 aF . Increasing C_2 , leads to a decrease of the gap width. The best fit to the experimental spectrum is obtained for $C_2 = 1.5 \text{ aF}$. In order to determine C_1 , the peak-to-peak separation ΔV has to be regarded. The latter is governed by the smaller capacitance according to $\Delta V \approx e/C_1$. This provides $C_1 = 0.186 \text{ aF}$. So far, the ratio R_1/R_2 was chosen larger ($100:1$) than estimated above ($8:1$ to $16:1$). To investigate the influence of this parameter, spectra have been simulated for R_1/R_2 between $100:1$ to $33:1$. As can be referred from Fig. 5.9 (b), smaller ratios have no influence on neither the peak positions nor the gap width. However, the relative intensity between peaks and gap diminishes significantly.

Spectrum II (higher setpoint voltage, Fig. 5.9 c) shows also a series of equidistant

peaks, however with slightly larger peak-to-peak separation, $\Delta V = 0.87$ V, than spectrum I. A gap around $V_s = 0$ is not observed. Calculated spectra (Fig. 5.9 c-d) can account for the increased ΔV by reducing the capacitance C_1 slightly (from 0.192 aF to 0.186 aF). This procedure seems to be reasonable, because the increase of the sample bias leads to a larger tip-sample separation and thus to a decrease of C_1 and an increase of R_1 . The influence of each factor, C_1 and R_1 , can be simulated, as shown in Fig. 5.10 for a comparable set of parameters. While a decrease of C_1 by 4–16% results in an

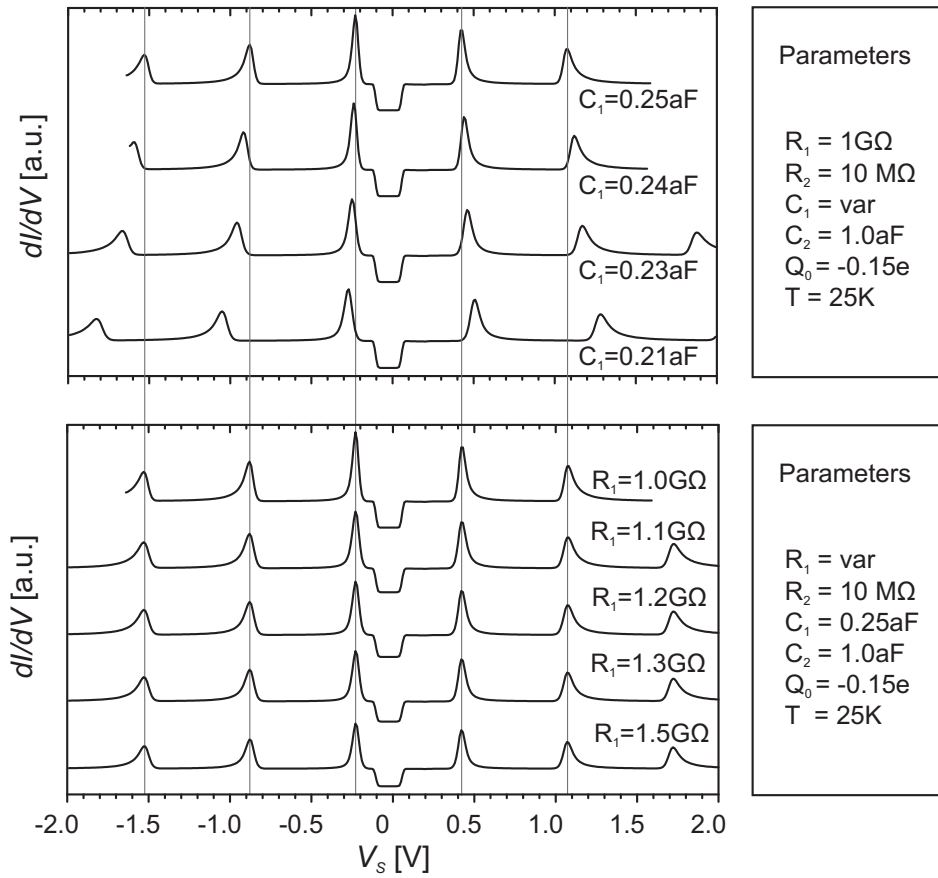


Figure 5.10: Calculated dI/dV spectra (see Eqn. 2.14) of metal clusters on a thin alumina film, whereby the increase of the tip-sample distance is simulated. The capacitance C_1 is varied in the upper diagram, the resistance R_1 in the lower one. In reality, both parameters change simultaneously. The separated variation of C_1 , R_1 is meant to evaluate the influence of either parameter on the energy separation between adjacent peaks, ΔV .

increase of ΔV by 7–20%, an increase of R_1 by 10–50% has almost no influence on ΔV . Thus, the increase of ΔV with larger sample bias would be in line with an interpretation of discrete dI/dV levels arising from Coulomb blockade effects. In contrast, the disappearance of a Coulomb gap for larger V_s cannot be reproduced by reasonable changes in the parameter set used to simulate spectrum I. This might be due to an

assumption made in the applied model, which is not met experimentally, namely that R_j remain constant during spectra acquisition. In reality, the resistance increases dramatically with decreasing bias during a spectral run, due to the exponential tunneling characteristics. As a result, the tunneling current strongly reduces in vicinity of E_F , and spectral features (peaks or gaps) become invisible in dI/dV spectra. This effect is most pronounced for larger V_s . Thus, the spectra of Ag clusters might exhibit a Coulomb gap even for larger V_s (> 1 V) but with an intensity, which is too small to be detected.

The results demonstrate, that simulations based on Coulomb blockade effects reproduce well the features observed in dI/dV spectra on Ag clusters on alumina / NiAl(110) if the parameters R_j , C_j are chosen as follows: $C_1 = 0.2-0.3$ aF, $C_2 = 1.0-3.0$ aF, $R_1/R_2 \approx 100 : 1$. Conductance spectra on Pd clusters can also be fitted, as shown for an example in Fig. 5.11. Usually, R_j , C_j are in the following range: $C_1 = 0.1-0.2$ aF, $C_2 = 0.6-2.0$ aF, $R_1/R_2 \approx 100 : 1$. C_1 might even have values below 0.1 aF for smaller clusters, however this could not be derived from the spectra because of the limited energy range, prohibiting the determination of ΔV .

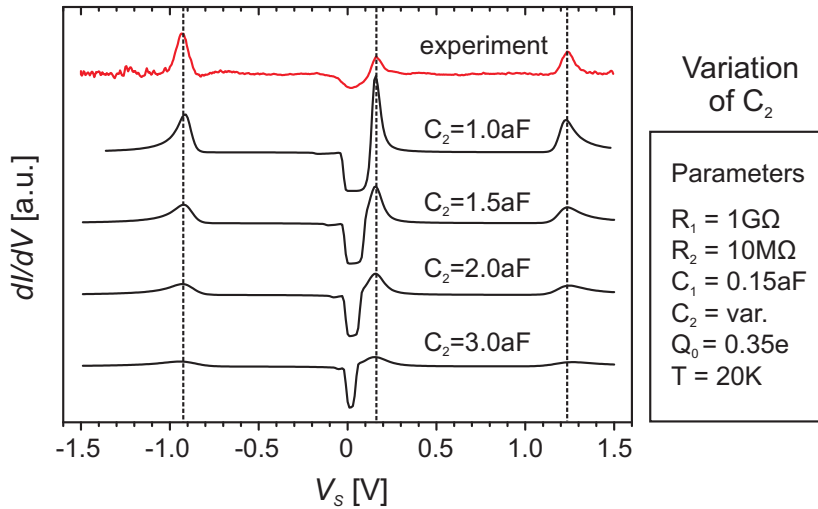


Figure 5.11: Measured (top) and calculated dI/dV spectra of a Pd cluster. The baseline of the measured spectrum was corrected, the original data are shown in Fig. 5.8 (b). The parameters of the simulated spectra were kept constant except from C_2 which was varied between 1.0 and 3.0 aF.

Comparison Between Estimated and Fitted Data

A comparison between estimated and fitted parameters reveals a good agreement for C_1 , and the general size of R_1 and R_2 for both Ag and Pd clusters. However, C_2 is too small by one order of magnitude in either case, and the ratio R_1/R_2 appears to be too

large by a factor of 5–10. As can be referred from the simulated spectra in Fig. 5.9, the ratio R_1/R_2 is mainly responsible for the relative intensity of the gap with respect to the peaks. Considering the effect of decreasing intensity of spectral features close to the Fermi level, i.e. at energies far from the setpoint eV_s , larger ratios R_1/R_2 should agree well with the observations. The deviation in C_2 , on the other hand, is more difficult to understand, though comparable capacitances (0.1–2 aF) have also been determined in various other STM experiments on double barrier junctions, where the dielectric was a thin oxide film or an alkanethiol [123, 174, 175, 180].

Another point, which has to be considered, is the energy separation ΔE between discrete dI/dV peaks. Experimentally, the following dependence was observed: $\Delta E \propto V^{-0.3}$, with V being the cluster volume (Fig. 5.3). Thus, ΔE should depend on the cluster height, h , as $\Delta E \propto 1/h$. However, this dependence cannot be easily derived from the Coulomb blockade model. It was shown above, that $\Delta E \approx e^2/C_1$ for the estimated values of C_j , R_j . With Eqn. (5.2) one obtains $\Delta E \approx e^2 z/\epsilon_0 A_t$, suggesting $\Delta E \propto 1/d_t^2$ (where d_t is the diameter of the top facet). This seems to be in contradiction to the experimental observations. However, as discussed above, the capacitance C_1 of the tip–vacuum–cluster junction is difficult to estimate because of several unknown parameters. Therefore, the calculated values provide only estimates of the real capacitances, but they are not suited to derive a quantitative description for ΔE . In summary, the Coulomb blockade model is not necessarily in contradiction with the observed dependence of ΔE on the cluster height, but it does not provide an explanation, neither.

Dispersion of dI/dV peaks in Ag Clusters

The last point to elucidate the applicability of the Coulomb blockade model concerns the observation of a spatial peak dispersion in series of dI/dV spectra over Ag clusters (Fig. 5.4) and in conductance images (Fig. 5.5). The experiments revealed a shift of conductance peaks away from the Fermi level, when the tip was moved from the cluster center to the edge. As discussed above, such a peak shift to higher absolute energies would be obtained for decreasing R_1 and decreasing C_1 , whereby a stronger effect is expected for latter case (Fig. 5.10). C_1 depends mainly on the tip-cluster distance d and on the projected "overlap" area A of the two facing electrodes (tip and cluster). While d remains constant, A might indeed change dependent on the position of the tip with respect to the cluster. This is shown schematically in Fig. 5.12, where the tip is supposed to be terminated by a planar surface. This simplification is justified, since the resolution ability of the tip is determined by the presence of a small microtip consisting of a few atoms, which has no large influence on the capacitance C_1 of the vacuum barrier. When the tip is moved away from the cluster center, the projected

”overlap“ area A between tip and cluster decreases, and hence does the capacitance C_1 . Thus, Coulomb blockade can explain the spatial peak dispersion observed for dI/dV spectra taken across the Ag clusters.

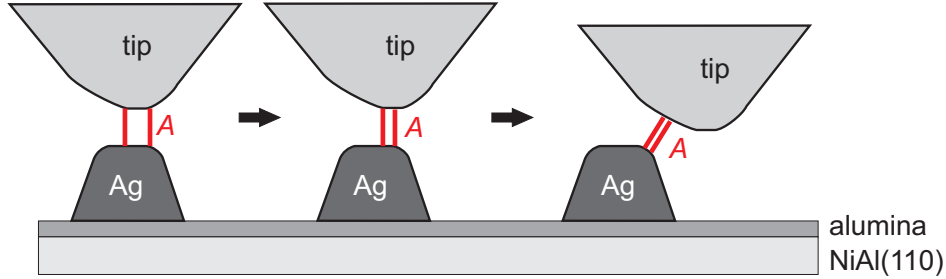


Figure 5.12: Schematic of the tunneling junction, showing the projected ”overlap“ surface area A between tip and Ag cluster dependent on the tip position.

To sum up these considerations, Coulomb blockade effects might provide a good explanation for the experimental observations. However, the determined capacitance C_2 of the vacuum barrier appears to be too small by about one order of magnitude, representing the weak point of the model. Therefore, a second explanation is discussed in the following.

5.3.2 Quantization Along the Cluster Height

The conductance spectra might also reflect the intrinsic LDOS of Ag particles, affected by the quantization of electronic states in the spatially confined system [181]. The presence of discrete electronic levels would lead to sharp peaks in dI/dV spectra similar to those observed here. Quantized surface states have been earlier observed on the top facet of Ag and Au particles on HOPG using STS [111, 171, 172]. These resonances start at an energy close to the onset of the unconfined surface band (-65 mV for Ag(111)) and are not equidistant in energy. The observation of peaks with constant energy separation over a much wider bias range prohibits a similar interpretation for the present data.

Approximately equidistant LDOS levels have been detected by photoelectron spectroscopy and STS for Ag films on GaAs and HOPG [182, 183] and Pb films on Cu(111) [184]. The level separation showed a decrease with increasing film thickness, which was attributed to a quantization of electronic states perpendicular to the film surface. Peak separations measured for Ag particles on the alumina film on NiAl(110) cover a similar range and would also be consistent with quantization effects along the particle height. In such a case, the discretization would be truly one-dimensional and electron confinement in planes parallel to the cluster-oxide interface would be of minor

importance. In a simple particle-in-a-box model, peak separations scale with the dimensionality of the confined system $\Delta E \sim V^{-\alpha}$ [185]. For quantization in a 3D system the scaling factor α is 1, it becomes 2/3 in a 2D and 1/3 in a 1D system. Fitting the correlation between experimental peak separation and cluster volume yields a scaling factor α of roughly 0.3, suggesting a discretization of electronic states along the cluster height (Fig. 5.3). A 1D particle-in-a-box model can also be used to provide a crude estimation of the expected energy gaps between the levels. Electronic states in a 1D quantum well with infinite walls are given by $E_n = E_0 + \frac{\hbar^2}{2m_{\text{eff}}} \left(\frac{\pi n}{l}\right)^2$. To approach the experimental situation, typical cluster heights were chosen for the well length l , and E_0 was taken to match the onset of the bulk Ag *sp* band at -5.5 eV [88]. The calculated level energies as a function of cluster height are shown in Fig. 5.13. The parabolic

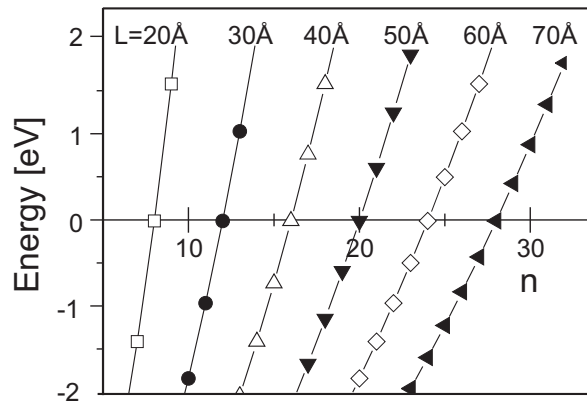


Figure 5.13: Calculated level energies for a particle-in-a-box with box lengths L comparable to real cluster heights.

dispersion is nearly washed out for states with high quantum numbers n , and peaks appear to be equidistant close to the Fermi level. Only this situation (large n) matches the experimental observations, and calculated peak-to-peak separations then cover the same energy range as the measured splittings. However, the simplicity of the model prohibits any quantitative description of the electron confinement in the cluster, as it neglects the finite depth of the potential, phase shifts at the cluster-vacuum and cluster-oxide interfaces and the curvature of the cluster top facet.

Spatial confinement in planes parallel to the surface should also lead to a quantization of electronic states. The level splitting would scale with the inverse area of the 2D planes and is expected to be much smaller than along the cluster height. On the flat top facets of Au particles on HOPG, a quantized surface state has indeed been identified by STS [111, 172]. For Ag particles on the alumina film, a corresponding dI/dV signature was not detected, which might be due the strongly curved cluster surface, but also due to a growth direction deviating from Ag[111].

Spatial Dispersion of the Electronic Levels

Spatially resolved dI/dV spectra of Ag particles revealed a shift of the LDOS resonances to higher energies and an increase of their mutual separation, when moving the tip away from the cluster center. Several approaches are possible to explain this behavior in the picture of electron confinement in oxide-supported Ag clusters. The effect would in principle be consistent with an enhanced electron quantization at positions of reduced cluster height (Fig. 5.13) [185]. However, several arguments are in conflict with such an interpretation. The examined particles have sizes in the range of the Ag Fermi wavelength and represent quantum-mechanical units with constant level energies throughout their diameter [146]. The observed shifts have opposite signs for peaks at positive and negative sample bias and disappear for states at the Fermi level. Using the picture of a height-dependent electron quantization in the cluster, the reversed dispersion of electronic states requires a switching from electron- to hole-like effective masses at the Fermi level. Such an assumption is not justified by experimental evidence and could not be observed in comparable systems before. More severely, the observed level dispersion should depend on the cluster size with larger shifts occurring in smaller particles due to the lower quantum numbers involved. However, no unambiguous dependence of the level shifts on the cluster volume could be derived from the experimental data.

A plausible explanation for the observed behavior, which is in general agreement with the interpretation of the peaks as due to discrete electronic levels, can be found by considering the influence of the tip-induced electric field on the cluster electronic system. In conductance spectra taken with disabled feedback loop, the tip electric field directly scales with the sample bias. Resonances at higher energies are affected by stronger fields and show larger shifts compared to states at the Fermi level. Furthermore, states at positive and negative polarity feel reverse field directions and disperse in opposite manner, as observed in the experiment. The spatial shift of level energies can be understood in terms of a decreasing tip-oxide distance when moving the tip from the center to outer parts of the Ag particles. Above the cluster center, the tip-oxide distance is maximal and the tip electric field is efficiently screened at the Ag surface. The applied sample bias drops mostly in the vacuum barrier between tip and cluster and the effective cluster potential is only weakly affected by the presence of the tip (Fig. 5.14 a). As the tip moves down the cluster, the influence of the electric field on the alumina support increases. The small screening efficiency of the oxide surface leads to a considerable penetration of the field and initiates a band bending in direction of the field gradient [88]. A fraction of the sample bias now drops inside the oxide film, reducing the apparent potential at the cluster surface (Fig. 5.14 b). An electronic state, which was detected at a voltage V_0 in the cluster center, cannot be

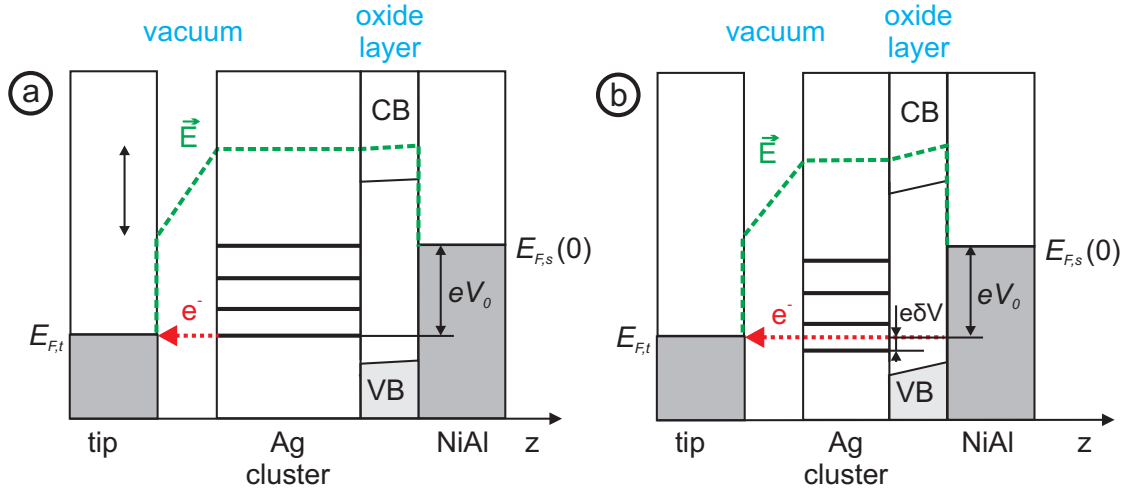


Figure 5.14: Potential diagram for a tunneling junction containing tip, vacuum barrier, Ag cluster, alumina film and NiAl support. (a) sketches tunneling into the cluster center and (b) into its outer parts. The broken line indicates the electron potential across the tunneling junction. Whereas the sample bias drops mostly in the vacuum barrier in (a), it partly penetrates into the oxide film in (b). Energy levels of the cluster in (b) are therefore detected at a higher sample bias ($V_0 + \delta V$) than in (a).

reached at the cluster edge. An additional voltage δV has to be applied to compensate for the voltage drop in the oxide film and the cluster resonance is measured at higher absolute energies. This shift of the resonance condition with decreasing cluster height in combination with the radial cluster symmetry would also explain the occurrence of rings of enhanced conductance, which expand on the cluster surface with increasing sample bias.

Following this model, tip-induced shifts of the cluster levels should exclusively depend on the tip-oxide distance [28]. A correlation between level dispersion and tip height was indeed observed in spectral series taken on the Ag particles (Fig. 5.5). However, the tip height is not the only factor controlling the peak shifts, and rings of enhanced conductance do not perfectly correspond to contour lines of the cluster height. This discrepancy might be caused by the non-local character of the tip-induced electric field, which influences the cluster potential in a wide area. Especially for relatively blunt tips and clusters with close neighbors, the spatial pattern induced by the LDOS peaks can be distorted to almost arbitrarily shapes on the cluster surface.

The maximum bending of the oxide bands and the corresponding peak shifts depend on the static dielectric constant ϵ_r of the alumina layer. Taking the bulk ϵ_r of approximately 10 and a similar thickness for vacuum gap and oxide film (5 Å), 10% of the applied voltage drops in the alumina layer [179]. For a peak position at -1.5 V, the maximum shift would be in the order of -0.15 V, which agrees well with experimental values. As the dielectric properties of the ultra-thin alumina layer might be different

from the bulk material, real shifts of the LDOS levels could be even larger.

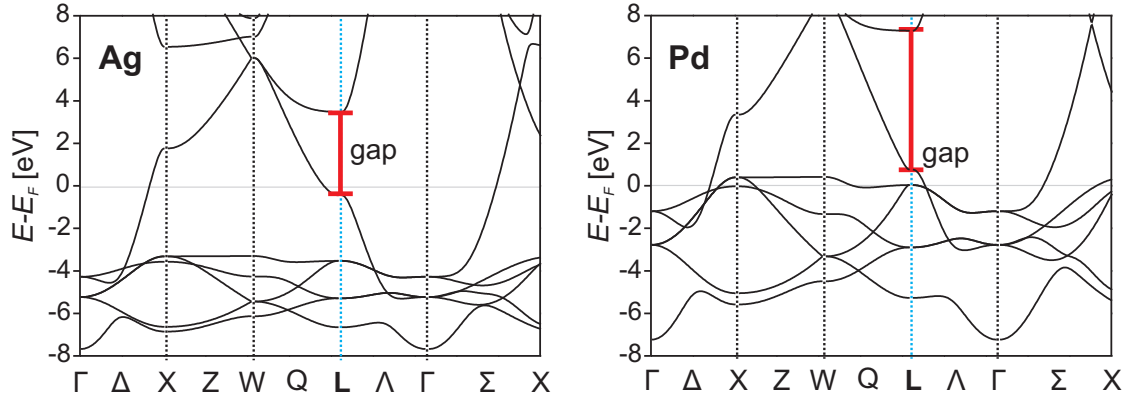


Figure 5.15: Band structure of Ag and Pd, which both exhibit an L band gap [185].

So far, it could be shown that a quantization of electronic states along the cluster height is, in general, suited to explain the presence of discrete dI/dV peaks in conductance spectra of Ag clusters on the alumina film. However, two facts seem to contradict a height quantization. First, increased tip-sample distances during spectroscopy (i.e. larger V_s or smaller I_t) should lead to smaller peak-to-peak separations, because the electric field between tip and cluster and hence the band bending become smaller. This is not observed experimentally (see Fig. 5.6). Secondly, if Ag clusters grow with $[111]$ orientation (like Au), a level quantization along the cluster height would mostly affect the electron band in $\Gamma - L$ direction of the Brillouin zone, which has a pronounced gap in bulk silver (Fig. 5.15) [181, 184]. In the present experiment on Ag particles, the energy levels cross the Fermi level without evidence of this gap. The obvious suppression of the forbidden zone for electronic states is rather unexpected for particles of this size and could be an indication for a growth direction different from Ag $[111]$, where bulk bands show no gap at the Fermi level. However, the hexagonal or triangular cluster shapes, which are sometimes observed, point to the development of (111) -oriented clusters, putting a serious drawback to the quantization model.

Palladium shows also a gap at the L point of the Brillouin zone, though the onset is at higher energy (Fig. 5.15). The growth direction of Pd is known to be $[111]$ from atomically resolved STM images [169]. Nevertheless, peaks in conductance spectra of Pd clusters do also cross this forbidden zone. This indicates that a quantization of electronic states should not be the origin of the equidistant dI/dV peaks.

To sum up the arguments for the second interpretation, a quantization of discrete electronic states along the cluster height can conclusively explain some of the experimental observation, notably the presence of equidistant dI/dV peaks. However, the expected evolution of peak-to-peak separations dependent on the setpoint (V_s) is not

in line with experimental results. Other points, such as the observation of electronic levels within the L -band gap cast further doubts in this interpretation, though the growth direction is not exactly known, and thus this concern does not represent a clear contradiction.

5.3.3 Comparison

The previous sections have shown that both Coulomb blockade and 1D quantization of electronic states can explain many of the experimental observations. However, a Coulomb blockade regime appears to be more likely for several reasons. First, simulated conductance spectra in this regime could reproduce both gaps and equidistant peaks with the correct size, using reasonable input values for C_1 , R_1 , and R_2 . Only the capacitance of the oxide barrier (C_2) had to be chosen roughly one order of magnitude smaller than expected. Secondly, the interpretation of equidistant peaks as due to a height quantization of discrete electronic levels is only reasonable when assuming the growth direction of the clusters to be different from [111]. This is not the case for Pd and unlikely for Ag. Thirdly, Coulomb blockade effects can easily explain peak shifts to higher absolute energies with increasing setpoint bias. Here, an interpretation based on the discrete electronic level model fails. Finally, peak shifts dependent on the distance from the cluster center can be understood in terms of a Coulomb blockade variation caused by a change of the capacitance characterizing the vacuum barrier (C_1). This observation cannot be explained by a height quantization in a straightforward manner, however electric-field effects might result in comparable peak shifts, allowing for a plausible explanation, too.

5.4 Summary

Silver and Pd clusters grown on alumina / NiAl(110) have been studied by STM, STS and conductance imaging. Typical cluster diameters were in the range of 60–120 Å for Ag and 30–80 Å for Pd. Conductance spectra revealed a series of equidistant peaks for both Ag and Pd clusters with typical peak-to-peak separations ΔV of 0.56–0.85 V for Ag and $\Delta V \geq 1.0$ V for Pd. Additionally, spectra exhibit often a region with almost zero conductance around the sample Fermi level, whereby gap widths are slightly larger for Pd than for Ag. The appearance of spectral features (equidistant peaks and gaps) depends on the setpoint bias used to adjust the tip-sample distance before spectra acquisition. Gaps are less pronounced at higher sample bias and almost vanish for $V_s > 1.5$ V, while peak separations become larger with increasing sample bias, whereby the shift is larger for peaks further away from the sample Fermi level. A peak shift to

larger absolute energies is also observed when the tip is moved from the cluster center to the cluster edge, as determined by spatially resolved STS and conductance imaging.

Two effects have been considered to explain the experimental findings: Coulomb blockade effects and quantization of discrete electronic states, inherent to the metal cluster. The advantages and disadvantages of either theory are discussed in detail. Accordingly, Coulomb blockade appears to be more likely as origin of the mentioned spectral features.

Chapter 6

Conclusions and Outlook

The aim of this thesis was the detailed characterization of a thin alumina film on NiAl(110) using low-temperature STM and STS. Three main questions should be addressed: (i) the geometric and electronic structure of the film and its defects, (ii) the adsorption behavior of the alumina film toward single metal atoms and (iii) the size dependence of electronic and electron transport properties of deposited metal clusters.

First, atomically resolved STM images of alumina / NiAl(110) have been obtained, which show features with different symmetry. The assignment of these structures to distinct atomic oxide layers was possible only after computational determination of the structure [1]. Accordingly, three of the four oxide layers can be directly imaged by STM. Further studies addressed the geometric and electronic properties of antiphase domain boundaries (APDB), which are regularly appearing line defects in the alumina film. Here, STM and STS data together with DFT calculations [136] provide a conclusive picture how changes in the film geometry and stoichiometry influence its electronic properties. These studies haven shown that APDB are oxygen-deficient structures which induce three unoccupied defect levels in the alumina band gap.

Second, the adsorption behavior of the alumina film toward single Au atoms has been investigated at 5 K. STM images revealed the presence of monomers, dimers and small, sometimes one-dimensional clusters on the oxide surface after evaporation of Au atoms. The detailed analysis of their geometric properties strongly indicates that the NiAl substrate is involved in the binding of Au atoms on the oxide film. This represents a remarkable result, since it is usually supposed that wide-gap thin insulating films, as the investigated alumina film on NiAl(110), behave chemically like the corresponding bulk oxides. So far, only computational studies for Au atoms on MgO / Mo(100) indicate that there might be exceptions, especially for adatoms with high electron affinity. The present studies provide first experimental evidence for such deviating adsorption behavior of thin insulating films on metal supports.

Third, Ag and Pd clusters were deposited onto alumina/NiAl(110) and investigated by STM and STS. Conductance spectra exhibited a series of sharp peaks with equidistant energy separation that decreases with increasing cluster size. Some spectra revealed furthermore a dip in conductance around the sample Fermi level. A detailed analysis of these features suggests, that they do not represent intrinsic cluster properties but result from the specific electron transport properties across the tunneling junction: since the metal clusters are separated from the STM electrodes (tip and NiAl) by two barriers with different height (vacuum and oxide layer), charge can accumulate on the cluster in a quantized fashion. The energy separation between the dI/dV peaks corresponds hence to the charging energy of the cluster. This phenomenon is known as Coulomb staircase, the observed dip in conductance as Coulomb gap. These results are especially important for further studies on oxide-supported metal clusters. A main goal is, for instance, the investigation of vibrational modes of molecular adsorbates on the various adsorption sites of a cluster (e.g. different facets or edges etc.). For that purpose, inelastic tunneling spectroscopy (IETS) is a promising STM method, as it provides vibrational information of single, adsorbed molecules by detection of the second derivative of the tunneling current [53]. However, if already the first derivative (i.e. the differential conductance investigated here) is strongly structured due to Coulomb blockade effects, it will be difficult to distinguish relevant features in the second derivative.

The characterization of the alumina film performed within the scope of this thesis includes several predictions which can be tested in further studies. Investigations on the bare alumina film might comprise adsorption studies on different molecules with high oxidation strength, e.g. O_2 or NO. They are supposed to have high affinity to APDB, where adsorption should occur preferentially at the position with large O–O separation, as identified in STM images and computationally. Apart from the determination of the adsorption site, it might be possible to characterize the adsorbed molecules by IETS. Furthermore, the unexpected adsorption behavior of the alumina film toward Au adatoms suggests a number of experiments. First, the Au-alumina interaction should be further studied, e.g. by co-adsorption of molecules, such as CO, which is often used for this purpose [161, 186, 187]. Vibrational spectra of the CO-Au complex (obtained by IETS) might resolve the question of the charge state of Au: a much weaker interaction (reflected in a higher CO stretching frequency and a lower energy of the CO hindered rotation) is expected for $Au^{\delta+}$ than for $Au^{\delta-}$ species. However, one has to bear in mind that such IETS studies would provide information on the charge state of the Au(CO) complex, which does not necessarily correspond to the initial charge state of the Au adatom, as shown by recent infrared spectroscopy measurements of Au(CO) on 20 ML thick MgO(100) films [187]. To check the influence of the adsorbed

molecule, other gases (e.g. NO) might be adsorbed as reference. Apart from studies dedicated to the Au–alumina interaction, initial investigations on other metal adatoms (Pd [149], Ag) should be extended to determine whether the participation of the NiAl in the adatom binding is a special feature of Au or more universal. Indications for such mechanism would be the adsorption site, adatom distances in dimers, the occurrence of preferential dimer orientations and eventually the existence of chains. Such studies are essential to evaluate the suitability of thin oxide films as model for bulk oxides.

Bibliography

- [1] G. Kresse, M. Schmid, E. Napetschnig, M. Shishkin, L. Köhler, and P. Varga. Structure of the ultrathin aluminum oxide film on NiAl(110). *Science*, 308:1440, 2005.
- [2] G. Ertl, H. Knözinger, and J. Weitkamp, editors. *Handbook of Heterogeneous Catalysis*. VCH, Weinheim, 1997.
- [3] G. Ertl and P. Rau. Chemisorption and catalytic reactions of oxygen and carbon monoxide on a palladium (110) surface. *Surf. Sci.*, 15:443, 1969.
- [4] D. R. Kahn, E. E. Petersen, and G. A. Somorjai. Hydrogenolysis of cyclopropane on a platinum stepped single crystal at atmospheric pressure. *J. Catal.*, 34:294, 1974.
- [5] K. Christmann, G. Ertl, and T. Pignet. Adsorption of hydrogen on a Pt(111) surface. *Surf. Sci.*, 54:365, 1976.
- [6] D. W. Goodman, R. D. Kelley, T. E. Madey, and J. T. Yates. Kinetics of the hydrogenation of CO over a single-crystal nickel-catalyst. *J. Catal.*, 63:226, 1980.
- [7] G. Ertl. Primary steps in catalytic synthesis of ammonia. *J. Vac. Sci. Technol. A*, 1:1247, 1983.
- [8] R. Schlögl. Catalytic synthesis of ammonia – a “never-ending story”? *Angew. Chem. Int. Ed.*, 42:2004, 2003.
- [9] M. S. Chen, D. Kumar, C.-W. Yi, and D. W. Goodman. The promotional effect of gold in catalysis by palladium-gold. *Science*, 310:291, 2005.
- [10] U. Diebold. The surface science of titanium dioxide. *Surf. Sci. Rep.*, 48:53, 2003.
- [11] R. Schaub, E. Wahlström, A. Rønnau, E. Lægsgaard, I. Stensgaard, and F. Besenbacher. Oxygen-mediated diffusion of oxygen vacancies on the TiO₂(110) surface. *Science*, 299:377, 2003.

- [12] F. Esch, S. Fabris, L. Zhou, T. Montini, C. Africh, P. Fornasiero, G. Comelli, and R. Rosei. Electron localization determines defect formation on ceria substrates. *Science*, 309:752, 2005.
- [13] H. Kuhlenbeck, C. Xu, B. Dillmann, M. Hassel, B. Adam, D. Ehrlich, S. Wohlrab, H.-J. Freund, U. A. Ditzinger, H. Neddermeyer, M. Neuber, and M. Neumann. Adsorption and reaction on oxide surfaces - CO and CO₂ on Cr₂O₃(111). *Ber. Bunsenges. Phys. Chem.*, 96:15, 1992.
- [14] Z. Li, Q. Guo, and P. J. Møller. Electronic properties of Cu clusters and islands and their reaction with O₂ on SnO₂(110) surface. *Zeitschr. Phys. D*, 40:550, 1997.
- [15] R. P. Furstenuau and M. A. Langell. Adsorption of ethylene on stoichiometric and reduced NiO(100). *Surf. Sci.*, 159:108, 1985.
- [16] A. Ludviksson, K. H. Ernst, R. Zhang, and C. T. Campbell. The chemisorption of CO on Cu films on ZnO(0001)-O. *J. Catal.*, 141:380, 1993.
- [17] Q. Guo and P. J. Møller. CO and residual H adsorption on Cu/ZnO(10 $\bar{1}$ 0). *Appl. Surf. Sci.*, 115:39, 1997.
- [18] O. Dulub, M. Batzill, and U. Diebold. Growth of copper on single crystalline ZnO: surface study of a model catalyst. *Topics Catal.*, 36:65, 2005.
- [19] H.-J. Freund, H. Kuhlenbeck, and V. Staemmler. Oxide surfaces. *Rep. Prog. Phys.*, 59:283, 1996.
- [20] C. T. Campbell. Ultrathin metal films and particles on oxide surfaces: structural, electronic and chemisorptive properties. *Surf. Sci. Rep.*, 27:1, 1997.
- [21] M. Bäumer and H.-J. Freund. Metal deposits on well-ordered oxide films. *Prog. Surf. Sci.*, 61:127, 1999.
- [22] H.-J. Freund. Clusters and islands on oxides: from catalysis via electronics and magnetism to optics. *Surf. Sci.*, 500:271, 2002.
- [23] A. K. Santra and D. W. Goodman. Oxide-supported metal clusters: models for heterogeneous catalysts. *J. Phys.: Condens. Matter*, 14:R31, 2002.
- [24] R. M. Jaeger, H. Kuhlenbeck, H.-J. Freund, M. Wuttig, W. Hoffmann, R. Franchy, and H. Ibach. Formation of a well-ordered aluminum oxide overlayer by oxidation of NiAl(110). *Surf. Sci.*, 259:235, 1991.

- [25] S. Andersson, P. A. Brühwiler, A. Sandell, M. Frank, J. Libuda, A. Giertz, B. Brena, A. J. Maxwell, M. Bäumer, H.-J. Freund, and N. Mårtensson. Metal-oxide interaction for metal clusters on a metal-supported thin alumina film. *Surf. Sci.*, 442:L964, 1999.
- [26] R. H. French, R. L. Coble, R. V. Kasowski, and F. S. Ohuchi. Vacuum ultraviolet, photoemission and theoretical studies of the electronic structure of Al_2O_3 up to 1000°C . *Physica B+C*, 150:47, 1988.
- [27] E. T. Arakawa and M. W. Williams. Optical properties of aluminum oxide in vacuum ultraviolet. *J. Phys. Chem. Solids*, 29:735, 1968.
- [28] S. Schintke and W. D. Schneider. Insulators at the ultrathin limit: electronic structure studied by scanning tunnelling microscopy and scanning tunnelling spectroscopy. *J. Phys.: Condens. Matter*, 16:R49, 2004.
- [29] I. Costina and R. Franchy. Band gap of amorphous and well-ordered Al_2O_3 on $\text{Ni}_3\text{Al}(100)$. *Appl. Phys. Lett.*, 78:4139, 2001.
- [30] J. S. Corneille, J.-W. He, and D. W. Goodman. XPS characterization of ultra-thin MgO films on a $\text{Mo}(100)$ surface. *Surf. Sci.*, 306:269, 1994.
- [31] S. Altieri, L. H. Tjeng, and G. A. Sawatzky. Electronic structure and chemical reactivity of oxide-metal interfaces: $\text{MgO}(100)/\text{Ag}(100)$. *Phys. Rev. B*, 61:16948, 2000.
- [32] J.-W. He, X. Xu, J. S. Corneille, and D. W. Goodman. X-ray photoelectron spectroscopic characterization of ultra-thin silicon oxide films on a $\text{Mo}(100)$ surface. *Surf. Sci.*, 279:119, 1992.
- [33] J. Weissenrieder, S. Kaya, J.-L. Lu, H.-J. Gao, S. Shaikhutdinov, H.-J. Freund, M. Sierka, T. K. Todorova, and J. Sauer. Atomic structure of a thin silica film on a $\text{Mo}(112)$ substrate: a two-dimensional network of SiO_4 tetrahedra. *Phys. Rev. Lett.*, 95:076103, 2005.
- [34] A. B. Boffa, H. C. Galloway, P. W. Jacobs, J. J. Benítez, J. D. Batteas, M. Salmeron, A. T. Bell, and G. A. Somorjai. The growth and structure of titanium oxide films on $\text{Pt}(111)$ investigated by LEED, XPS, ISS, and STM. *Surf. Sci.*, 326:80, 1995.
- [35] G. S. Herman, M. C. Gallagher, S. A. Joyce, and C. H. F. Peden. Structure of epitaxial thin TiO_2 films on $\text{W}(110)$ as studied by low energy electron diffraction and scanning tunneling microscopy. *J. Vac. Sci. Technol. B*, 14:1126, 1996.

- [36] N. Ernst, B. Duncombe, G. Bozdech, M. Naschitzki, and H.-J. Freund. Field ion microscopy of platinum adatoms deposited on a thin Al₂O₃ film on NiAl(110). *Ultramicroscopy*, 79:231, 1999.
- [37] M. Bäumer, M. Frank, M. Heemeier, R. Kühnemuth, S. Stempel, and H.-J. Freund. Nucleation and growth of transition metals on a thin alumina film. *Surf. Sci.*, 454:957, 2000.
- [38] T. Schalow, M. Laurin, B. Brandt, S. Schauer mann, S. Guimond, H. Kühlenbeck, D. E. Starr, S. K. Shaikhutdinov, J. Libuda, and H.-J. Freund. Oxygen storage at the metal/oxide interface of catalyst nanoparticles. *Angew. Chem. Int. Ed.*, 44:7601, 2005.
- [39] V. Johánek, M. Laurin, A. W. Grant, B. Kasemo, C. R. Henry, and J. Libuda. Fluctuations and bistabilities on catalyst nanoparticles. *Science*, 304:1639, 2004.
- [40] J. Libuda and H.-J. Freund. Molecular beam experiments on model catalysts. *Surf. Sci. Rep.*, 57:157, 2005.
- [41] G. A. Somorjai. Modern surface science and surface technologies: an introduction. *Chem. Rev.*, 96:1223, 1996.
- [42] M. J. Green, B. J. Barner, and R. M. Corn. Real-time sampling electronics for double modulation experiments with Fourier transform infrared spectrometers. *Rev. Sci. Instrum.*, 62:1426, 1991.
- [43] E. Ozensoy, D. C. Meier, and D. W. Goodman. Polarization modulation infrared reflection absorption spectroscopy at elevated pressures: CO adsorption on Pd(111) at atmospheric pressures. *J. Phys. Chem. B*, 106:9367, 2002.
- [44] M. Borasio, O. R. de la Fuente, G. Rupprechter, and H.-J. Freund. In situ studies of methanol decomposition and oxidation on Pd(111) by PM-IRAS and XPS spectroscopy. *J. Phys. Chem. B*, 109:17791, 2005.
- [45] S. W. Wu, G. V. Nazin, X. Chen, X. H. Qiu, and W. Ho. Control of relative tunneling rates in single molecule bipolar electron transport. *Phys. Rev. Lett.*, 93:236802, 2004.
- [46] G. V. Nazin, X. H. Qiu, and W. Ho. Vibrational spectroscopy of individual doping centers in a monolayer organic crystal. *J. Chem. Phys.*, 122:181105, 2005.
- [47] X. H. Qiu, G. V. Nazin, and W. Ho. Vibrationally resolved fluorescence excited with submolecular precision. *Science*, 299:542, 2003.

- [48] A. J. Heinrich, J. A. Gupta, C. P. Lutz, and D. M. Eigler. Single-atom spin-flip spectroscopy. *Science*, 306:466, 2004.
- [49] S. Schauer mann, V. Johánek, M. Laurin, J. Libuda, and H.-J. Freund. Low temperature decomposition of NO on ordered alumina films. *Chem. Phys. Lett.*, 381:298, 2003.
- [50] G. Pacchioni, L. Giordano, and M. Baistrocchi. Charging of metal atoms on ultrathin MgO/Mo(100) films. *Phys. Rev. Lett.*, 94:226104, 2005.
- [51] G. Binnig, H. Rohrer, Ch. Gerber, and E. Weibel. Surface studies by scanning tunneling microscopy. *Phys. Rev. Lett.*, 49:57, 1982.
- [52] R. M. Feenstra, W. A. Thompson, and A. P. Fein. Real-space observation of π -bonded chains and surface disorder on Si(111)2x1. *Phys. Rev. Lett.*, 56:608, 1986.
- [53] B. C. Stipe, M. A. Rezaei, and W. Ho. Single-molecule vibrational spectroscopy and microscopy. *Science*, 280:1732, 1998.
- [54] J. H. Coombs, J. K. Gimzewski, B. Reihl, J. K. Sass, and R. R. Schlittler. Photon-emission experiments with the scanning tunneling microscope. *J. Microscopy*, 152:325, 1988.
- [55] R. Berndt, R. R. Schlittler, and J. K. Gimzewski. Photon-emission scanning tunneling microscope. *J. Vac. Sci. Technol. B*, 9:573, 1991.
- [56] M. F. Crommie, C. P. Lutz, and D. M. Eigler. Imaging standing waves in a two-dimensional electron gas. *Nature*, 363:524, 1993.
- [57] M. F. Crommie, C.P. Lutz, and D. M. Eigler. Confinement of electrons to quantum corrals on a metal surface. *Science*, 262:218, 1993.
- [58] Ph. Avouris and I.-W. Lyo. Observation of quantum-size effects at room-temperature on metal-surfaces with STM. *Science*, 264:942, 1994.
- [59] J. Li, W.-D. Schneider, R. Berndt, and S. Crampin. Electron confinement to nanoscale Ag islands on Ag(111): a quantitative study. *Phys. Rev. Lett.*, 80:3332, 1998.
- [60] N. Nilus, T. M. Wallis, and W. Ho. Development of one-dimensional band structure in artificial gold chains. *Science*, 297:1853, 2002.

- [61] H. J. Lee and W. Ho. Single-bond formation and characterization with a scanning tunneling microscope. *Science*, 286:1719, 1999.
- [62] J. I. Pascual, J. J. Jackiw, Z. Song, P. S. Weiss, H. Conrad, and H.-P. Rust. Adsorbate-substrate vibrational modes of benzene on Ag(110) resolved with scanning tunneling spectroscopy. *Phys. Rev. Lett.*, 86:1050, 2001.
- [63] J. I. Pascual, N. Lorente, Z. Song, H. Conrad, and H.-P. Rust. Selectivity in vibrationally mediated single-molecule chemistry. *Nature*, 423:525, 2003.
- [64] R. Berndt, J. K. Gimzewski, and P. Johansson. Inelastic tunneling excitation of tip-induced plasmon modes on noble-metal surfaces. *Phys. Rev. Lett.*, 67:3796, 1991.
- [65] N. Niliius, N. Ernst, and H.-J. Freund. Photon emission spectroscopy of individual oxide-supported silver clusters in a scanning tunneling microscope. *Phys. Rev. Lett.*, 84:3994, 2000.
- [66] S. Heinze, M. Bode, A. Kubetzka, O. Pietzsch, X. Nie, S. Blügel, and R. Wiesendanger. Real-space imaging of two-dimensional antiferromagnetism on the atomic scale. *Science*, 288:1805, 2000.
- [67] A. Wachowiak, J. Wiebe, M. Bode, O. Pietzsch, M. Morgenstern, and R. Wiesendanger. Direct observation of internal spin structure of magnetic vortex cores. *Science*, 298:577, 2002.
- [68] A. J. Heinrich, C. P. Lutz, J. A. Gupta, and D. M. Eigler. Molecule cascades. *Science*, 298:1381, 2002.
- [69] E. Wahlström, E. K. Vestergaard, R. Schaub, A. Rønnau, M. Vestergaard, E. Lægsgaard, I. Stensgaard, and F. Besenbacher. Electron transfer-induced dynamics of oxygen molecules on the TiO₂(110) surface. *Science*, 303:511, 2004.
- [70] M. Rossler, P. Geng, and J. Wintterlin. A high-pressure scanning tunneling microscope for studying heterogeneous catalysis. *Rev. Sci. Instrum.*, 76:023705, 2005.
- [71] R. Wiesendanger, editor. *Scanning Probe Microscopy and Spectroscopy: Methods and Applications*. Cambridge University Press, Cambridge, 1994.
- [72] C. J. Chen. *Introduction to Scanning Tunneling Microscopy*. Oxford University Press, New York, Oxford, 1993.

-
- [73] D. Drakova. Theoretical modelling of scanning tunneling microscopy, scanning tunneling spectroscopy and atomic force microscopy. *Rep. Prog. Phys.*, 64:205, 2001.
- [74] J. Bardeen. Tunneling from a many-particle point of view. *Phys. Rev. Lett.*, 6:57, 1961.
- [75] J. Tersoff and D. R. Hamann. Theory and application for the scanning tunneling microscope. *Phys. Rev. Lett.*, 50:1998, 1983.
- [76] J. Tersoff and D. R. Hamann. Theory of the scanning tunneling microscope. *Phys. Rev. B*, 31:805, 1985.
- [77] C. J. Chen. Introduction to scanning tunneling spectroscopy. *J. Vac. Sci. Technol. A*, 6:319, 1988.
- [78] A. Selloni, P. Carnevali, E. Tosatti, and C. D. Chen. Voltage-dependent scanning-tunneling microscopy of a crystal surface: graphite. *Phys. Rev. B*, 31:2602, 1985.
- [79] N. D. Lang. Spectroscopy of single atoms in the scanning tunneling microscope. *Phys. Rev. B*, 34:5947, 1986.
- [80] P. Sautet. Images of adsorbates with the scanning tunneling microscope: theoretical approaches to the contrast mechanism. *Chem. Rev.*, 97:1097, 1997.
- [81] W. Hebenstreit, J. Redinger, Z. Horozova, M. Schmid, R. Podloucky, and P. Varga. Atomic resolution by STM on ultra-thin films of alkali halides: experiment and local density calculations. *Surf. Sci.*, 424:L321, 1999.
- [82] R. H. Fowler and L. Nordheim. Electron emission in intense electric fields. *Proc. R. Soc.*, 119:173, 1928.
- [83] R. S. Becker, J. A. Golovchenko, and B. S. Schwartzentruber. Electron interferometry at crystal surfaces. *Phys. Rev. Lett.*, 55:987, 1985.
- [84] G. Binnig, K. H. Frank, H. Fuchs, N. Garcia, B. Reihl, H. Rohrer, F. Salvan, and A. R. Williams. Tunneling spectroscopy and inverse photoemission: image and field states. *Phys. Rev. Lett.*, 55:991, 1985.
- [85] T. A. Jung, F. J. Himpsel, R. R. Schlittler, and J. K. Gimzewski. *Scanning Probe Microscopy - Analytic Methods (Nano Science and Technology)*, chapter 2. Springer, Berlin, 1998.

- [86] E. D. L. Rienks, N. Nilius, H.-P. Rust, and H.-J. Freund. Surface potential of a polar oxide film: FeO on Pt(111). *Phys. Rev. B*, 71:241404(R), 2005.
- [87] M. R. Castell, S. L. Dudarev, C. Muggelberg, A. P. Sutton, G. A. D. Briggs, and D. T. Goddard. Microscopy of metal oxide surfaces. *Microsc. Microanal.*, 6:324, 2000.
- [88] D. A. Bonnell. Scanning tunneling microscopy and spectroscopy of oxide surfaces. *Prog. Surf. Sci.*, 57:187, 1998.
- [89] Th. Bertrams, A. Brodde, and H. Neddermeyer. Tunneling through an epitaxial oxide film: Al₂O₃ on NiAl(110). *J. Vac. Sci. Technol. B*, 12:2122, 1994.
- [90] Th. Bertrams and H. Neddermeyer. Growth of NiO(100) layers on Ag(100): characterization by scanning tunneling microscopy. *J. Vac. Sci. Technol. B*, 14:1141, 1996.
- [91] S. Schintke, S. Messerli, M. Pivetta, F. Patthey, L. Libioulle, M. Stengel, A. De Vita, and W. D. Schneider. Insulator at the ultrathin limit: MgO on Ag(001). *Phys. Rev. Lett.*, 87:276801, 2001.
- [92] K. Højrup Hansen, T. Worren, E. Lægsgaard, F. Besenbacher, and I. Stensgaard. Bias dependent apparent height of an Al₂O₃ thin film on NiAl(110), and of supported Pd clusters. *Surf. Sci.*, 475:96, 2001.
- [93] V. A. Ukraintsev. Data evaluation technique for electron-tunneling spectroscopy. *Phys. Rev. B*, 53:11176, 1996.
- [94] L. J. Lauhon and W. Ho. Effects of temperature and other experimental variables on single molecule vibrational spectroscopy with the scanning tunneling microscope. *Rev. Sci. Instrum.*, 72:216, 2001.
- [95] A. Wachowiak. *Aufbau einer 300mK-Ultrahochvakuum-Rastertunnelmikroskopie-Anlage mit 14 Tesla Magnet und spinpolarisierte Rastertunnelspektroskopie an ferromagnetischen Fe-Inseln*. PhD thesis, Universität Hamburg, 2003.
- [96] D. Haude. *Rastertunnelspektroskopie auf der InAs(110)-Oberfläche: Untersuchungen an drei-, zwei- und nulldimensionalen Elektronensystemen im Magnetfeld*. PhD thesis, Universität Hamburg, 2000.
- [97] J. Viernow, D. Y. Petrovykh, A. Kirakosian, J.-L. Lin, F. K. Men, M. Henzler, and F. J. Himpsel. Chemical imaging of insulators by STM. *Phys. Rev. B*, 59:10356, 1999.

-
- [98] K. Morgenstern, K.-F. Braun, and K.-H. Rieder. Surface-state depopulation on small Ag(111) terraces. *Phys. Rev. Lett.*, 89:226801, 2002.
- [99] H. Jensen, J. Kröger, R. Berndt, and S. Crampin. Electron dynamics in vacancy islands: scanning tunneling spectroscopy on Ag(111). *Phys. Rev. B*, 71:155417, 2005.
- [100] S. Crampin, H. Jensen, J. Kröger, L. Limot, and R. Berndt. Resonator design for use in scanning tunneling spectroscopy studies of surface electron lifetimes. *Phys. Rev. B*, 72:035443, 2005.
- [101] V. Madhavan, W. Chen, T. Jamneala, M. F. Crommie, and N. S. Wingreen. Tunneling into a single magnetic atom: spectroscopic evidence of the Kondo resonance. *Science*, 280:567, 1998.
- [102] T. Jamneala, V. Madhavan, W. Chen, and M. F. Crommie. Scanning tunneling spectroscopy of transition-metal impurities at the surface of gold. *Phys. Rev. B*, 61:9990, 2000.
- [103] M. F. Crommie, C. P. Lutz, and D. M. Eigler. Spectroscopy of a single adsorbed atom. *Phys. Rev. B*, 48:2851, 1993.
- [104] T. M. Wallis, N. Nilius, and W. Ho. Electronic density oscillations in gold atomic chains assembled atom by atom. *Phys. Rev. Lett.*, 89:236802, 2002.
- [105] N. Nilius, T. M. Wallis, and W. Ho. Localized molecular constraint on electron delocalization in a metallic chain. *Phys. Rev. Lett.*, 90:186102, 2003.
- [106] S. Fölsch, P. Hyldgaard, R. Koch, and K. H. Ploog. Quantum confinement in monatomic Cu chains on Cu(111). *Phys. Rev. Lett.*, 92:056803, 2004.
- [107] G. Mills, B. Wang, W. Ho, and H. Metiu. Electronic states of linear Au clusters supported on metal surfaces: Why are they like those of a particle in a box? *J. Chem. Phys.*, 120:7738, 2004.
- [108] Mats Persson. Computational study of electron states in Au chains on NiAl(110). *Phys. Rev. B*, 70:205420, 2004.
- [109] A. Calzolari, C. Cavazzoni, and M. B. Nardelli. Electronic and transport properties of artificial gold chains. *Phys. Rev. Lett.*, 93:096404, 2004.
- [110] A. Calzolari and M. B. Nardelli. First principles theory of artificial metal chains on NiAl(110) surface. *Phys. Rev. B*, 72:045416, 2005.

-
- [111] H. Hövel and I. Barke. Large noble metal clusters: electron confinement and band structure effects. *New Journal of Physics*, 5:31, 2003.
- [112] J. Repp, G. Meyer, S. M. Stojković, A. Gourdon, and Ch. Joachim. Molecules on insulating films: scanning tunneling microscopy imaging of individual molecular orbitals. *Phys. Rev. Lett.*, 94:026803, 2005.
- [113] G. V. Nazin, C. H. Xi, and W. Ho. Atomic engineering of photon emission with a scanning tunneling microscope. *Phys. Rev. Lett.*, 90:216110, 2003.
- [114] N. A. Pradhan, N. Liu, C. Silien, and W. Ho. Atomic scale conductance induced by single impurity charging. *Phys. Rev. Lett.*, 94:076801, 2005.
- [115] N. Nilius, T. M. Wallis, and W. Ho. Influence of a heterogeneous Al₂O₃ surface on the electronic properties of single Pd atoms. *Phys. Rev. Lett.*, 90:046808, 2003.
- [116] N. Nilius, E. D. L. Rienks, H.-P. Rust, and H.-J. Freund. Self-organization of gold atoms on a polar FeO(111) surface. *Phys. Rev. Lett.*, 95:066101, 2005.
- [117] K. Mullen, E. Ben-Jacob, R. C. Jaklevic, and Z. Schuss. I-V characteristics of coupled ultrasmall-capacitance normal tunnel junctions. *Phys. Rev. B*, 37:98, 1988.
- [118] I. Giaever and H. R. Zeller. Superconductivity of small tin particles measured by tunneling. *Phys. Rev. Lett.*, 20:1504, 1968.
- [119] J. Lambe and R. C. Jaklevic. Charge-quantization studies using a tunnel capacitor. *Phys. Rev. Lett.*, 22:1371, 1969.
- [120] K. Mullen, E. Ben-Jacob, and S. Ruggiero. Charging effects in coupled superconducting tunnel junctions and their implications for tunneling measurements of high-T_c superconductors. *Phys. Rev. B*, 38:R5150, 1988.
- [121] M. Amman, R. Wilkins, E. Ben-Jacob, P. D. Maker, and R. C. Jaklevic. Analytic solution for the current-voltage characteristic of two mesoscopic tunnel junctions coupled in series. *Phys. Rev. B*, 43:1146, 1991.
- [122] A. E. Hanna and M. Tinkham. Variation of the Coulomb staircase in a two-junction system by fractional electron charge. *Phys. Rev. B*, 44:5919, 1991.
- [123] R. Wilkins, E. Ben-Jacob, and R. C. Jaklevic. Scanning-tunneling-microscope observations of Coulomb blockade and oxide polarization in small metal droplets. *Phys. Rev. Lett.*, 63:801, 1989.

- [124] D. V. Averin, A. N. Korotkov, and K. K. Likharev. Theory of single-electron charging of quantum wells and dots. *Phys. Rev. B*, 44:6199, 1991.
- [125] Y. Hasegawa and Ph. Avouris. Direct observation of standing wave formation at surface steps using scanning tunneling spectroscopy. *Phys. Rev. Lett.*, 71:1071, 1993.
- [126] N. Nilius, M. Kulawik, H.-P. Rust, and H.-J. Freund. Defect-induced gap states in Al₂O₃ thin films on NiAl(110). *Phys. Rev. B*, 69:121401, 2004.
- [127] M. Sterrer, M. Heyde, M. Nowicki, N. Nilius, Th. Risse, H.-P. Rust, G. Pacchioni, and H.-J. Freund. Identification of color centers on MgO(001) thin films with scanning tunneling microscopy. *J. Phys. Chem. B*, 110:46, 2006.
- [128] J. Buisset. *Tieftemperatur Rastertunnelmikroskopie - Entwicklung eines hochstabilen Gerätekonzepts zur Untersuchung dynamischer Oberflächenprozesse und zur Analyse und Handhabung einzelner Atome und Moleküle zwischen 4 und 300 Kelvin*. PhD thesis, Technische Universität Berlin, 1996.
- [129] H.-P. Rust, J. Buisset, E. K. Schweizer, and L. Cramer. High precision mechanical approach mechanism for a low temperature scanning tunneling microscope. *Rev. Sci. Instrum.*, 68:129, 1997.
- [130] M. Doering. *Über die Abbildung und Untersuchung der Eigenschaften einzelner Adsorbate auf Metalloberflächen mittels Rastertunnelmikroskopie bei tiefen Temperaturen*. PhD thesis, Freie Universität Berlin, 1998.
- [131] H.-P. Rust, M. Doering, J. I. Pascual, T. P. Pearl, and P. S. Weiss. Temperature control of a liquid helium cooled Eigler-style scanning tunneling microscope. *Rev. Sci. Instrum.*, 72:4393, 2001.
- [132] P. S. Weiss and D. M. Eigler. What is underneath? Moving atoms and molecules to find out. In V. T. Binh, N. Garcia, and K. Dransfeld, editors, *Nanosources and Manipulations of Atoms under High Fields and Temperatures: Applications*, volume 235 of *NATO ASI Series E*. Plenum, New York, 1993.
- [133] M. Kulawik, N. Nilius, H.-P. Rust, and H.-J. Freund. Atomic structure of antiphase domain boundaries of a thin Al₂O₃ film on NiAl(110). *Phys. Rev. Lett.*, 91:256101, 2003.
- [134] J. Libuda, F. Winkelmann, M. Bäumer, H.-J. Freund, Th. Bertrams, H. Neddermeyer, and K. Müller. Structure and defects of an ordered alumina film on NiAl(110). *Surf. Sci.*, 318:61, 1994.

- [135] M. Frank and M. Bäumer. From atoms to crystallites: adsorption on oxide-supported metal particles. *Phys. Chem. Chem. Phys.*, 2:3723, 2000.
- [136] M. Schmid, M. Shishkin, G. Kresse, E. Napetschnik, P. Varga, M. Kulawik, N. Nilius, H.-P. Rust, and H.-J. Freund. Oxygen-deficient line defects in an ultrathin aluminum oxide film. Submitted.
- [137] M. Adelt, S. Nepijko, W. Drachsel, and H.-J. Freund. Size-dependent luminescence of small palladium particles. *Chem. Phys. Lett.*, 291:425, 1998.
- [138] M. Frank. *Vom Atom zum Kristallit – Struktur und Reaktivität oxidgetragener Metallpartikel*. PhD thesis, Humboldt-Universität zu Berlin, 2000.
- [139] M. Frank, R. Kühnemuth, M. Bäumer, and H.-J. Freund. Vibrational spectroscopy of CO adsorbed on supported ultra-small transition metal particles and single metal atoms. *Surf. Sci.*, 454-456:968, 2000.
- [140] F. Winkelmann, S. Wohlrab, J. Libuda, M. Bäumer, D. Cappus, M. Menges, K. Al-Shamery, H. Kuhlenbeck, and H.-J. Freund. Adsorption on oxide surfaces: structure and dynamics. *Surf. Sci.*, 307-309:1148, 1994.
- [141] G. Ceballos, Z. Song, J. I. Pascual, H.-P. Rust, H. Conrad, M. Bäumer, and H.-J. Freund. Structure investigation of the topmost layer of a thin ordered alumina film grown on NiAl(110) by low temperature scanning tunneling microscopy. *Chem. Phys. Lett.*, 359:41, 2002.
- [142] D. R. Jennison and A. Bogicevic. Ultrathin alumina film Al-sublattice structure, metal island nucleation at terrace point defects, and how hydroxylation affects wetting. *Faraday Discuss.*, 114:45, 1999.
- [143] A. Stierle, F. Renner, R. Streitl, H. Dosch, W. Drube, and B. C. Cowie. X-ray diffraction study of the ultrathin Al₂O₃ layer on NiAl(110). *Science*, 303:1652, 2004.
- [144] G. Kresse and J. Furthmüller. Efficiency of ab-initio total energy calculations for metals and semiconductors using a plane-wave basis set. *Comput. Mater. Sci.*, 6:15, 1996.
- [145] J. P. Perdew, J. A. Chevary, S. H. Vosko, K. A. Jackson, M. R. Pederson, D. J. Singh, and C. Fiolhais. Atoms, molecules, solids and surfaces: applications of the generalized gradient approximation for exchange and correlation. *Phys. Rev. B*, 46:6671, 1992.

- [146] C. Kittel. *Introduction to Solid State Physics*. Wiley, New York, 1996.
- [147] G. L. Kellogg. Field ion microscope studies of single-atom surface diffusion and cluster nucleation on metal surfaces. *Surf. Sci. Rep.*, 21:1, 1994.
- [148] Harald Brune. Microscopic view of epitaxial metal growth: nucleation and aggregation. *Surf. Sci. Rep.*, 31:125, 1998.
- [149] N. Nilius, T. M. Wallis, M. Persson, and W. Ho. Distance dependence of the interaction between single gold atoms: Gold dimers on NiAl(110). *Phys. Rev. Lett.*, 90:196103, 2003.
- [150] K. Morgenstern, K.-F. Braun, and K.-H. Rieder. Direct imaging of Cu dimer formation, motion, and interaction with Cu atoms on Ag(111). *Phys. Rev. Lett.*, 93:056102, 2004.
- [151] W. T. Wallace, B. K. Min, and D. W. Goodman. The nucleation, growth, and stability of oxide-supported metal clusters. *Top. Catal.*, 34:17, 2005.
- [152] N. F. Mott. The theory of the formation of protective oxide films on metals.-III. *Trans. Faraday Soc.*, 43:429, 1947.
- [153] A. Bogicevic and D. R. Jennison. Variations in the nature of metal adsorption on ultrathin Al₂O₃ films. *Phys. Rev. Lett.*, 82:4050, 1999.
- [154] N. C. Hernández, J. Graciani, A. Márquez, and J. F. Sanz. Cu, Ag and Au atoms deposited on the α -Al₂O₃(0001) surface: a comparative density functional study. *Surf. Sci.*, 575:189, 2005.
- [155] L. Giordano, M. Baistrocchi, and G. Pacchioni. Bonding of Pd, Ag, and Au atoms on MgO(100) surfaces and MgO/Mo(100) ultra-thin films: a comparative DFT study. *Phys. Rev. B*, 72:115403, 2005.
- [156] A. Cörper, G. Bozdech, N. Ernst, T. Klüner, and H.-J. Freund. Field electron energy spectroscopy of alumina-supported platinum adatoms. *Phys. Stat. Sol. (b)*, 242:2462, 2005.
- [157] J.-M. Antonietti, M. Michalski, U. Heiz, H. Jones, K. H. Lim, N. Rösch, A. Del Vitto, and G. Pacchioni. Optical absorption spectrum of gold atoms deposited on SiO₂ from cavity ringdown spectroscopy. *Phys. Rev. Lett.*, 94:213402, 2005.
- [158] R. C. Weast, editor. *CRC Handbook of Chemistry and Physics*. CRC Pr., Cleveland, Ohio, 55 edition, 1974.

- [159] N. C. Hernández and J. F. Sanz. First principles simulations of Cu and Au deposition on α -Al₂O₃ (0001) surface. *Appl. Surf. Sci.*, 238:228, 2004.
- [160] J. Repp, G. Meyer, F. E. Olsson, and M. Persson. Controlling the charge state of individual gold adatoms. *Science*, 305:493, 2004.
- [161] A. S. Wörz, U. Heiz, F. Cinquini, and G. Pacchioni. Charging of Au atoms on TiO₂ thin films from CO vibrational spectroscopy and DFT calculations. *J. Phys. Chem. B*, 109:18418, 2005.
- [162] B. Yoon, H. Häkkinen, U. Landman, A. S. Wörz, J.-M. Antonietti, S. Abbet, K. Judai, and U. Heiz. Charging effects on bonding and catalyzed oxidation of CO on Au₈ clusters on MgO. *Science*, 307:403, 2005.
- [163] A. Del Vitto, G. Pacchioni, F. Delbeq, and Ph. Sautet. Au atoms and dimers in the MgO(100) surface: a DFT study of nucleation at defects. *J. Phys. Chem. B*, 109:8040, 2005.
- [164] Z.-P. Liu, S. J. Jenkins, and D. A. King. Origin and activity of oxidized gold in water-gas-shift catalysis. *Phys. Rev. Lett.*, 94:196102, 2005.
- [165] G. Butti, M. I. Trioni, and H. Ishida. Electronic properties calculation of MgO thin films adsorbed on semi-infinite Ag(001). *Phys. Rev. B*, 70:195425, 2004.
- [166] L. Giordano, A. Del Vitto, and G. Pacchioni. Au and Pd atoms adsorbed on pure and Ti-doped SiO₂/Mo(112) films. Submitted.
- [167] J. Repp, G. Meyer, S. Paavilainen, F. E. Olsson, and M. Persson. Scanning tunneling spectroscopy of Cl vacancies in NaCl films: strong electron-phonon coupling in double-barrier tunneling junctions. *Phys. Rev. Lett.*, 95:225503, 2005.
- [168] M. Frank, K. Wolter, N. Magg, M. Heemeier, R. Kühnemuth, M. Bäumer, and H.-J. Freund. Phonons of clean and metal-modified oxide films: an infrared and HREELS study. *Surf. Sci.*, 492:270, 2001.
- [169] K. Højrup Hansen, T. Worren, S. Stempel, E. Lægsgaard, M. Bäumer, H.-J. Freund, F. Besenbacher, and I. Stensgaard. Palladium nanocrystals on Al₂O₃: structure and adhesion energy. *Phys. Rev. Lett.*, 83:4120, 1999.
- [170] A. Bettac, L. Köller, V. Rank, and K. H. Meiwes-Broer. Scanning tunneling spectroscopy on deposited platinum clusters. *Surf. Sci.*, 402:475, 1998.

- [171] H. Hövel, B. Grimm, M. Bödecker, K. Fieger, and B. Reihl. Tunneling spectroscopy on silver clusters at $T=5\text{K}$: size dependence and spatial energy shift. *Surf. Sci.*, 463:L603, 2000.
- [172] I. Barke and H. Hövel. Confined Shockley surface states on the (111) facets of gold clusters. *Phys. Rev. Lett.*, 90:166801, 2003.
- [173] J. G. Hou, B. Wang, J. Yang, X. R. Wang, H. Q. Wang, Q. Zhu, and X. Xiao. Nonclassical behavior in the capacitance of a nanojunction. *Phys. Rev. Lett.*, 86:5321, 2001.
- [174] J. G. Hou, B. Wang, J. Yang, W. Lu, Z. Li, H. Wang, D. M. Chen, and Q. Zhu. Disorder and suppression of quantum confinement effects in Pd nanoparticles. *Phys. Rev. Lett.*, 90:246803, 2003.
- [175] N. Oncel, A.-S. Hallback, H. J. W. Zandvliet, E. A. Speets, B. J. Ravoo, D. N. Reinhoudt, and B. Poelsema. Coulomb blockade of small Pd clusters. *J. Chem. Phys.*, 123:044703, 2005.
- [176] M. Valden, X. Lai, and D. W. Goodman. Onset of catalytic activity of gold clusters on titania with the appearance of nonmetallic properties. *Science*, 281:1647, 1998.
- [177] U. Heiz, A. Sanchez, S. Abbet, and W.-D. Schneider. Catalytic oxidation of carbon monoxide on monodispersed platinum clusters: each atom counts. *J. Am. Chem. Soc.*, 121:3214, 1999.
- [178] H. Osman, J. Schmidt, K. Svensson, R. E. Palmer, Y. Shigeta, and J. P. Wilcoxon. STM studies of passivated Au nanocrystals immobilized on a passivated Au(111) surface: ordered arrays and single electron tunnelling. *Chem. Phys. Lett.*, 330:1, 2000.
- [179] J. Fontanella, C. Andeen, and D. Schuele. Low-frequency dielectric constants of α -quartz, sapphire, MgF_2 , and MgO . *J. Appl. Phys.*, 45:2852, 1974.
- [180] B. Wang, H. Wang, H. Li, C. Zeng, J. G. Hou, and X. Xiao. Tunable single-electron tunneling behavior of ligand-stabilized gold particles on self-assembled monolayers. *Phys. Rev. B*, 63:035403, 2000.
- [181] D. A. Evans, M. Alonso, R. Cimino, and K. Horn. Observation of quantum size effects in photoemission from Ag islands on GaAs(110). *Phys. Rev. Lett.*, 70:3483, 1993.

-
- [182] F. Patthey and W.-D. Schneider. Layer-by-layer-resolved quantum-well states in ultrathin silver islands on graphite: a photoemission study. *Phys. Rev. B*, 50:17560, 1994.
- [183] I. B. Altfeder, K. A. Matveev, and D. M. Chen. Electron fringes on a quantum wedge. *Phys. Rev. Lett.*, 78:2815, 1997.
- [184] R. Otero, A. L. Vázquez de Parga, and R. Miranda. Observation of preferred heights in Pb nanoislands: a quantum size effect. *Phys. Rev. B*, 66:115401, 2002.
- [185] D. A. Papaconstantopoulos. *Handbook of Band Structures of Elemental Solids*. Plenum Press, New York, 1986.
- [186] M. Frank, M. Bäumer, R. Kühnemuth, and H.-J. Freund. Metal atoms and particles on oxide supports: probing structure and charge by infrared spectroscopy. *J. Phys. Chem. B*, 105:8569, 2001.
- [187] M. Sterrer, M. Yulikov, Th. Risse, H.-J. Freund, J. Carrasco, F. Illas, C. Di Valentin, L. Giordano, and G. Pacchioni. When the reporter induces the effect: CO on Au₁/MgO(100)/Mo(100). *Angew. Chem.*, Accepted.

Appendix A

List of Abbreviations

nD	-	n -dimensional
f_{mod}	-	Modulation frequency of the lock-in amplifier, which is used for conductance imaging and STS
AFM	-	Atomic force microscopy
Al_i	-	interface aluminum atoms of the thin alumina film on NiAl(110)
Al_s	-	surface aluminum atoms of the thin alumina film on NiAl(110)
APDB	-	Antiphase domain boundary
CB	-	Conduction band
CT	-	Charge transfer
DFT	-	Density functional theory
DOS	-	Density of states
EA	-	Electron affinity
E_F	-	Fermi energy
FWHM	-	Full width at half maximum
HOMO	-	Highest occupied molecular orbital
I_t	-	Tunneling current
IETS	-	Inelastic electron tunneling spectroscopy
LDOS	-	Local density of states
LEED	-	Low energy electron diffraction
LUMO	-	Lowest unoccupied molecular orbital
O_i	-	interface oxygen atoms of the thin alumina film on NiAl(110)
O_s	-	surface oxygen atoms of the thin alumina film on NiAl(110)
ML	-	Monolayer
PDOS	-	Partial density of states
RT	-	Room temperature
SAM	-	Self-assembled monolayer

SS	-	Surface state
STM	-	Scanning tunneling microscopy
STS	-	Scanning tunneling spectroscopy
UHV	-	Ultra-high vacuum
UPS	-	Ultraviolet photoelectron spectroscopy
V_{mod}	-	Modulation voltage of the lock-in amplifier (given as rms value), which is used for conductance imaging and STS
V_s	-	Sample bias
VB	-	Valence band

Appendix B

Publications and Conference Contributions

Publications ¹

1. A. Terasaki, T. M. Briere, M. Kulawik, S. Minemoto, K. Tono, A. Matsushita, and T. Kondow. Ferromagnetic spin coupling in the manganese trimer ion evidenced by photodissociation spectroscopy. *J. Chem. Phys.*, 118:2180, 2003.
2. M. Kulawik, M. Nowicki, G. Thielsch, L. Cramer, H.-P. Rust, H.-J. Freund, T. P. Pearl, and P. S. Weiss. A double lamellae dropoff etching procedure for tungsten tips attached to tuning fork atomic force microscopy/scanning tunneling microscopy sensors. *Rev. Sci. Instrum.*, 74:1027, 2003.
3. M. Kulawik, N. Nilius, H.-P. Rust, and H.-J. Freund. Atomic structure of antiphase domain boundaries of a thin Al₂O₃ film on NiAl(110). *Phys. Rev. Lett.*, 91:256101, 2003.
4. N. Nilius, M. Kulawik, H.-P. Rust, and H.-J. Freund. Defect-induced gap states in Al₂O₃ thin films on NiAl(110). *Phys. Rev. B*, 69:121401, 2004.
5. M. Heyde, M. Kulawik, H.-P. Rust, and H.-J. Freund. Double quartz tuning fork sensor for low temperature atomic force and scanning tunneling microscopy. *Rev. Sci. Instrum.*, 75:2446, 2004.
6. N. Nilius, M. Kulawik, H.-P. Rust, and H.-J. Freund, Quantization of electronic states in individual oxide-supported silver particles. *Surf. Sci.*, 572:347, 2004.

¹Publications which belong to this thesis are marked on the margin

7. M. Kulawik, H.-P. Rust, M. Heyde, N. Nilius, B. A. Mantooth, P. S. Weiss, and H.-J. Freund. Interaction of CO molecules with surface state electrons on Ag(111). *Surf. Sci.*, 590:L253, 2005.
8. M. Kulawik, H.-P. Rust, N. Nilius, M. Heyde, and H.-J. Freund. STM studies of ordered $(\sqrt{31} \times \sqrt{31})R9^\circ$ CO islands on Ag(111). *Phys. Rev. B*, 71:153405, 2005.
9. M. Kulawik, N. Nilius, and H.-J. Freund. Influence of the metal substrate on the adsorption properties of thin oxide layers: Au atoms on a thin alumina film on NiAl(110). *Phys. Rev. Lett.*, *Accepted*.
10. M. Heyde, M. Kulawik, H.-P. Rust, and H.-J. Freund. Frequency modulated atomic force spectroscopy on NiAl(110) partially covered with a thin alumina film. *Phys. Rev. B*, *Accepted*.
11. M. Schmid, M. Shishkin, G. Kresse, E. Napetschnig, P. Varga, M. Kulawik, N. Nilius, H.-P. Rust, and H.-J. Freund. Oxygen-deficient line defects in an ultrathin aluminum oxide film. *Submitted*.

Conference Contributions

1. Structure investigation of domain boundaries of Al₂O₃ on NiAl(110) by Low-Temperature Scanning Tunneling Microscopy. (Talk)
M. Kulawik, N. Nilius, H.-P. Rust, and H.-J. Freund.
22nd European Conference on Surface Science, Praha, Czech Republic, September 7–12, 2003.
2. Adsorption of CO on Ag(111) mediated by the interaction with surface-state electrons. (Talk)
M. Kulawik, M. Heyde, B. Mantooth, H.-P. Rust, P. S. Weiss, and H.-J. Freund.
103. Hauptversammlung der Deutschen Bunsen-Gesellschaft für Physikalische Chemie e. V., Dresden, Germany, May 20–22, 2004, .
3. STM studies on the electronic properties of single Au atoms and Au dimers on a thin Al₂O₃ film on NiAl(110). (Talk)
M. Kulawik, N. Nilius, H.-P. Rust, and H.-J. Freund.
69. Jahrestagung der Deutschen Physikalischen Gesellschaft, Berlin, Germany, March 4–9, 2005.

Danksagung

Das Gelingen dieser Arbeit ist maßgeblich der Unterstützung durch Mitarbeiter, Freunde und Verwandte geschuldet, bei denen ich mich an dieser Stelle recht herzlich bedanken möchte. Mein besonderer Dank gilt:

- Herrn Prof. Hans-Joachim Freund für die interessante Aufgabenstellung, die hervorragenden Arbeitsbedingungen, sowie viele entscheidende und richtungsgebende Hinweise,
- Herrn Dr. Hans-Peter Rust für die gute Betreuung, interessante Anregungen sowie wichtige Hilfestellungen bei experimentellen und wissenschaftlichen Problemen,
- Herrn Dr. Niklas Nilius für unzählige, wertvolle Diskussionen der wissenschaftlichen Ergebnisse, die unermüdliche Hilfe bei experimentellen Fragestellungen und nicht zuletzt für seine moralische Unterstützung,
- Herrn Prof. Georg Kresse für die Bereitstellung der Koordinaten des Aluminiumoxidfilms und Rechnungen an Antiphasendomängengrenzen sowie für hilfreiche Diskussionen,
- Herrn Dr. Emile Rienks, der bei zahlreichen Umbauten und Reparaturen des Mikroskops immer tatkräftig zur Seite stand und dabei nicht nur seine gute Laune behielt, sondern damit sogar seine Mitstreiter ansteckte,
- Herrn Gero Thielsch für seine zuverlässige Hilfe in allen technischen Belangen,
- Dem „Umzugsteam“ Herrn Dr. Hans-Peter Rust, Herrn Dr. Marek Nowicki und Herrn Gero Thielsch, die entscheidenden Anteil an der schnellen Wiederaufnahme der wissenschaftlichen Arbeit nach dem Umzug der beiden Mikroskope hatten,
- Mitgliedern der feinmechanischen Werkstatt und hier besonders Herrn Klaus-Peter Vogelgesang, der benötigte Bauteile stets rasch und in hervorragender Qualität lieferte,

-
- Allen Mitgliedern des Instituts für Chemische Physik für die gute Atmosphäre,
 - Meiner Mutter, Frau Marianne Kulawik, die mich von Kind auf gefördert und unterstützt hat, und damit den jetzt eingeschlagenen Weg erst ermöglichte, sowie
 - Der Studienstiftung des deutschen Volkes für die finanzielle und ideale Unterstützung während des Studiums und der Promotion.

Lebenslauf

Name:	Maria Kulawik		
Geburtsdatum:	23.10.1976		
Geburtsort:	Berlin		
1983	–	1991	Grundschule in Berlin
1991	–	1996	Heinrich-Hertz-Oberschule in Berlin, Gymnasium mit mathematisch-naturwissenschaftlichem Profil
07/1996	–	08/1996	Forschungsaufenthalt am Weizmann Institute of Science in Rehovot, Israel
10/1996	–	07/1998	Studium der Chemie an der Humboldt-Universität zu Berlin
09/1998	–	07/1999	Studium der Chemie/Physik an der Ecole Nationale Supérieure de Chimie et de Physique de Bordeaux in Frankreich, Stipendium des DAAD
10/1999	–	07/2001	Fortsetzung des Chemie-Studiums an der Humboldt-Universität zu Berlin, Stipendium der Studienstiftung des deutschen Volkes 1997–2001
10/2000	–	07/2001	Diplomarbeit unter Betreuung von Prof. Dr. K. Rademann und Dr. W. Christen, Titel „New Design of a Compact, High Resolution Time-of-Flight Mass Spectrometer“
07/2001	–	10/2001	Forschungsaufenthalt am Toyota Technological Institute and Genesis Research Institute in Chiba, Japan

-
- 10/2001 – 03/2002 Studium der Japanologie/Polonistik an der Humboldt-Universität zu Berlin
- seit 04/2002 Promotion am Fritz-Haber-Institut der Max-Planck-Gesellschaft in Berlin, Thema: „Low-Temperature Scanning Tunneling Microscopy Studies on Model Catalysts“, Betreuung durch Prof. Dr. H.-J. Freund und Dr. H.-P. Rust, Promotionsstipendium der Studienstiftung des deutschen Volkes

Selbständigkeitserklärung

Hiermit erkläre ich, die vorliegende Arbeit selbständig ohne fremde Hilfe verfaßt und nur die angegebene Literatur und Hilfsmittel verwendet zu haben.

Maria Kulawik
Berlin, den 20. Januar 2006